Ultra-High Resolution Laser Spectroscopy of Rare Earth Doped Solids

by

Matthew John Sellars

A thesis submitted for the degree of Doctor of Philosophy

of the Australian National University

November 1995

Statement of authorship

The contents of this thesis, except where indicated by references, are entirely my own work.

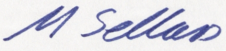

Matthew John Sellars
November 1995

Acknowledgments

First of all my thanks goes to my supervisor Dr Neil Manson, for communicating his great enthusiasm for physics and life, along with his wealth of knowledge and experience in solid state physics. I also thank Dr Peter Fisk for initiating the ultra high resolution laser work within the Solid State group at RSPhysSE.

I am grateful to Dennis Gibson and the other members of the RSPhysSE's electronics unit for designing and constructing the servo-controller used to stabilise the laser. The technical expertise of Ian Mcrae and Paul Morrison was invaluable throughout my time at RSPhysSE, and I am also indebted to Dennis Gibson for answering my countless inquiries about electronics.

Stimulating discussions with Dr John Martin and Dr Changjiang Wei were most helpful. Dr John Martin provided many helpful comments in reviewing initial drafts of this work, as did Dr Deborah Hope. I must also thank my family; their tolerance, warmth and patience were always offset by a refreshing scepticism.

For the encouragement and support she has given me over many years I owe an immense debt of thanks to Deborah Hope.

Abstract

A commercial single longitudinal mode ring dye laser was modified to improve its frequency stability. The frequency was stabilised to a linewidth of approximately 1 kHz over time intervals of tens of milliseconds. The resolution of the laser was demonstrated by burning and then probing a spectral hole with a 3.7 kHz width (FWHM) in the $^1F_0 \Rightarrow {}^1D_0$ transition in $Y_2O_3:Eu^{3+}$. This to the author's knowledge is the narrowest spectral hole directly observed in a solid.

The stabilised laser was used to investigate the coherent response of the $^1F_0 \Rightarrow {}^1D_0$ transition in $KEu(WO_4)_2$. The dephasing rate of the transition was studied as a function of both the magnitude and the phase of the optical driving field. Critical to this investigation was the development of a new optical coherent transient technique, coherence phase locking. The new technique is the optical analogue to the NMR technique of spin locking. It was concluded that the relative phase of the driving field to the transition dipole moment is an important parameter in interpreting the observed non-optical Bloch equation behaviour.

Time resolved holeburning in the $^3H_4 \Rightarrow {}^1D_2$ transition in $LaF_3:Pr^{3+}$ is used to investigate magnetic interactions involving the Pr^{3+} ions. The cross-relaxation of Pr^{3+} groundstate hyperfine levels between Pr^{3+} ions was found to be a mechanism for broadening the spectral holes. A new optical transition was identified, in which the spin of a neighbouring ^{19}F nuclei is flipped with the optical excitation of the Pr^{3+} ion to the $^1D_2$ state.

Table of contents

Chapter 1 Introduction

1.1 Overview and motivation

The optical spectra of rare earth ion centres in crystals closely resemble those of the free rare earth ion. The spectra of these centres have been studied for many years. For the free ion the levels associated with the optical transitions are metastable, resulting in very narrow homogeneous line widths. It has been found that for particular transitions under certain circumstances very narrow homogeneous line widths can also be observed in rare-earth ion centres.

The resemblance between the ion centre spectra and the spectra of the free ion results from the levels associated with the optical transitions having the same electronic configuration, and the open shell of 4f electrons being well-screened from the lattice by filled outer shells. The effect of both the static and dynamic crystal fields on the ion's energy levels is small and can be treated as a perturbation.

The long lifetimes of the free ion states are a consequence of the optical transitions occurring between states with the same electronic configuration, in that pure electric dipole transitions are forbidden by parity. When the rare earth ion is a dopant in a crystal the transitions will still be very weak, although in the case of an odd parity crystal field, electric dipole transitions are no longer strictly forbidden. This is a result of mixing of electron configurations of opposite parity into the 4f configuration. At room temperature the lifetimes of the excited states are shortened by phonon-assisted electric dipole transitions. The rate of these phonon-assisted transitions can be significantly reduced by cooling the crystal down to liquid helium temperatures. At these low temperatures the lifetime of the lowest level of a multiplet is typically limited by the rates of the zero-phonon transitions and can be of the order of milliseconds.

In general the homogeneous linewidths observed for the transitions from the ground state to these long lived states are orders of magnitude greater than the natural linewidth. This is due to the interaction of the rare earth ion with the dynamic environment of its crystal host, resulting in an increased dephasing rate of the transition. The dominant interactions are usually magnetic in origin, where the magnetic moments associated with the states of the rare earth ion interact with the fluctuating magnetic fields in the crystal. The fluctuating field is due to strongly interacting magnetic moments constantly exchanging spin. Both the moment associated with the rare-earth ion and the moments in the host can be either electronic or nuclear in origin.

For a given crystal host the narrowest homogeneous linewidths will be between states of the rare-earth ion with no first order electronic spin. Two transitions that meet these criteria are the $^7F_0 \Rightarrow {}^5D_0$ transition in Eu^{3+} and the transition between the lowest crystal field levels of the $^3H_4$ and $^1D_2$ states of the Pr^{3+} ion occupying a non-axial site in the crystal. The states involved in these transitions still possess enhanced nuclear magnetic moments of the order of a kilohertz per gauss, that will interact with the crystals magnetic moments. To reduce the linewidth further a host must be chosen that possesses no net electronic spin and minimal nuclear magnetic moments. The narrowest observed homogeneous line width for a rare-earth doped crystal is 120 Hz in a sample of $Y_2SiO_5:Eu^{3+}$ [Equall *et al.* 94].

A practical application of these rare-earth transitions with narrow homogeneous line widths, that has received substantial attention, is frequency-selective optical memory [Szabo 1975]. Frequency selective optical memory schemes use the persistent bleaching of the absorption of packets of ions though optical pumping cycles and the large contrast of the homogeneous to the inhomogeneous linewidths of these transitions. The inhomogeneous broadening is due largely to inhomogenieties in the crystal strain field. Typically the inhomogeneous linewidths are of the order of gigahertz. The density in frequency space of the data storage capacity is given by the ratio of the inhomogeneous linewidth to the homogeneous linewidth. For a material with a homogeneous linewidth of 100 Hz and an inhomogeneous linewidth of 10 GHz a memory storage capacity of 10^8 for each optical spot is anticipated. Time domain optical data storage has also been demonstrated in these materials using stimulated photon-echo-memory [Mossberg *et al.* 1982, Yano *et al.* 92].

For the development of such optical data storage schemes it is important to understand how dynamic processes in the crystal effect the optical transition. The time scale over which these dynamical processes can operate varies from microseconds to years. Processes that operate on fast time scales tend to produce an increase in the homogeneous linewidth of the transition and, as discussed above, decrease the data storage capacity. Slower processes can degrade the data by either causing a relaxation in the hyperfine population or causing random shifts in the optical transition frequencies of the ions, a process known as spectral diffusion.

To study the homogeneous profile in the presence of the inhomogeneous broadening a suite of specialised high-resolution laser techniques has been used. The time domain technique of photon echoes has been the preferred method for studying homogeneous

linewidths less than 1 MHz wide. Photon echoes, and the closely related stimulated photon echoes, have the advantage that they can resolve homogeneous linewidths narrower than the linewidth of the laser. In these techniques the Fourier width of the pulses used can be selected to be greater than the linewidth of the laser and the homogeneous profile. This overcomes the need to frequency stabilise the laser such that its linewidth is less than the homogeneous linewidth. To date all observations of linewidths below a few kHz have been made using photon echoes. The resolution of the other techniques depends on the linewidth of the laser. Hence to use these techniques in studying the narrowest of the rare earth ion transitions, a laser with a resolution of at least 1 kHz is required.

1.2 Outline of present work

In this work a commercially available ring dye laser has been modified to reduce its linewidth from 1 MHz to below 1 kHz. The laser was then used to investigate a number of transitions using coherent transient and saturation techniques. The modifications to the laser are described in Chapter 2.

In Chapter 3 the modified laser is used to demonstrate persistent spectral hole burning in the $^7F_0 \Rightarrow {}^5D_0$ transition in Y_2O_3:Eu^{3+}. These holeburning measurements are used to characterise the laser's stability. Y_2O_3, like Y_2SiO_5, is a crystal with no electronic spin and only small nuclear magnetic moments and the $^7F_0 \Rightarrow {}^5D_0$ transition possesses a very narrow homogenous linewidth, 625 Hz [MacFarlane *et al.* 1981]. In persistent spectral holeburning the laser is used to excite a homogeneous packet of ions out of the inhomogeneous profile. Through an optical pumping cycle the ions are deposited into ground state hyperfine levels out of resonance with the laser (see Fig 1.1). Scanning the laser through this region reveals a hole in the absorption profile of the inhomogeneously broadened line at the original frequency of the laser. These holeburning measurements are used to characterise the laser stability.

A new optical coherent transient technique utilising the modified laser, is demonstrated in Chapter 4. The technique, analogous to the NMR pulse technique of spin locking, uses a pulse sequence where both the amplitude and the phase of the driving field are switched. The technique was used along with other coherent transient techniques to investigate the effect of the driving field on the coherence dephasing of the $^7F_0 \Rightarrow {}^5D_0$ transition in $KEu(WO_4)_2$.

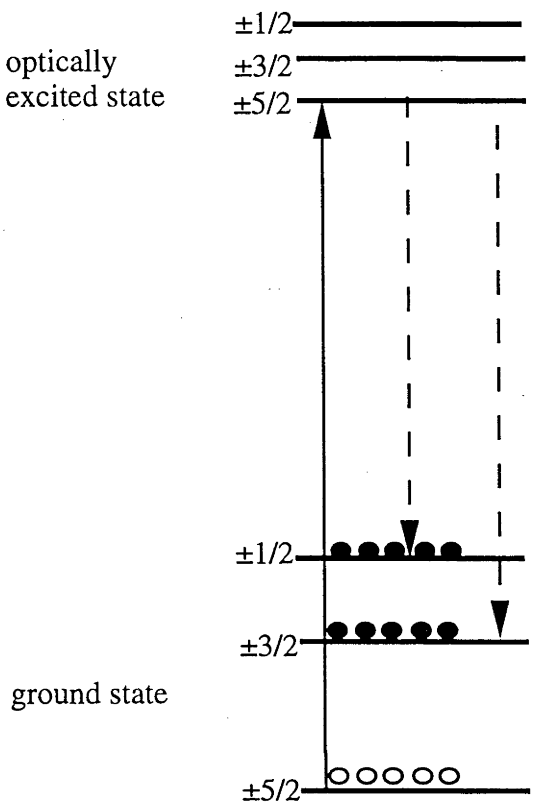

Figure 1.1 An example of an optical pumping cycle where resonant ions are deposited into hyperfine levels which are out of resonance with the laser. For the optical transitions investigated in this work the electronic states are singlets and hyperfine structure is due to a quadrupole interaction.

In Chapter 5 a detailed study is made of the time evolution of spectral holes burnt into the $^3H_4 \Rightarrow {}^1D_2$ transition in $LaF_3:Pr^{3+}$. Unlike $Y_2O_3:Eu^{3+}$ and $Y_2SiO_5:Eu^{3+}$, $LaF_3:Pr^{3+}$ possesses nuclei with large nuclear magnetic moments. The sample provides a useful case study of the effects of magnetic interactions on rare-earth optical transitions. In this work time-resolved spectral holeburning is used to study magnetic processes acting on time scales from milliseconds to seconds. Presented in Chapter 6 is an overall conclusion and directions for future investigations using the stabilised laser are also discussed.

Chapter 2 Laser stabilisation

2.1 Introduction

As discussed in Chapter 1, time domain measurements have established that there are rare-earth systems with transition linewidths less than a few kilohertz. In order to resolve such narrow transitions in the frequency domain it is necessary to have a tunable laser source with a comparable linewidth. To be generally applicable to investigations of a range of rare earth systems the laser is required to be broadly tunable in the visible spectrum; in today's technology this necessitates the use of a dye laser.

The linewidth of free-running single mode dye lasers is in general in excess of 10 MHz [Salomon *et al.* 1988]. Most of this linewidth can be attributed to fast fluctuations in the optical thickness of the dye jet stream. Narrower linewidths can be achieved by actively stabilising the laser frequency to a stable reference such as the mode of an optical cavity. Actively frequency stabilised single mode dye lasers became commercially available in late nineteen seventies in the form of the Coherent 699-21 and 599-21 family of lasers, and the Spectra Physics 380D laser. The linewidths of all of these lasers were in excess of 500 kHz. The Spectra Physics laser has since gone off the market and the Coherent 699 laser has been re-engineered into the 899 series, but with no reduction in its linewidth.

The shortfall in Coherent's active frequency stabilisation system lies in their use of a low finesse confocal cavity as the reference, and in the limited bandwidth of their frequency correction servo-controller. The modifications made to a Coherent 699-29 single mode ring dye laser to reduce its linewidth below 1 MHz will be described in this chapter.

The modifications involve locking the laser's frequency to a mode of a high finesse non-confocal optical cavity and increasing the bandwidth of the servo-controller. The method used follows closely that of Drever *et al.* [1983]. The performance of this laser will then be assessed in terms of the requirements of the proposed spectroscopic measurements in rare-earth doped solids, discussed in Chapter 1.

2.2 Theory of frequency stabilisation:

2.2.1 Error signal:

The locking technique first employed by Drever has been successfully applied by a number of groups to reduce the linewidth of their dye lasers into the sub-Hertz to 100 Hz range [Hall *et al.* 1983, DeVoe *et al.* 1984, Helmcke *et al.* 1987, Houssin *et al.* 1988, Steiner *et al.* 1989, Kallenbach *et al.* 1991, Mitsunaga *et al.* 1993 , Zhu *et al.* 1993]. The two key elements in this method are the use of a phase-modulation technique to generate an error signal from the light reflected off a high finesse reference cavity and the use of a electro-optic phase modulator in the laser cavity for fast frequency corrections. Using this method servo bandwidths in excess of 1 MHz have been demonstrated along with a high detection sensitivity to frequency excursions.

Figure 2.1 is a schematic diagram of the locking system used here to generate an error signal from a high finesse reference cavity, which was adapted from Drever's system. An electro-optic phase modulator produces FM sidebands on the laser output at the rf frequency υ_m. The modulated beam is then coupled into the reference cavity. The modulation frequency is chosen such that when the carrier is on resonance the sidebands lie well outside the passband of the reference cavity. It is also set to be a few octaves greater than the desired bandwidth of the servo. When the laser frequency is close to a resonance of the reference cavity the light reflected off the cavity will possess an AM modulation at the frequency υ_m. This AM modulation is produced when the cavity breaks the symmetry of the original FM modulation by preferentially absorbing one of the sidebands or by introducing a phase shift in either the carrier or one of the sidebands. The reflected light is steered onto a photodiode. The electronic signal generated by the photodiode is amplified and passed through a high pass filter, to cut out frequency noise on the signal. The resultant signal is heterodyned with a local oscillator at the original modulation drive frequency, to produce the error signal.

The error signal is given by Equation 2.1, the derivation of which is shown in appendix A.

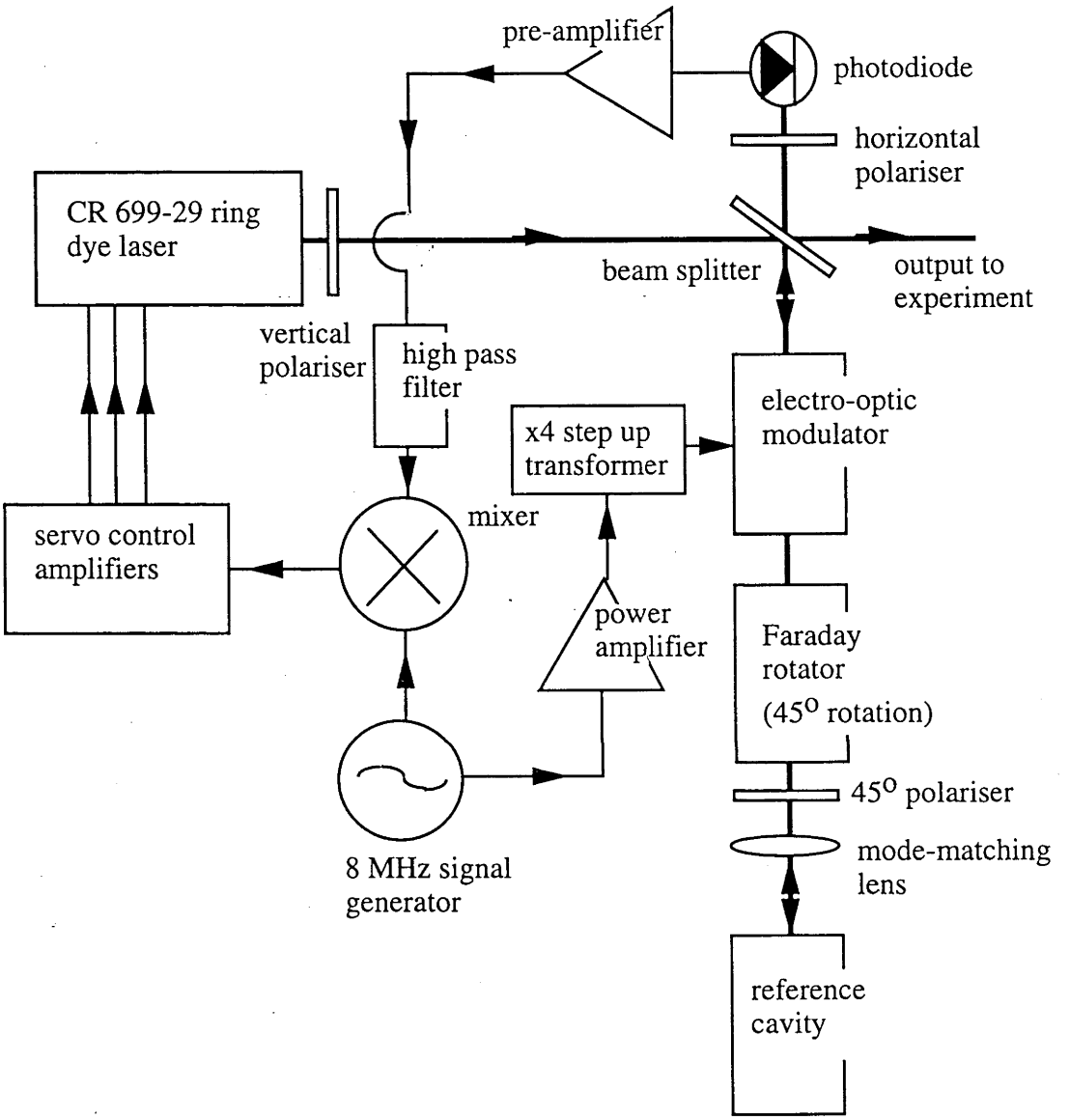

Figure 2.1 Schematic diagram of the laser stabilisation system.

$$V = g\frac{2\eta q E_o^2}{h\nu_c} J_0(\delta)J_1(\delta) \times$$

$$\mathrm{Re}\left(\left\{\frac{\rho t^2 \sin\theta_c}{D_c}\left[\left[\rho+\rho t^2\frac{\rho^2-\cos(\theta_c+\theta_m)]}{D_+}\right]+\left[\rho+\rho t^2\frac{\rho^2+\cos(\theta_c-\theta_m)]}{D_-}\right]\right]\right.$$

$$-\left[\rho+\rho t^2\frac{\rho^2+\cos\theta_c]}{D}\right]\left[\rho t^2\frac{\sin(\theta_c+\theta_m)]}{D_+}+\rho t^2\frac{\sin(\theta_c-\theta_m)]}{D_-}\right]\Big\}i\exp[-i\varphi_{LO}]+$$

$$\left[\rho+\rho t^2\frac{\rho^2+\cos\theta_c]}{D}\right]\left[\left[\rho+\rho t^2\frac{\rho^2-\cos(\theta_c+\theta_m)]}{D_+}\right]-\left[\rho+\rho t^2\frac{\rho^2+\cos(\theta_c-\theta_m)]}{D_-}\right]\right]+$$

$$\left.\frac{\rho t^2\sin\theta_c}{D_c}\left[\left[\rho t^2\frac{\sin(\theta_c+\theta_m)]}{D_+}-\rho t^2\frac{\sin(\theta_c-\theta_m)]}{D_-}\right]\right]\Big\}\exp[-i\varphi_{LO}]\right) \tag{2.1}$$

where

ρ^2 is the reflection coefficient of the cavity mirrors,

$t^2 = (1-\rho^2)$ is the transmission coefficient of each mirror,

d is the cavity length,

η is the quantum efficiency of the detection,

q is the charge on an electron,

υ_c is the laser frequency,

υ_m is the modulation frequency,

$\theta_m = \frac{4\pi\nu_m d}{c}$ is the accumulated phase shift in the laser field after one round trip in the cavity,

$\theta_m = \frac{4\pi\nu_m d}{c}$ is the accumulated phase shift in the modulation on the laser after one round trip in the cavity,

E_o^2 is the laser power mode match to the cavity resonance and

$D_c = 1+\rho^4-2\rho^2\cos\theta_c$,

$D_+ = 1+\rho^4-2\rho^2\cos(\theta_c+\theta_m)$,

$D_- = 1+\rho^4-2\rho^2\cos(\theta_c-\theta_m)$,

g is the electronic gain.

Figures 2.2a and b show the error signal as a function of the frequency offset of the carrier from the cavity resonance, with the local oscillator respectively in-phase and in-quadrature with the signal from the photodiode. It is the in-quadrature component which has the desired characteristics for use as an error signal. On the high-energy side the signal is positive for frequencies within υ_m of the carrier and on the low-energy side it is negative. A servo-loop with negative feedback will push the laser frequency into

resonance with the cavity. In the region bounded by ±HWHM of the cavity resonance the error is extremely steep, resulting in a frequency discriminator with a very high sensitivity. Using this error signal it is possible to have a tight locking region close to the lock point and at the same time a robust system capable of recovering from frequency excursions of magnitude up to υ_m. It is also worth noting that the in-phase component is zero at line centre, and therefore changes to the phase of the local oscillator will not shift the locking point away from the resonance peak.

When the resonance linewidth of the cavity is assumed to be much smaller than υ_m and υ_m is in turn much smaller than the spacing between the resonant frequencies of the cavity, at any one time only one component of the modulated light can interact strongly with a cavity resonance. Under this approximation there are only three significant contributions to the in-quadrature component of the error signal, which can now be written as

$$V = g\frac{2\eta q E_o^2}{h\nu_c} J_0(\delta)J_1(\delta)\rho^2 t^2\left[\frac{\sin\theta_c}{D_c} - \frac{\sin(\theta_c+\theta_m)}{D_+} - \frac{\sin(\theta_c-\theta_m)}{D_-}\right] \qquad (2.2)$$

For frequencies close to resonance such that modulus of θ_C is much less than 1, the error signal is approximately described by the first term in Equation (2.2)

$$\frac{\partial V}{\partial \nu} = g\frac{2\eta q E_o^2}{h\nu_c} J_0(\delta)J_1(\delta)\frac{1}{\Delta\nu_{1/2}} \qquad (2.3)$$

As shown in Appendix A the slope of the frequency discriminator at the cavity resonance is given by

$$\frac{\partial V}{\partial \nu} = g\frac{2\eta q E_o^2}{h\nu_c} J_0(\delta)J_1(\delta)\frac{1}{\Delta\nu_{1/2}} \qquad (2.4)$$

where $\Delta\nu_{1/2}$ is the FWHM linewidth of the cavity resonance.

It was shown by Houssin *et al.* [1988] (and also reproduced in Appendix A) that the slope of the frequency discriminator is related to V_{p_p}, the peak to peak voltage of the error signal, and $\Delta\upsilon_{1/2}$ via the expression:

$$\delta V = 2\left(\frac{V_{p-p}}{\Delta\nu_{1/2}}\right)\delta\nu \qquad (2.5)$$

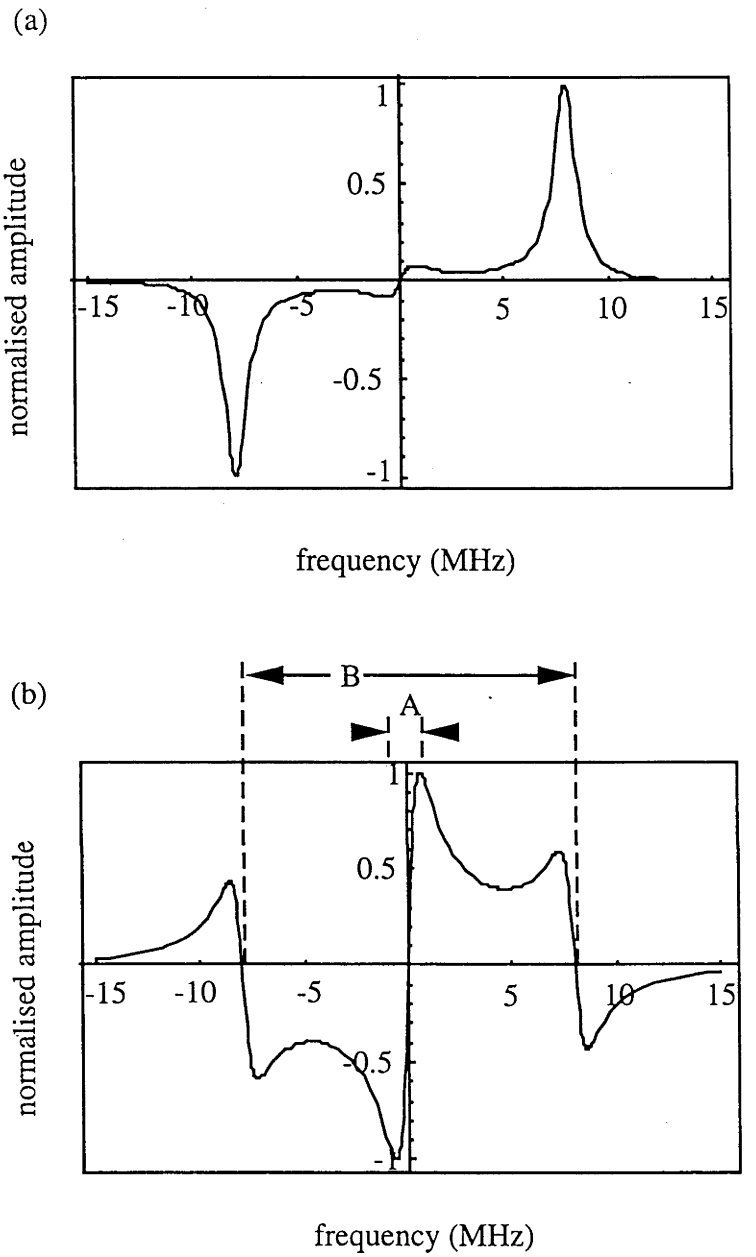

Figure 2.2 a and b. The DC response of the error signal with a modulation frequency of 8 MHz and a cavity resonance width of 500 kHz (HWHM). a) Signal in phase with modulation. (b) Signal in quadrature with modulation. The region over which the error signal has the correct phase is indicated by "B". The tight locking region is indicated by "A".

This last expression allows the sensitivity of the frequency discriminator to be calculated from parameters that can be easily measured; the height of the error signal and the width of the cavity resonance.

2.2.2 AC response of error signal

Equation 2.1 describes only the DC response of the error signal. In designing the servo controller to correct the laser frequency it is important to know the response of the error signal to AC perturbations. A lag in the response of the error signal due to the buildup time of the reference cavity can be expected. When the laser is locked to the cavity resonance, the sidebands which are well off-resonance can be considered to be simply reflected off the input mirror of the cavity. For the carrier frequency, which is close to resonance, the situation is different. The carrier reflected off the cavity can be decomposed into two parts. The first is simply the light reflected directly off the input mirror. It contributes nothing to the AM modulation, and hence the error signal, as it bears the same phase relationship with the sidebands as it had before the reflection. The second component is the light which has coupled into the cavity and is now leaking out through the input coupler. If the perturbation is significantly slower than the buildup time of the cavity then the frequency of this component, leaking out of the cavity, is the same as the reflected component off the cavity. The two components will differ by a shift in their relative phase. The shift is the origin of the DC response, which is a comparison of the frequency of the laser to that of the cavity resonance. For perturbations comparable to or faster than the cavity buildup time the cavity acts as an integrator. The effective phase of the leakage out of the cavity is a time-weighted average of the phase of the light coupled into the cavity. Drever *et al.* [1983] pointed out that for these fast perturbations the error signal acts as a phase comparator between the laser and the leakage out of the cavity.

Equation 2.6, derived in Appendix B, gives the response of the error signal to small perturbations about the lock point at the frequency $\omega_n/2\pi$.

$$V(\nu_n) = 2g\frac{\eta q E_0^2}{h\nu_c} J_1(\delta_m)\left[\rho + \rho t^2 \frac{\rho^2 - \cos\theta_m}{D_m}\right]\times \frac{\nu_p}{\nu_n}\left[\left[\rho + \rho t^2 \frac{\rho^2 - \cos\theta_m}{D_m}\right]\sin 2\pi\nu_n t + \left[\frac{\sin\theta_n}{D_n}\rho t^2\right]\cos 2\pi\nu_n t\right], \quad (2.6)$$

where υ_p is the amplitude of the frequency perturbation and υ_n is the frequency of the perturbation.

The amplitude and phase shift of the error signal as a function of the perturbation frequency is plotted in Figures 2.3a and b. From this plot it is apparent that the error signal has a frequency response of a single-pole low-pass filter, with the characteristic 6 dB/octave rolloff and 90 degrees phase shift, at high frequencies. The 3 dB rolloff frequency is the HWHM of the cavity resonance. Because the error signal only undergoes a 90^{o} phase shift in going to higher frequencies it is possible to run the servo loop controlling the laser frequency with a bandwidth greater than the linewidth of the reference cavity resonance.

2.2.3 Basic servo-controller theory

The final stability of the actively stabilised laser will depend on frequency fluctuations of the unstabilised laser, the sensitivity of the frequency discriminator, the gain of the servo and the noise in the all the components of the servo controller. Figure 2.4 is a simplified block diagram of the stabilised laser showing the various gain/sensitivity coefficients (G_i's) and noise sources. Analysis of the loop equations gives the following expression for the spectral density of the rms. frequency deviations of the stabilised laser:

$$\Delta\nu(\nu_n)_{output} = \frac{\Delta\nu(\nu_n)_{open}}{1+G_{disc}(\nu_n)G_{dc}(\nu_n)G_{el}(\nu_n)} + \frac{N_{disc}(\nu_n)G_{dc}(\nu_n)G_{el}(\nu_n)}{1+G_{disc}(\nu_n)G_{dc}(\nu_n)G_{el}(\nu_n)} + \frac{N_{dc}(\nu_n)G_{el}(\nu_n)}{1+G_{disc}(\nu_n)G_{dc}(\nu_n)G_{el}(\nu_n)} \qquad (2.7)$$

where $\Delta\nu(\nu_n)_{output}$ is the rms spectral density of the laser output frequency deviation, $\Delta\nu(\nu_n)_{open}$ is the rms spectral density of the frequency deviation of the unstabilised laser, $G_{el}(\upsilon_n)$ is the sensitivity to the voltage applied to the tuning elements, $G_{disc}(\upsilon_n)$ is the discriminator sensitivity, defined as the derivative of the voltage output of the mixer with respect to the laser frequency, $G_{dc}(\upsilon_n)$ is the gain of the DC amplification stage, N_{disc} is the discriminator's intrinsic noise voltage at the mixer output and $N_{dc}(\upsilon_n)$ is the DC amplifier noise voltage referred to its output. Each of the terms in Equation 2.6 is the closed loop contribution to the frequency noise from each of the blocks shown in figure 2.4. The product $G_{disc}G_{dc}G_{el}$, in general a complex number, is the open loop gain $G_o(\upsilon_n)$. From Equation 2.6 it can be seen that the servo loop will oscillate if $G_o(\upsilon_n) = -1$. For this to occur $G_o(\upsilon_n)$ must have undergone a 180^{o} phase shift. The condition for the stable operation of the servo, taking account of the saturation of the amplifiers, is best presented in the form of a Nyquist diagram. In a Nyquist diagram the real and imaginary components of $G_o(\upsilon_n)$ are plotted on a x-y graph. An oscillation in the servo loop will occur if the plot encloses the point (-1,0). Figures 2.5 a, b and c show the Nyquist

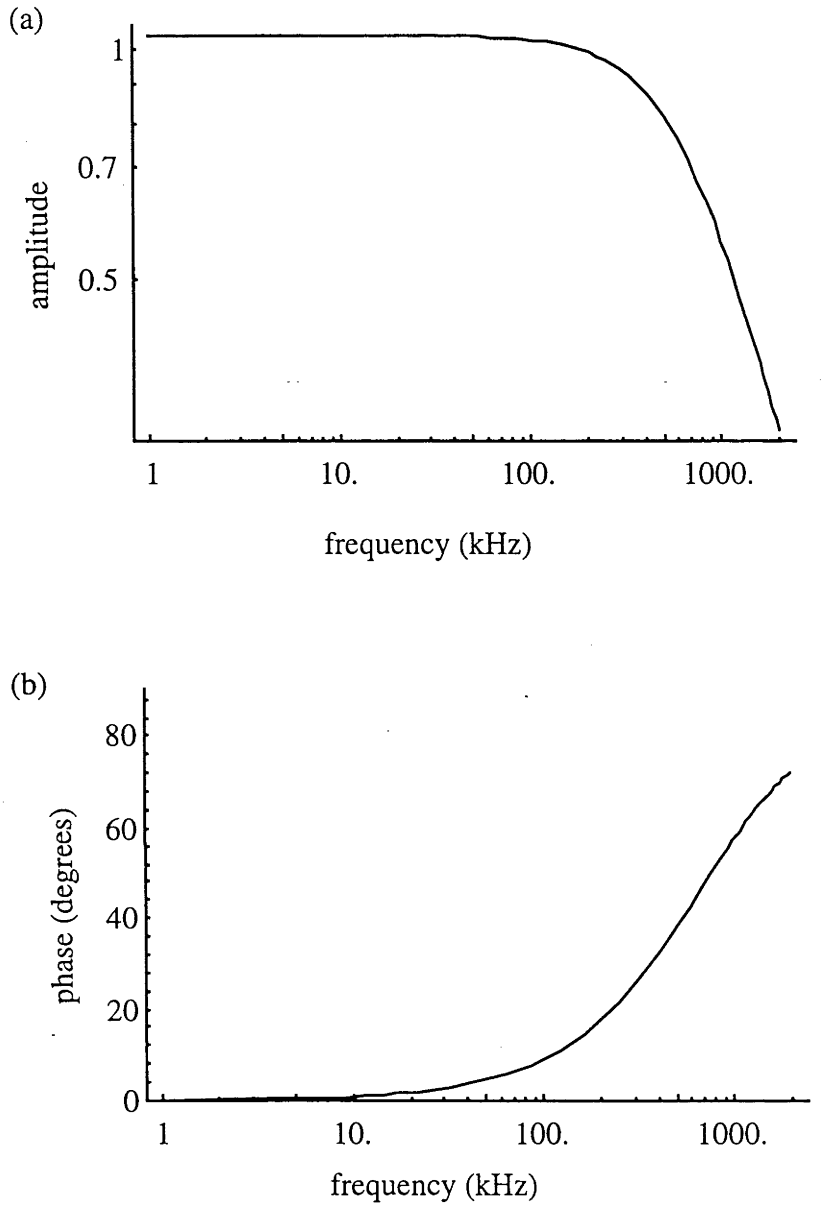

Figure 2.3 a & b. Amplitude and phase shift of the error signal as a function of the perturbation frequency, calculated using Equation 2.6. The HWHM of the cavity resonance was set to 500 kHz.

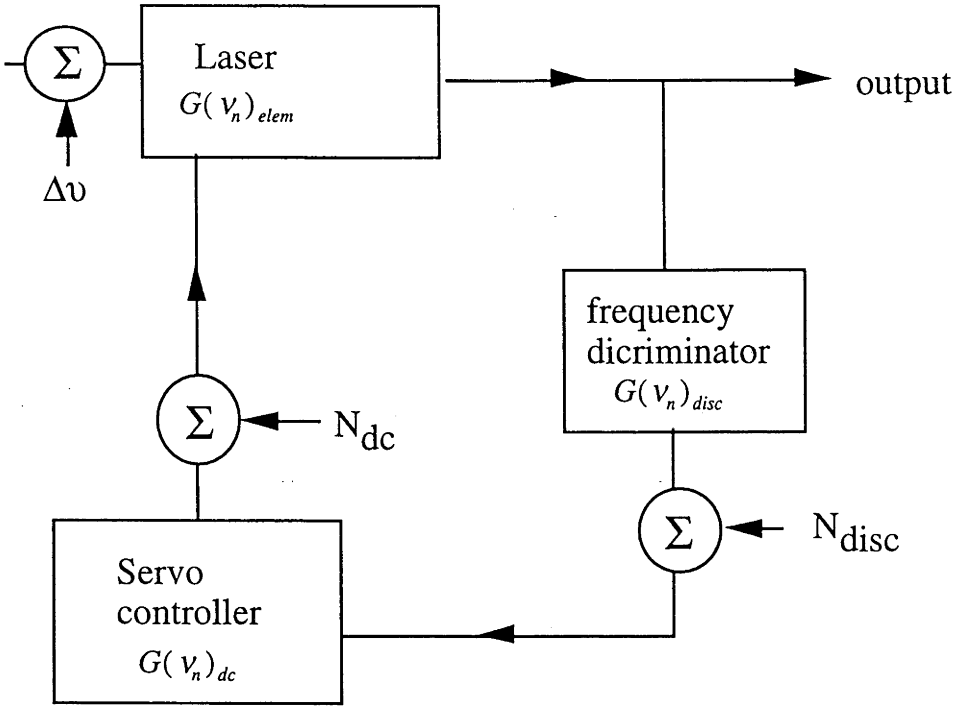

Figure 2.4: Block diagram of the laser stabilisation servo loop, showing the reference points for the noise sources and the sensitivity/gain coefficients (G). $\Delta\upsilon$ is the free running frequency niose on the laser. N_{disc} is the niose associated with the frequency discriminator and N_{dc} is the noise associated with the servo control amplifiers.

diagrams for servo loops where the gain is rolled off with first, second and third order filters respectively. The first order system produces a 6 dB/octave slope at high frequencies and a maximum phase shift of 90^{o} and it can be seen from Fig 2.5 that it will be stable for all gains. The second order system produces 12 dB/octave with a maximum phase shift of 180^{o} and will be stable for all finite gains, but any additional phase shift may cause an oscillation whilst running with high gains. The third order system has an 18 dB/octave rolloff with a maximum phase shift of 270^{o} and will become unstable for gains greater than about 8.

In theory a simple first order system allows an infinite gain to be used. In practice the real components in the servo loop introduce extra phase shifts which limit the gain that can be used. To maximise the gain in the desired frequency range within the contrast of these phase shifts it is often necessary to build servo controllers with frequency responses more complex than a first order system. Important sources of these phase shifts, in the present case, include the finite bandwidth of the amplifiers, the first order rolloff, the cavity response discussed in section 2.2, and the round trip time of the servo loop. The latter introduces a phase shift of $\exp[-i2\pi d/fc]$, where d/c is the round trip time of the servo-loop, which includes both the electrical and optical paths.

2.2.4 Fundamental performance limit of stabilised lasers

In the limit of very high open loop gain the frequency stability of the laser will be limited by the noise in the servo controller. Assuming the use of low noise amplifiers so that N_{dc} is negligibly small and in the limit of very high open loop gain ($G_O \rightarrow \infty$),

$$\Delta\nu_c(\nu_n)_{output} = \frac{N(\nu_n)_{disc}}{G(\nu_n)_{disc}} \tag{2.8}$$

This expression indicates that the stability of the laser frequency will be determined by the sensitivity of the frequency discriminator. For a given level of N_{disc} the lowest frequency noise floor will be achieved with the highest possible discriminator sensitivity, G_{disc}. Equation 2.4 shows that G_{disc} can be increased by increasing the laser intensity on the photodiode, the finesse of the cavity, or the sideband intensity.
In the limit of high laser intensity on the photodiode, N_{disc} will be dominated by the shot noise in the photocurrent. The spectral density of the shot noise is given by:

$$V_{noise} = \left(\frac{2q^2 P_d \eta}{h\nu}\right)^{1/2}, \tag{2.9}$$

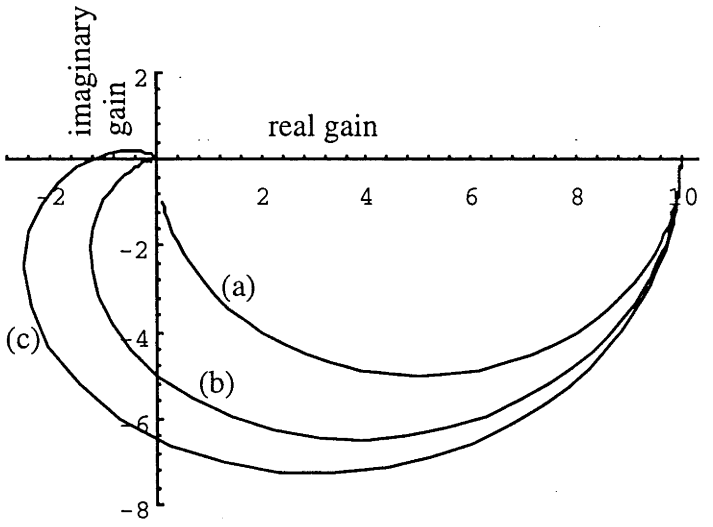

Figure 2.5. Nyquist diagrams for three different servo loops (a), (b) and (c), rolled off with a first, a second and a third order low pass filter respectively.

where q is the charge on the electron, P_d is the laser power incident on the photodiode and η is the quantum efficiency of the photodiode [Yariv 1985]. In the case of the Drever laser stabilisation scheme P_d is the light reflected off the cavity onto the photodiode when the laser frequency is locked to the peak of a cavity resonance. P_d consists of the component of the beam at the carrier frequency not mode matched to the cavity mode, as well as the total laser power in the sidebands.

The spectral density noise floor level for this situation, found by making use of Equations 2.4, 2.8 and 2.9 is:

$$\delta\nu_c(\nu_c) = \frac{\Delta\nu_{1/2}}{P_o J_1(\delta)}\left(\frac{h\nu_c P_d}{\eta}\right)^{1/2}. \qquad (2.10)$$

The typical values for the parameter in Equation 2.10 for the laser system to be described are for a wavelength of 580 nm; $\Delta\upsilon_{1/2}$ = 500 kHz, P_o =10 mW (total power incident on the cavity) , δ = 0.21, P_d = 0.8 P_o and η = 0.2. For these values the shot noise floor to the spectral density of the instantaneous laser frequency predicted by Equation 2.10 is 0.04 $Hz/\sqrt{Hz}$.

2.2.5 Characterisation of frequency stability

For spectroscopic purposes, what we really need to know is the spectral density of the laser output. In this section approximate relationships between the error signal from the laser stabilisation servo and the spectral density of the laser output will be considered.

The output signal from a single frequency laser can be modelled by the general expression:

$$V(t) = [V_0 + \varepsilon(t)]\sin[2\pi\nu_0 t + \Phi(t)] \qquad (2.11)$$

where V_0 and υ_o are the nominal amplitude and frequency, respectively. $\varepsilon(t)$ denotes the amplitude fluctuations around V_0, and $\Phi(t)$ denotes the phase fluctuations. The instantaneous frequency of the laser is given by the time rate of change of the phase divided by 2π. It will be assumed here that the amplitude noise is negligible so that the phase and frequency fluctuations can be modelled by

$$V(t) = V_0 \sin[2\pi\nu_0 t + \Phi(t)] \qquad (2.12)$$

The instantaneous frequency of the laser is given by

$$\begin{aligned} \nu(t) &= \nu_o + \frac{1}{2\pi}\frac{d\varphi(t)}{dt} \\ &= \nu_o + \Delta\nu(t) \end{aligned} \tag{2.13}$$

It is this instantaneous frequency offset that is measured by the error signal, where υ_0 is the frequency of the cavity resonance. One possible way to characterise the laser's performance is to simply take the rms of the instantaneous frequency. Unless care is taken, though, the $\Delta\upsilon_{rms}$ is not a good measure of the laser's linewidth. This problem can be understood by considering the power spectrum of $\Delta\upsilon(t)$ which is defined as the Fourier transform of the autocorrelation of $\Delta\upsilon(t)$ and is given by

$$S_{\Delta\nu}(f) = 2\int_0^\infty \langle \Delta\nu(t)\Delta\nu(t-\tau)\rangle \exp[-i2\pi f\tau]d\tau \tag{2.14}$$

where the angled brackets denote an averaging over t. The dimension of $S_{\Delta\upsilon}(f)$ is $Hz^2/Hz=Hz$. The following equation links the mean-square value of $\Delta\upsilon(t)$ to $S_{\Delta\upsilon}(t)$:

$$\langle \Delta\nu^2(t)\rangle = \int_0^\infty S_{\Delta\nu}(f)df \tag{2.15}$$

When stating a value for $\langle \Delta\nu^2(t)\rangle^{1/2}$ it is necessary to specify the bandwidth over which the measurement of $\Delta\upsilon(t)$ was made. In most practical cases where there is white frequency noise the value will continuously diverge as the measurement bandwidth is increased. $\langle \Delta\nu^2(t)\rangle^{1/2}$ will continue to diverge with increasing bandwidth even if little of the laser power is associated with the higher frequency oscillations.

As an example consider an oscillation on the laser frequency with a frequency of 10 MHz and an amplitude of 1 kHz p-p. If this is the only instability on the laser the $\Delta\upsilon_{rms}$ will be about 350 Hz. This value is independent of the frequency of the oscillation. The spectrum of the laser, though, consists of a discrete carrier with 99.99% of the laser power and two sidebands with only 0.01% of the laser power. In this case the rms value gives a poor indication of the laser linewidth. As a second example consider an oscillation at a frequency of 10 Hz and of amplitude 1 kHz. The spectrum will now consist of a comb of intense harmonics about the suppressed carrier, out to about ± 500 Hz. In this second case $\Delta\upsilon_{rms}$ does provide a valid indication of the linewidth. From these examples it can be seen that $\Delta\upsilon_{rms}$ is a useful measure of the laser linewidth if a

bandwidth for the measurement is chosen that only includes the sideband frequencies which carry the majority of the laser power.

The appropriate bandwidth can be determined by examining the power spectrum of the phase noise of the error signal. Since $2\pi\Delta\upsilon(t)$ is the time derivative of $\varphi(t)$ the following relationship exists between $S_{\Delta\upsilon}(f)$ and $S_{\varphi}(f)$:

$$S_{\varphi}(f)=\frac{S_{\Delta\nu}(f)}{f^2} \tag{2.16}$$

When AM noise is negligible and the root-mean-square value of $\varphi(t)$ is much smaller than one radian, a simple approximate relationship between $S_{\varphi}(f)$ and the spectral density of the laser can be derived [Rutman 1977]:

$$S_{\nu}(f)=\frac{V_o^2}{2}\left\{\delta(f-\nu_o)+S_{\varphi}(f-\nu_o)\right\} \tag{2.17}$$

The continuous noise sidebands around the discrete carrier centred at υ_0 have the same spectral density as the phase noise. This approximation breaks down for oscillation frequencies close to the carrier frequency, where the modulation index of the perturbations can no longer be assumed to be much less than one 1. When the modulation index is not small compared to unity, sum and difference frequencies of the perturbations in the phase noise density power spectra will become significant in the optical intensity spectrum. The appropriate bandwidth for the rms measurement is chosen by selecting the lowest possible cutoff frequency that still complies with the relationship:

$$\int_{\nu_{cutoff}}^{\infty} S_{\varphi}(f)df << 1 \tag{2.18}$$

This relationship ensures that the majority of the laser power is associated with oscillations having frequencies within the measurement bandwidth.

2.3 Experimental apparatus and technique:

In this section the CR-699-29 dye laser and the reference cavity are described, followed by a description of the operation of the servo controller locking the laser frequency to a resonance of the cavity.

2.3.1 CR- 699-29 Dye Laser

Before describing the frequency stabilisation technique it is useful to review briefly the operation of the 699 ring laser (shown in Fig. 2.6). The CR-699-21 is a unidirectional travelling wave single mode dye laser capable of being scanned continuously over a 30 GHz range and it is actively frequency stabilised. The resonator consists of four mirrors with a cavity round trip length of 1.50 m. Three frequency selective elements in the resonator are used to force the laser to operate in a single longitudinal mode. Of major interest to us here is the single mode operation and the original active frequency stabilisation system.

Unidirectional Operation

The unidirectional, travelling wave operation is achieved by means of an optical diode. The optical diode employs a Faraday rotator, which rotates both forward and backward waves by the same amount and in the same direction. A reciprocal polarisation-rotating element then rotates back the forward polarisation into the plane of incidence of the Brewster plates in the laser cavity. For the backward wave the two rotations add and the increased reflection of the Brewster surfaces in the cavity result in a net loss. The additional losses incurred by the backward travelling wave allow the forward wave to dominate.

Single Frequency Operation

Single longitudinal mode operation of the CR-699-21 is obtained through the use of three frequency selective optical elements: a three-plate birefringent filter, a thin etalon and a thick etalon. The three-plate birefringent filter has a passive bandwidth of 380 GHz; its use in the CR-699 reduces the laser linewidth to 2 GHz. The thin etalon has a free spectral range of 200 GHz, its finesse is sufficient to enforce single longitudinal mode operation.

The use of the thick etalon permits the longitudinal mode to be scanned. The peak of one of the modes of the etalon is locked to the lasing cavity mode, increasing the losses in the neighbouring cavity modes. This allows the lasing cavity mode to drift off the peak of the thin etalon transmission without causing a mode hop. The error signal used in locking the thick etalon to the laser cavity mode is generated by dithering the thick etalon at 2 kHz and then monitoring the modulation at 2 kHz on the laser intensity.

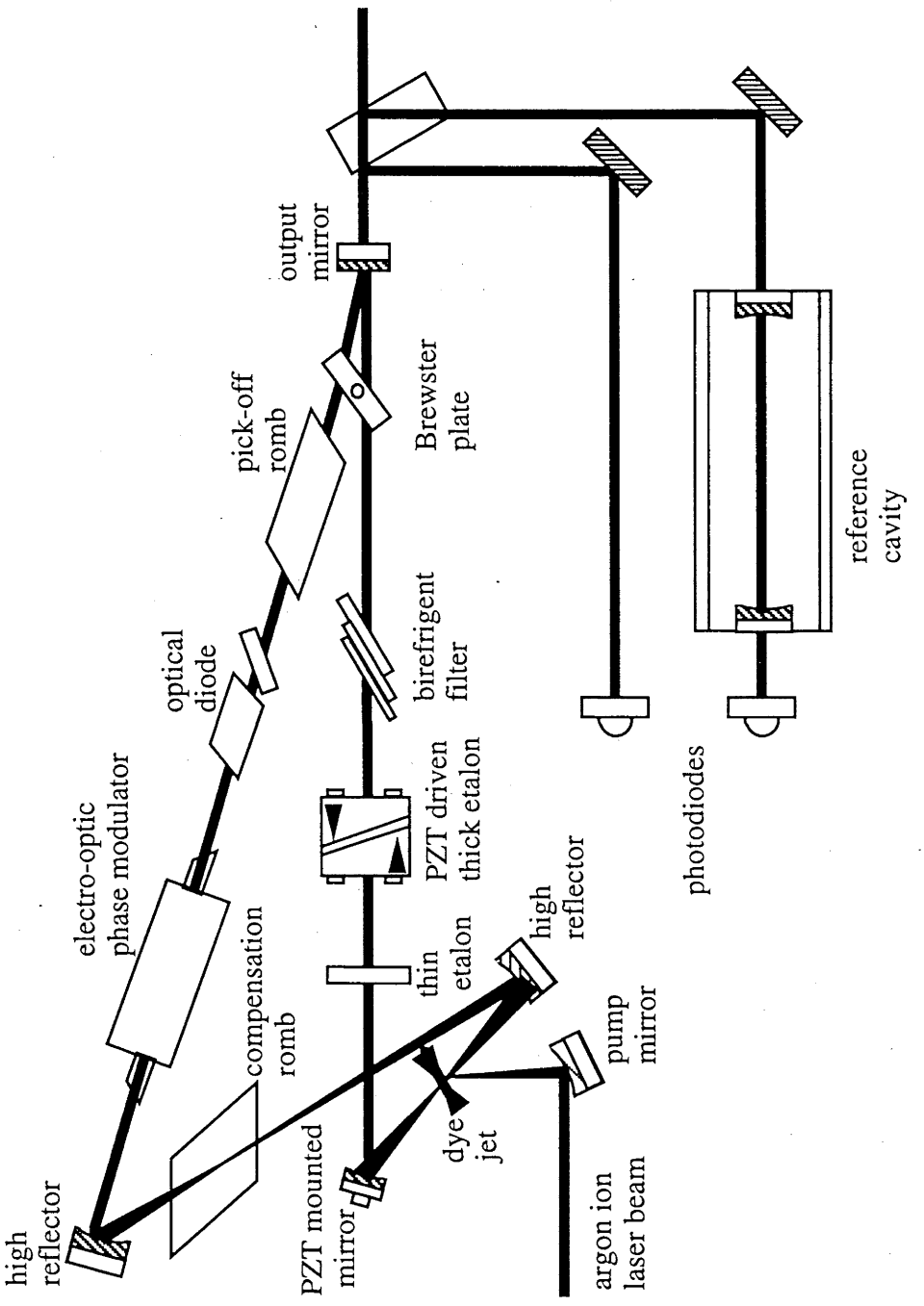

Figure 2.6. Schematic diagram of the optical arrangement of the CR-699-21 dye laser. The position of the electro-optic phase modulator added to the cavity is indicated.

When lasing in a single mode without active stabilisation the linewidth is approximately 20 MHz.

Single Frequency Scanning

In the CR-699, a galvo-driven Brewster plate, mounted at one vertex of the ring, is used to vary the length of the cavity and hence the frequency of the longitudinal mode. As mentioned above, the thick etalon automatically tracks this cavity mode. The thin etalon is tilted at rate such that its pass frequency follows the cavity mode. The laser frequency can be continuously scanned over 30 GHz.

Commercially Available Active Stabilisation

In its original configuration the 699-29 dye laser is actively stabilised by locking its frequency to a low finesse near-confocal cavity with a free spectral range of 1 GHz. The laser frequency is locked to the side of a transmission peak. The error signal is the cavity transmission normalised to the laser intensity. The bandwidth of the error signal is 70 kHz, limited by the photodiodes used to detect the cavity transmission and the laser intensity.

The frequency of the laser is adjusted with the use of the Brewster plate and the tweeter mirror, a mirror mounted on a piezo-electric stack. The servo that locks the laser to the reference cavity drives the Brewster plate at frequencies from DC up to 100 Hz whilst the tweeter mirror is driven at frequencies of a few hertz up to a few kilohertz. For both elements the upper frequency range is set by the existence of mechanical resonances at higher frequencies. When the laser is locked to the reference cavity the linewidth is reduced to 1 MHz.

Figure 2.7 shows the frequency spectrum of the error signal observed with the laser locked to the reference cavity using only the Brewster plate (the tweeter mirror being disabled). Between a few hundred hertz and 70 kilohertz this spectrum gives the frequency fluctuations present on a free running laser. It is apparent from this figure that there is an appreciable amount of frequency fluctuation on the laser output at frequencies exceeding the 2 kHz bandwidth of the commercial locking system. To narrow the laser linewidth down significantly below 1 MHz a servo bandwidth wide enough to attack these higher frequency fluctuations must be employed.

2.3.2 Reference Cavity:

A Newport "Supercavity" was used as the reference cavity for all the experiments covered in this thesis. The Supercavity has a free spectral range of 6 GHz. The radius of curvature of the two mirrors is 30 cm and the mirror separation is 25 mm. The mirror coatings were tuned to give a maximum finesse at 600 nm. When new, the manufacturer claimed a finesse of greater than 30,000 over the wavelength range 570 to 630, giving a FWHM of 200 kHz. The observed FWHM over this frequency range was typically 1 MHz however. The drop in finesse may have been due to aging or to possible optical damage due to high laser powers. The cavity was temperature stabilised to better than 50 μK, according to manufacture's specifications, thus reducing the thermal drifts of the cavity's frequency to the order of 100 kHz. One of the mirrors was mounted on a piezo-electric stack allowing the cavity's resonance frequency to be scanned over 30 GHz.

The Newport cavity assembly was bolted to an aluminium block which was in turn bolted to the optical table. No attempt was made to mechanically isolate the cavity assembly from the table. The table was vibrationally isolated from the floor.

The cavity was mounted 100 cm away from the output mirror of the ring laser. A single 15 cm focal length lens mounted approximately 12 cm away from the cavity's input mirror was used to couple the laser beam into the cavity. Typically 70% of the laser beam was coupled into the TEM_{oo} transverse mode of the cavity.

The Newport "Supercavity" was not designed as a frequency reference for stabilising lasers and hence has a number of limitations in this role. Of concern is the use of a PZT mounted mirror in the cavity, which leaves the cavity's frequency susceptible to electrical pickup. Also of concern is the poor vibrational and thermal isolation of the cavity. To overcome these limitations a custom built cavity was supplied to us by CSIRO. The cavity was based on a 50 cm long spacer made from a drilled-out rod of "Zerodur", it was surrounded by a heat shield and suspended by wires in a vacuum chamber. The cavity was temperature stabilised to 50 mK. The long term stability of the cavity's frequency measured over several hours was found to be better than 2 MHz [D. Gough 1993]. Unfortunately this cavity did not become available until after the completion of the experiment al work covered in this thesis.

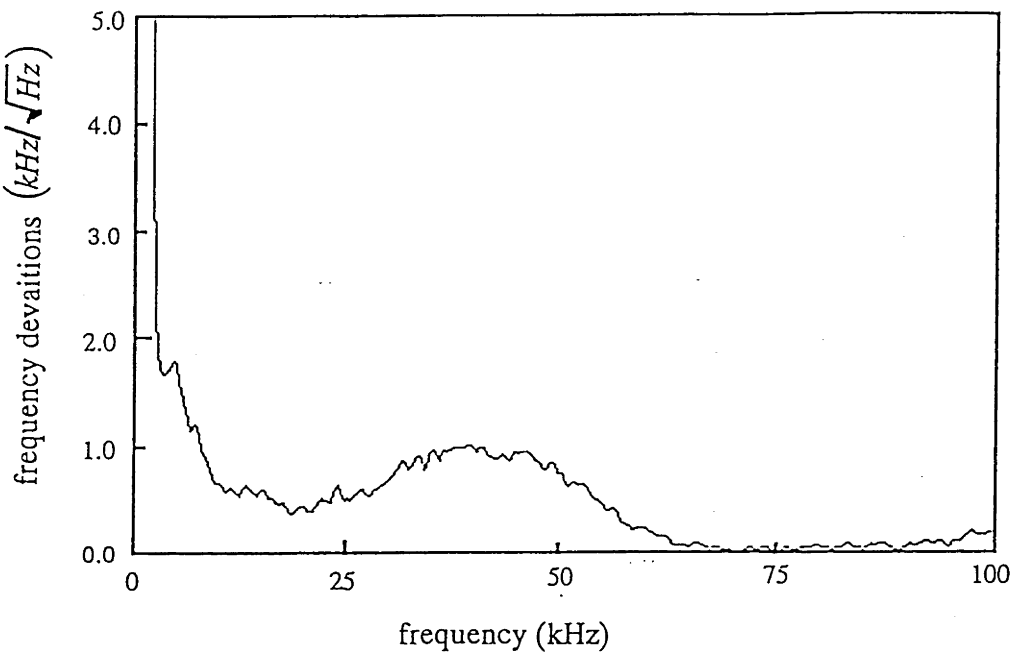

Figure 2.7. Spectrum of frequency noise on CR-699 dye laser with tweeter mirror disabled.

2.3.3 Description of laser stabilisation setup

As shown in the Fig 2.1, the schematic of the stabilisation system. A beam splitter is used to pick off a component of the laser beam. The beam splitter is made from an uncoated piece of glass 5 mm thick. The component reflected from the front surface, typically 10 mW, is phase modulated at 8 MHz by a Laser Metrics (now Fast Pulse Technologies) 1039D (KD*P) electro-optic phase modulator. The phase shift produced by the EOM is 6.28 mrad/λ per volt, with λ in μm. The rf drive amplitude to the EOM was $40V_{p\text{-}p}$. The modulation index at λ = 600 nm for this drive amplitude is 0.21. This results in about 5% of the total laser intensity incident on the cavity being transferred to each of the first order sidebands.

A single lens is used to couple the light into the reference cavity. The light reflected off the cavity is detected with a EG&G FND40 photodiode. In between the EOM and the coupling lens is a Faraday rotator (45^{o} rotation) followed by a linear polariser at 45^{o} to the vertical. There is also a vertical linear polariser positioned directly in front of the laser output and a horizontal linear polariser in front of the photodiode. The purpose of this arrangement is twofold. The first is to prevent the reflection from the cavity entering the laser (attenuation of reflected light is greater than 30 dB). The second is to reduce the interference on the photodiode between the reflected signal from the cavity and scattered light.

Figure 2.8 is another schematic of the locking system, showing the electronics in more detail. The signal from the photodiode goes to a preamplifier with a 30 dB gain, and then onto a second amplifier with 30 dB gain, and then a second order highpass filter rolled off at 4 MHz. This signal is mixed with an 8 MHz local oscillator with a 90^{o} phase delay. Care was taken to limit the amplitude of the harmonics of the 8 MHz local oscillator to -30 dB below the fundamental. A post-amplifier with a maximum gain of 20 dB and a bandwidth of 10 MHz boosts the error signal before it is used as the input to the servo controller amplifiers.

Three elements in the laser cavity are controlled, the Brewster plate, tweeter mirror and an electro-optic phase modulator mounted in the laser cavity.
The Brewster plate is driven by applying a signal to the scan input of the Coherent control box which is set to a scan range of 30 GHz. The Coherent control box is set to free run. In this mode the locking of the laser frequency to the coherent reference cavity is disabled and the Brewster plate in the laser cavity and the thin etalon are driven solely

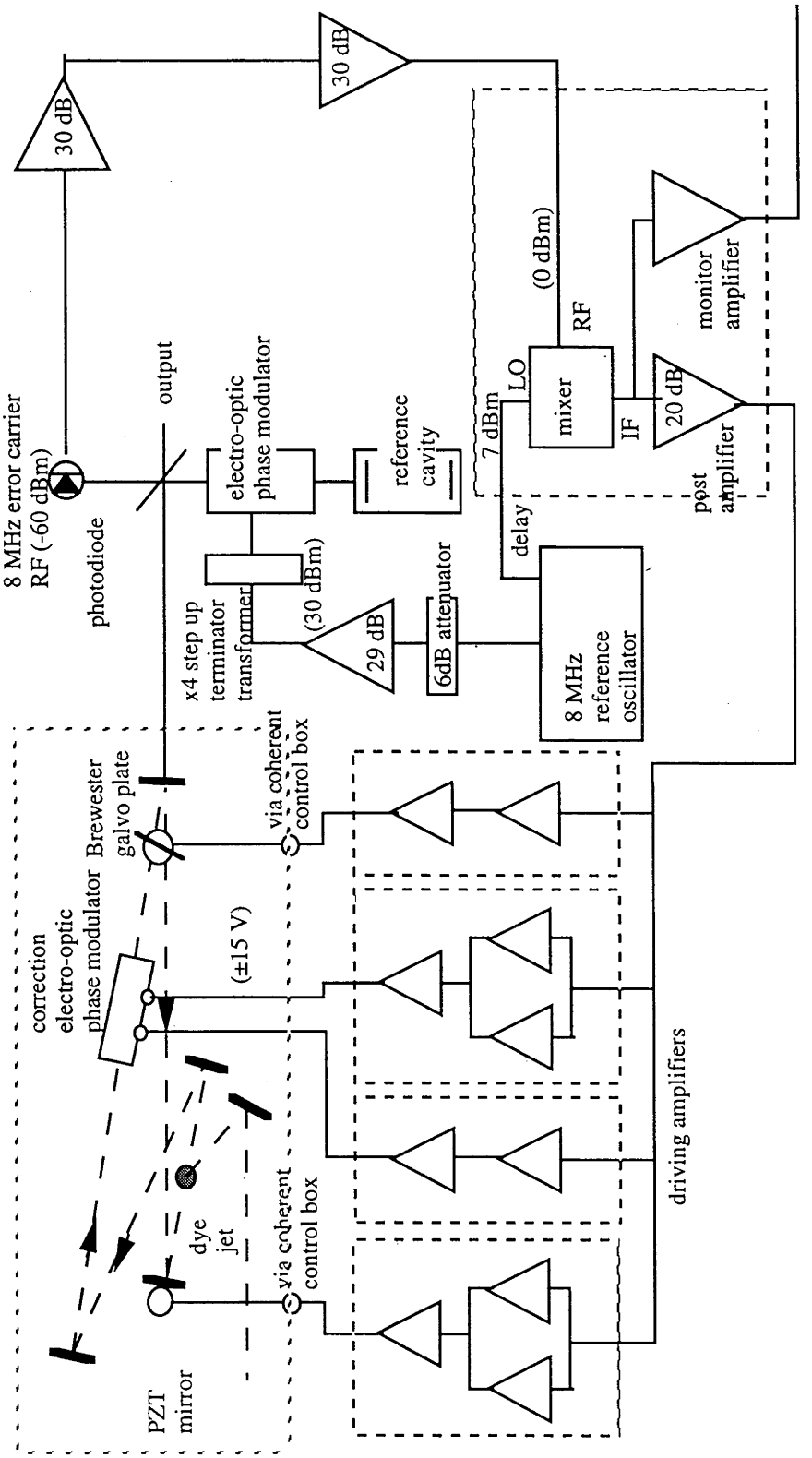

Figure 2.8. Schematic diagram of the frequency stabilisation system showing details of the electronics.

by the scan input via the feed forward amplifiers [see 699-29 manual]. The frequency response of the Brewster plate, determined by injecting a swept sine wave of known amplitude into the scan input and monitoring the frequency modulation on the laser using the Coherent error signal, is shown in Figure 2.9. The amplifier in the servo controller, used to drive the scan input, was a single integrator. The unity gain point of the integrator was continuously adjustable, and was typically set to about 100 Hz.

To drive the tweeter mirror, use was made of the tweeter drive in the Coherent control box. The error signal from the Coherent reference cavity on the input of the tweeter drive was interrupted and replaced with a signal from our servo controller. In a similar fashion to the Brewster plate the frequency response of the tweeter mirror was determined by injecting a swept sine wave of known amplitude into the tweeter drive and monitoring the frequency modulation on the laser using the Coherent error signal. The result of this is shown in figure 2.10. The output from two amplifiers are summed to drive the input to the coherent PZT drive. Typically only one amplifier was used with non-zero gain. The output from this amplifier was passed through a high pass first order filter rolled off at 50 Hz and then a first order low pass filter rolled off at 400 Hz.

The EOM mounted inside the laser cavity is a Gsanger low loss KDP phase modulator. The windows on the EOM are mounted at the Brewster angle for low loss operation. Its phase sensitivity is $6.28/\lambda$ radians per volt and its frequency response is flat out to 500 MHz. The EOM is mounted in the top arm of the laser's ring cavity, about 200 mm back from the top high reflecting mirror.

The frequency sensitivity of the laser to a voltage applied to the EOM is given by

$$\delta v = F.S.R\frac{6.28\times10^{-3}}{2\pi\lambda}\delta V \qquad (2.19)$$

where F.S.R is the free spectral range of the laser cavity. The Coherent 699 ring lasers have a free spectral range of 200 MHz, so for λ=0.6 μm a frequency sensitivity of 330 kHz/volt can be expected. The drive to the internal EOM produces a maximum voltage of 15 volts. This limits the maximum frequency shift that the EOM can correct to 5 MHz. The output of three amplifiers were summed to drive the inter-cavity EOM. The unfiltered frequency response of the first amplifier was flat up to 10 MHz, though in operation this was rolled off at 1.5 MHz with a first order low pass filter. The output of the second amplifier was rolled off with two first order filters with 3 dB points at 90 kHz and 40 kHz. The output of the third amplifier was similarly rolled off with two first

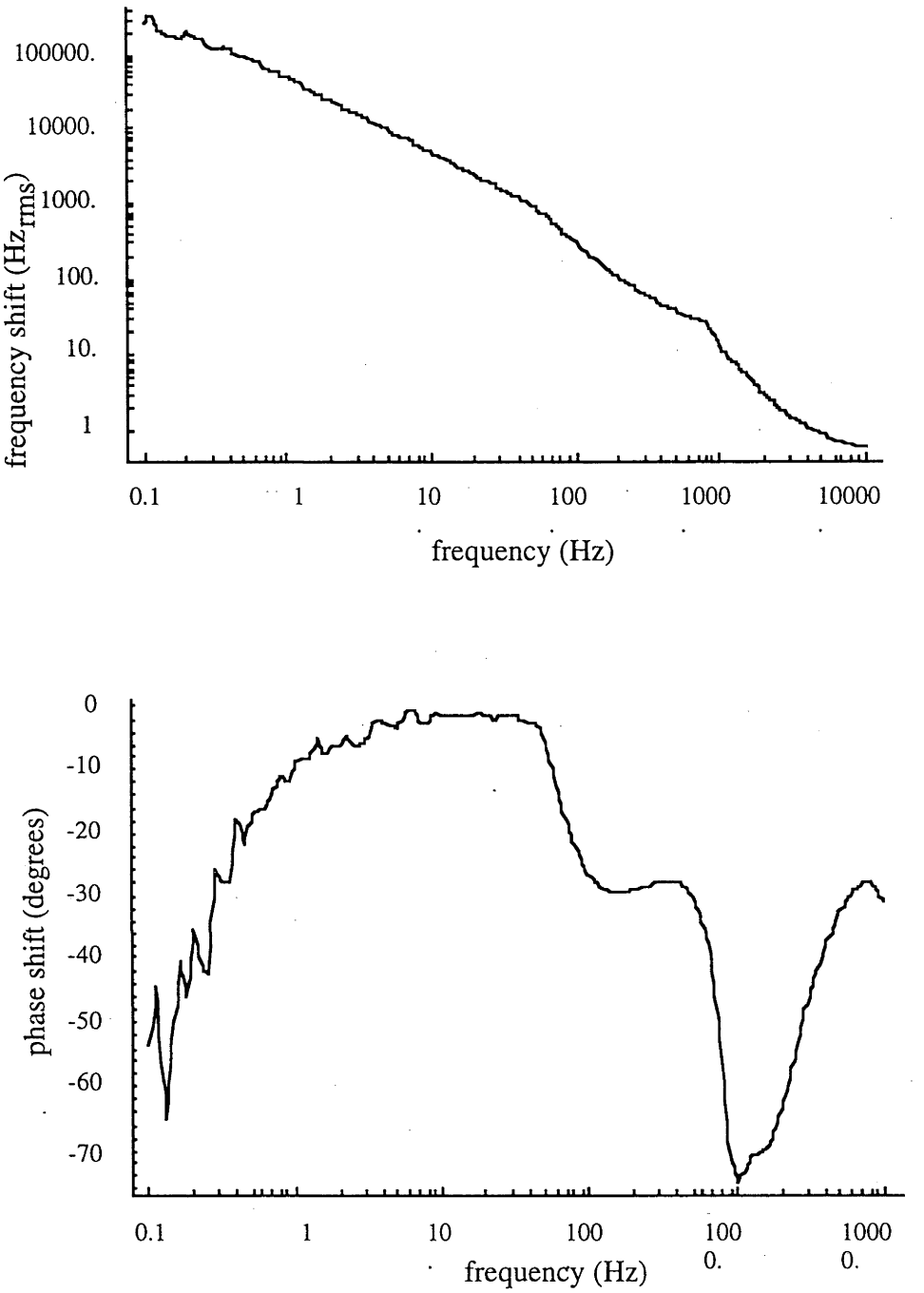

Figure 2.9. Frequency response of Brewster plate to a 1 Vrms signal, driven via the Coherent control box. Shown is the amplitude and phase of the frequency shift induced on the laser output. The scan range of the control box was set to 10 GHz

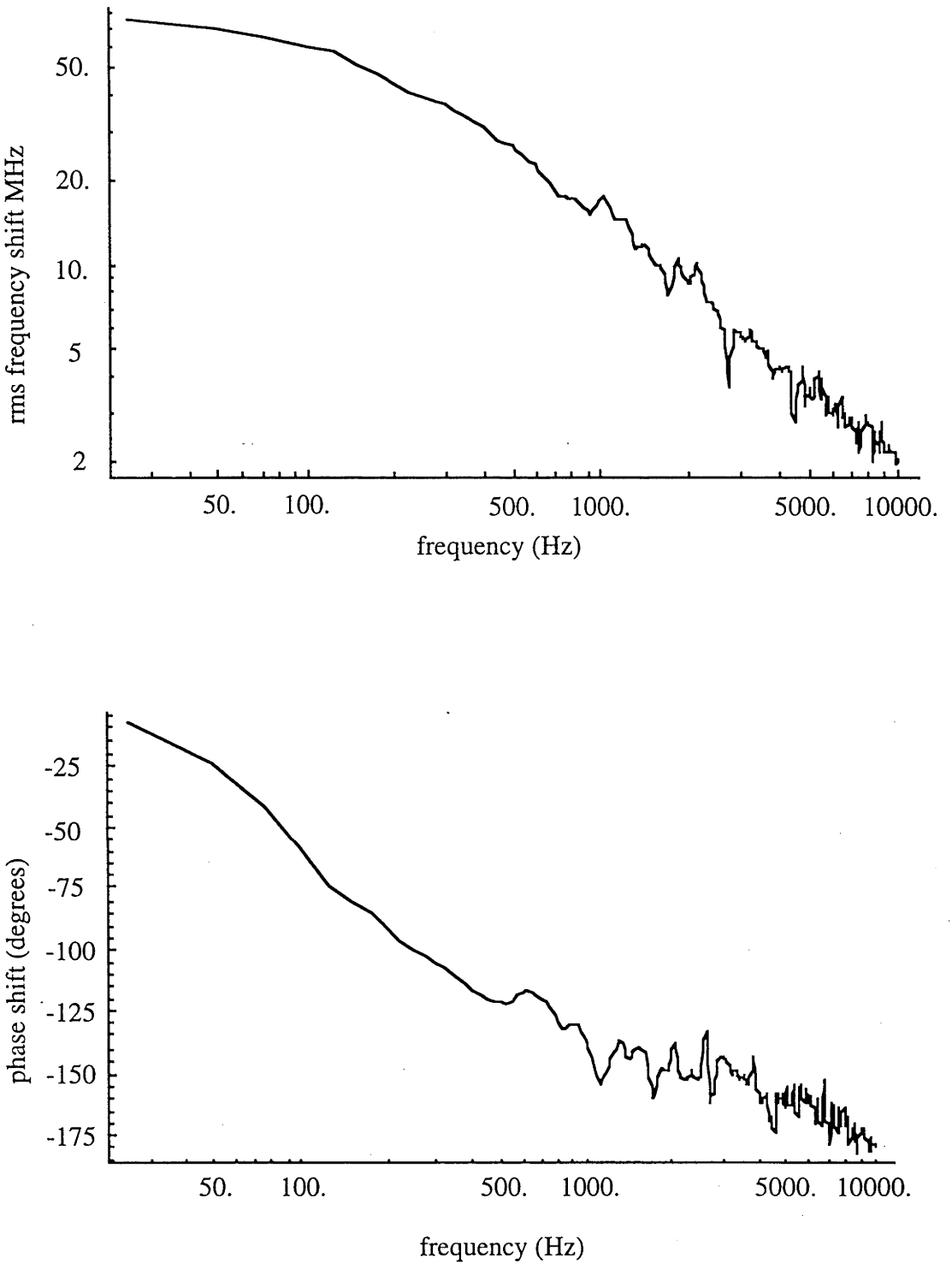

Figure 2.10. Frequency response of PZT mounted mirror to a 1 Vrms signal, driven via the coherent control box. Shown is the amplitude and phase of the frequency shift induced on the laser output.

order filters; in this case, with their 3 dB points at 90 kHz and 5 kHz. The total length of the servo loop was 6 m. Fixed delays in the amplifiers typically of the order of few nanoseconds was neglected.

Figure 2.11 shows the total gain of the servo, taking into account the response of all the elements in the loop. The response of the Brewster plate seen in Fig 2.9 was modelled as a pure integrator. The PZT response seen in Fig 2.10 was modelled by a first order filter rolled off at 100 Hz. The unfiltered response of the post and high frequency amplifiers were modelled as first order low pass filters. The unity gain point of the total servo gain is at 2.4 MHz, well above the rolloff frequency of the reference of 500 kHz.

2.4 Performance of stabilised laser

The linewidth of the Newport Supercavity resonance was measured by locking the laser to a second Newport Supercavity and scanning a resonance of the first cavity through the laser frequency. The FWHM linewidth was found to be 1.0±0.1 MHz for a laser frequency of 580 nm. Figure 2.12 shows the response of the error signal when the supercavity was tuned through the laser. For this measurement the laser frequency was set to 580 nm and was stabilised using the Coherent commercial system. The peak to peak voltage of the error signal was 4 V. Using Equation 2.5 the gradient of the frequency discriminator was determined to be 8.0 μV/Hz. The DC level of the error signal was found to be less than 1 mV away from ground, indicating an offset in the locking frequency of less than 125 Hz. To achieve this low offset level it was necessary to align the optical components so as to avoid any etalon effects due to stray reflections onto the photodiode. When stray reflections were present, the DC level showed a broad frequency laser dependence with offsets as large as 10 kHz.

To ascertain the amount of noise on the error signal the 8 MHz drive to the external EOM and all the feedbacks to the laser were disconnected. The noise left on the error signal is due to a combination of the amplifier noise, electrical pickup and shot noise on the photodiode. When the servo loop is closed this noise is injected onto the laser frequency. The rms value of this noise was observed to be 30 Hz_{rms} for a measurement bandwidth of 100 kHz. The expected contribution from the shot noise can be estimated from using Equation 2.15 and the shot noise spectral density calculated in section 2.2.4. For a shot noise level of .04 $Hz/\sqrt{Hz}$ and measurement of 100 kHz the rms value of the shot noise should be 13 Hz. This indicates that shot noise limited detection was not achieved. The noise on the observed signal was in fact found to be dominated by 50 Hz harmonics, attributed to pickup from the mains.

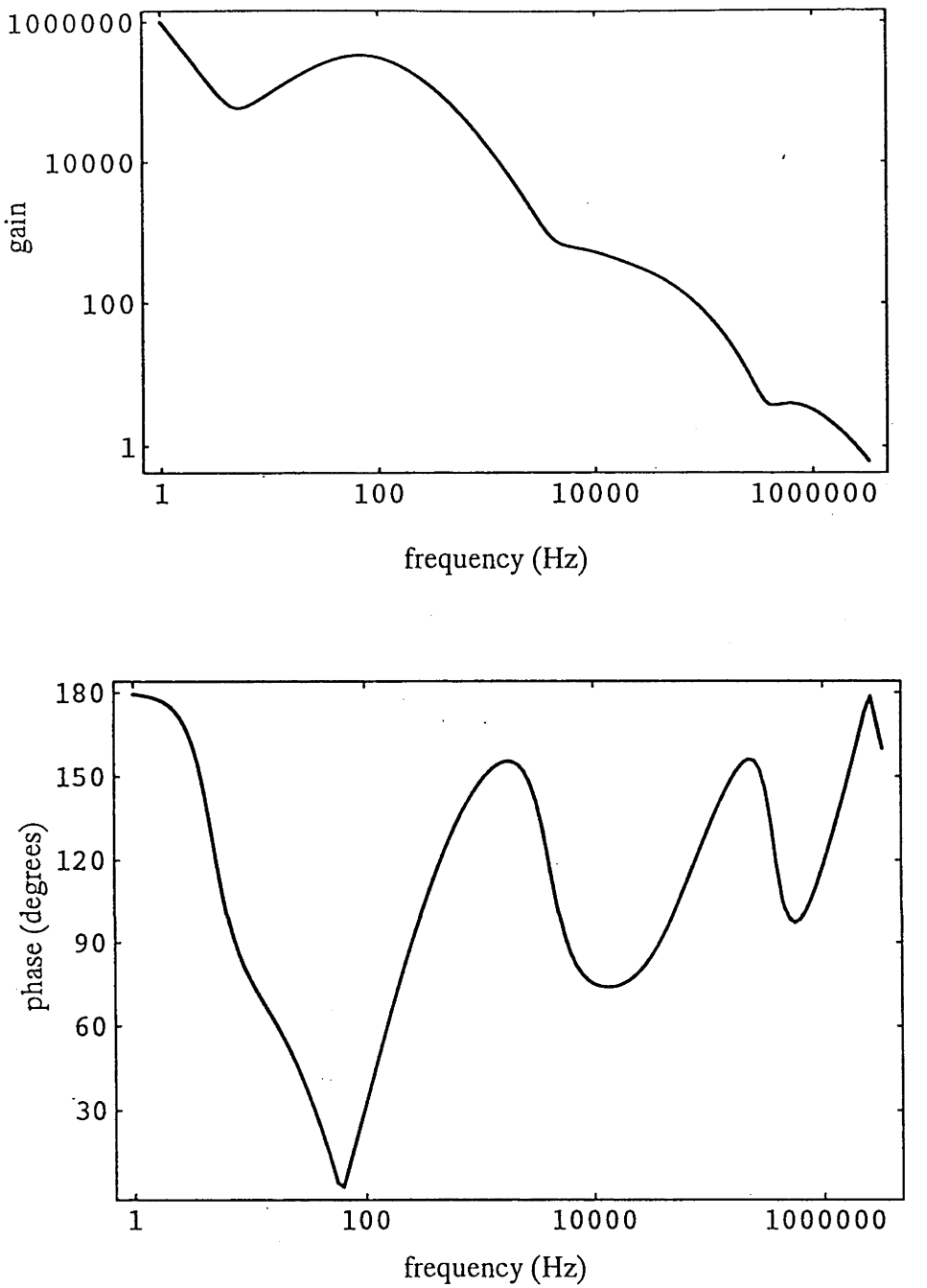

Figure 2.11. Total gain and the phase shift around the laser stabilisation servo-loop, as a function of frequency.

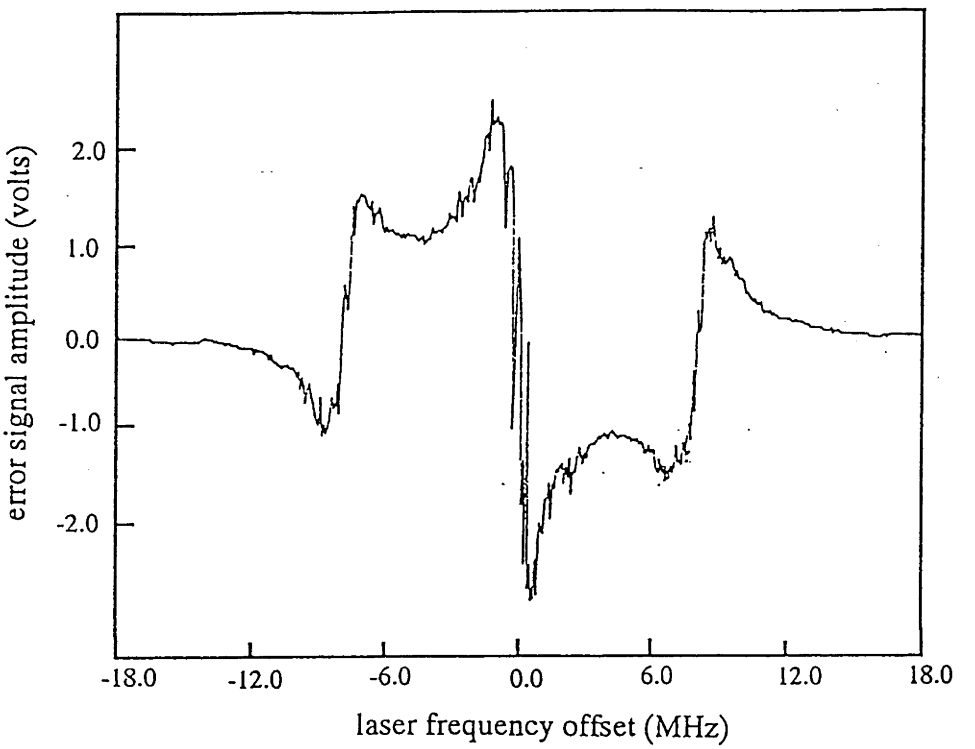

Figure 2.12. Observed DC response of the error signal.

When the laser was locked to the cavity resonance the frequency fluctuations observed on the error signal had a rms value of 2 ± 0.2 kHz_{rms} for a measurement bandwidth of 1 MHz. For a measurement bandwidth of 10 kHz the frequency fluctuations were 200 ± 50 Hz_{rms}.

Figures 2.13 a, b and c show the spectral noise density of the error signal when the laser is locked. The scans were recorded using a HP FFT analyser, over the frequency ranges 0-400 Hz, 6.4 kHz and 100 kHz for Figs 2.13 a, b and c respectively. Comparing Figure 2.13 with the frequency noise spectrum of the unlocked laser (shown in Fig 2.7) it can be seen that the noise density has been reduced from about $1000\ Hz/\sqrt{Hz}$ to about $2\ Hz/\sqrt{Hz}$ in the 100 Hz to 50 kHz range. The residual noise level is still well above the limit set by the shot noise in the detection system. This residual noise is due to electrical pickup in the servo controller and to the finite gain of the servo loop. The frequency noise spectrum was also observed in the 50 kHz to 5 MHz range. Using an rf spectrum analyser it was found to have a value peak of $10\ Hz/\sqrt{Hz}$ at 2 MHz close to the unity gain point of the servo.

The phase noise density spectrum, derived by dividing the frequency noise density spectra in Figs 2.13 a, b and c by the fluctuation frequency, is shown in Figs 2.14 a, b and c. As discussed in Section 2.2.5 this spectrum corresponds to the optical intensity spectrum for frequencies sufficiently removed from the carrier. By integrating the square of the phase noise density spectrum from 500 Hz to 100 kHz it was found that only 5% of the laser power is associated with oscillations above 500 Hz. Hence a measurement bandwidth of 10 kHz in measuring the rms value of the instantaneous frequency noise is likely to give a result which is an upper limit on the linewidth. Therefore the FWHM linewidth of the laser is of the order of 400 Hz, twice the rms frequency fluctuations observed using the 10 kHz measurement bandwidth.

2.5 Conclusion

In this chapter we have discussed the modification of a commercial high-resolution ring dye laser to improved the linewidth. Analysis of the error signal shows we have satisfactorily locked the laser frequency to a resonant frequency of the cavity to within 400 Hz. Of course if the cavity is unstable the linewidth of the laser will be greater than the 400 Hz value determined. In the following chapter the absolute stability of the laser will be investigated using the experiment technique of spectral holeburning.

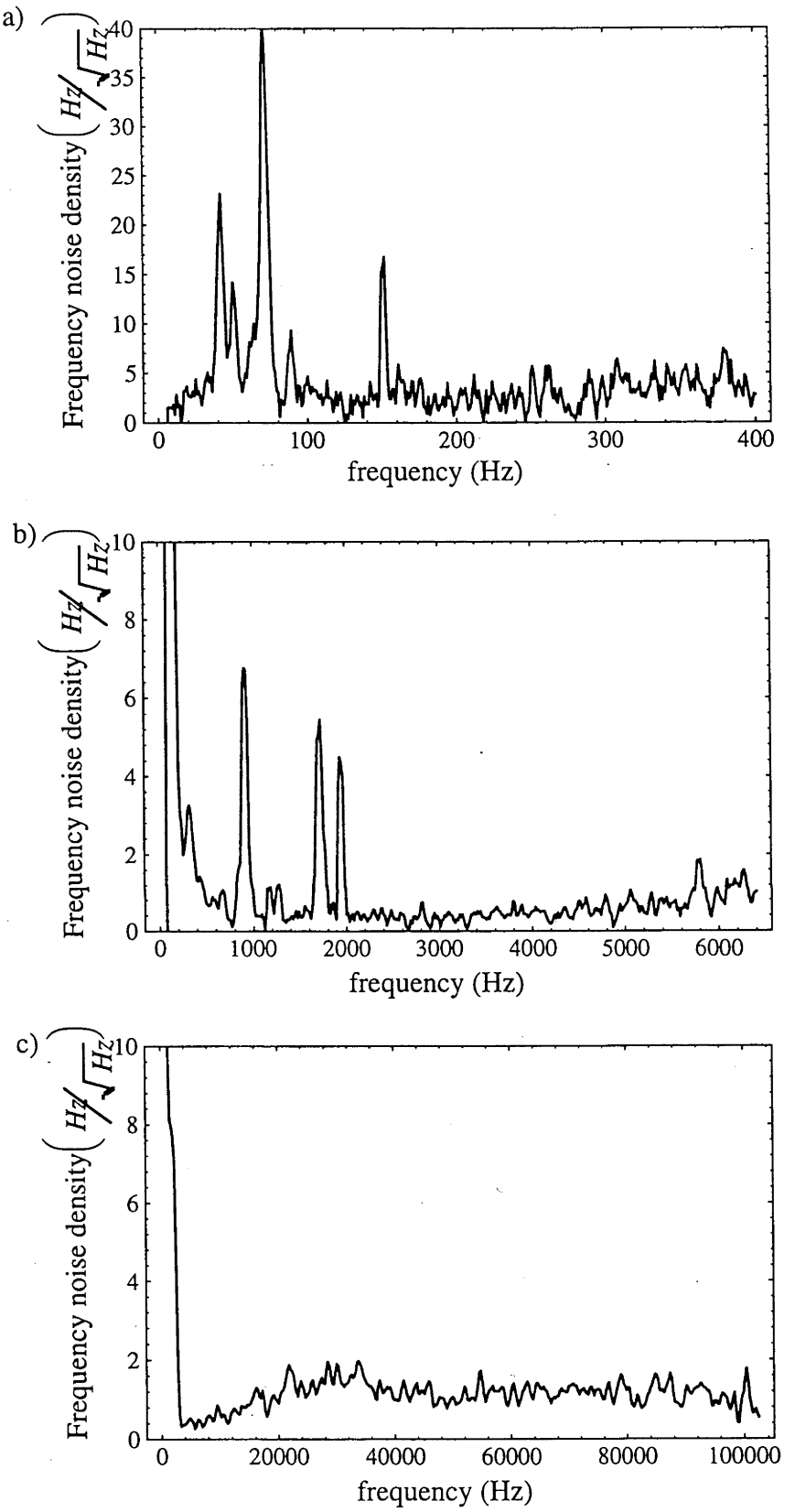

Figure 2.13a, b and c Spectrum of the frequency noise density of the error signal. Trace a) is over the range 0 ⇒ 400 Hz, trace b) 0 ⇒ 6.4 kHz and trace c) 0 ⇒ 100 kHz.

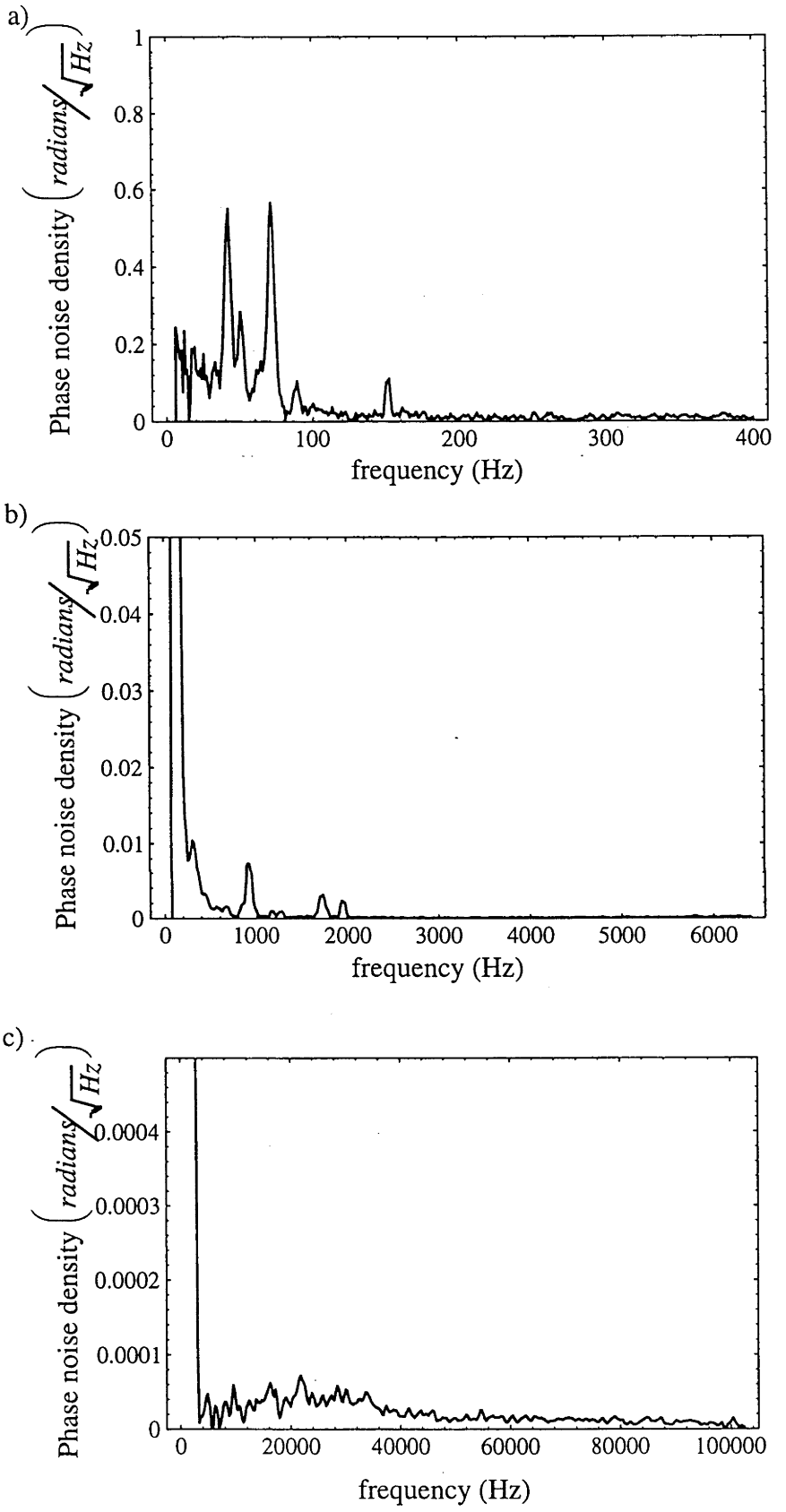

Figure 2.14a, b and c Spectrum of the phase noise density of the error signal. Trace a) is over the range 0 ⇒ 400 Hz, trace b) 0 ⇒ 6.4 kHz and trace c) 0 ⇒100 kHz.

Chapter 3 Ultra-narrow holeburning in $Y_2O_3:Eu^{3+}$

3.1 Introduction

This chapter reports spectral holeburning measurements performed on the $^7F_0 \Rightarrow {}^5D_0$ transition of Eu^{3+} doped in Y_2O_3. The investigation has two parts. In the first part a measurement of the spectral hole linewidth is made. The linewidth will be compared with linewidths obtained from previous time domain photon echo measurements on the same crystal. It is possible that the linewidth determined by two different techniques will differ and there are at least three reasons for this.

The simplest is that the laser linewidth or jitter contributes to the spectral holeburning measurement, but not to the photon echo measurement. Secondly, because the two techniques excite different densities of ions, the dephasing due to the excitation of adjacent ions (instantaneous spectral diffusion) will contribute in differing amounts to the observed linewidths and hence can result in different values. Finally, photon echoes and spectral holeburning operate on different time scales and this can also lead to the observation of different linewidths. Despite these factors it is expected that a sample with narrow time domain measurement will give narrow frequency domain values. Assuming this aspect is realised in the experimental measurements the investigation has a second objective. The second aim of the holeburning measurements is to use the narrow spectral hole as a frequency marker for characterising the frequency stability of the laser.

In the previous chapter the performance of the servo-controller locking the laser frequency to a mode of a reference cavity was determined by examining the servo-controller's error signal. This gives an indication of how the frequency of the two cavities, laser and reference, vary with respect to one another. The frequency stability of the laser depends not just on the performance of the servo-controller but also on the stability of the reference cavity. To determine the stability of the laser system it is necessary to compare its frequency to a frequency reference which is at least as stable as the laser, and preferably superior. In this work we will show how a spectral hole can be used as the stable frequency reference.

A conventional approach is to construct a second stabilised laser system and direct the output beams of the two laser systems onto a photodiode. The electrical output of the diode indicates the beat frequency between the two lasers. Assuming that the frequency changes of the two lasers are equivalent but not correlated, the stability of the two lasers can be determined by monitoring the changes in the beat frequency. This approach

requires extreme care in isolating the two lasers to obtain a reliable indication of the absolute stability. In view of this, and the cost of the required experimental resources this approach is not used here.

A second approach is to compare the laser frequency with a sharp atomic transition. For linewidths approaching kHz this approach requires constructing fairly sophisticated atomic traps or an atomic beam, and the laser must at the outset have a linewidth of the order of the atomic transition before the technique will be successful. The technique is capable of giving an absolute stability (and absolute frequency) but it must be appreciated that the measurements, although conceptually simple, require considerable technical sophistication. Pursuing such an approach required a complex apparatus and lacked relevance to the research direction of this laboratory.

The method attempted here is to use spectral holes as frequency references. The approach was readily accessible, as spectral holeburning itself represents the end utilisation of the laser development. In our laboratory the approach is certainly more straightforward. It is not claimed that the method is necessarily better than utilising atomic transitions and it is recognised that it does not give an absolute frequency determination, but there are some advantages over using atomic transitions. For example, the hole is used to create the frequency reference and in so doing it leads to the frequency reference being at or (afterwards) very close to the operating frequency of the laser. In addition, the frequency marker (the hole) has the same resolution as the laser. As discussed below, a broadband laser will burn a broad hole and a narrowband laser will burn a narrow hole. The frequency reference even improves as the system performance improves. Both factors are convenient and are by no means the case with atomic reference sources.

3.2 Holeburning procedure

To determine the linewidth of the laser over short time scales, the same laser was used to both burn and then measure the width of the spectral hole. The resultant hole linewidth gives a measure of the laser frequency jitter over the holeburning (and probe) period. It is claimed that the hole is a spectral feature which does not alter in frequency and, hence, can be used as a frequency reference. The reliability of the hole as a stable frequency marker will be discussed later in the chapter. The limiting resolution that can be achieved is set by the homogeneous linewidth of the holeburning sample. It is essential to use materials which exhibit very narrow homogeneous linewidths and the optimum materials are discussed in the next section.

Longer term laser drifts can also be measured by a holeburning technique. A variable delay is introduced between the holeburning phase and the probe. A movement of the measured hole position actually represents a movement of the laser frequency, and so a series of such measurements can be used to track the laser drift over time. The holeburning technique can therefore be used to determine laser stability over time scales ranging from the minimum holeburning period to the lifetime of the hole.

There is a further involvement of holeburning in this work. It is shown how an error signal can be generated from the transmission of the spectral hole by utilising a "Pound-Drever" method as discussed in Chapter 2. The error signal is found to be invaluable for establishing the presence of various instabilities and this knowledge has been used to further improve the overall laser stability.

3.3 Holeburning material

When an optical excitation pumps a centre from a resonant into a non-resonant state, there will be a bleaching effect at the excitation frequency. When the procedure is associated with an inhomogeneously broadened transition, the effect gives rise to spectral holeburning. The hole lifetime will be determined by the characteristic time it takes for the centre to return to the original ground state. The minimum width of the hole burnt is limited by the homogeneous linewidth of the optical transition (note that other effects can add to this width). For narrow spectral holes, therefore, it is necessary to utilise materials with narrow homogeneous linewidths.

As discussed in Chapter 1 the homogeneous linewidths of transitions associated with rare-earth centres in crystals cooled to liquid helium temperatures can be very narrow and are likely candidates for providing the necessary sharp spectral reference holes. The reason for the narrow transitions of rare earth ions lies in the fact that the open shell of f electrons is well screened from the lattice and so is barely affected by the static or dynamic crystal field. To minimise the hole linewidth there are a number of additional considerations. The transition should be associated with long lived states, since the radiative lifetime (T_1) determines the limiting linewidth. Furthermore, as magnetic interactions can cause broadening, it is best to select systems where the magnetic moments are absent or small. This can be achieved by using centres with no electronic moment and host materials with little or no nuclear moments.

The ion which best matches the conditions described above and exhibits the narrowest spectral holes is Eu^{3+}. The transitions in Eu^{3+} take place between two electronic states, $^7F_0$ and $^5D_0$, neither of which have a first order electronic magnetic moment. There are nuclear moments of the order of 1 kHz/G but these cannot be eliminated, as hyperfine levels are essential for the population storage in the relevant holeburning process.

Selecting host lattices with no electronic or nuclear spins would suggest utilisation of oxygen, calcium or sulphur, as the naturally abundant isotopes (<99%) of these atoms do not have nuclear spin. To date however, the host crystals exhibiting the narrowest lines have involved oxygen, silicon and yttrium. None of these components have an electronic moment. The naturally abundant isotopes of oxygen (O^{16} 100%) and silicon (Si^{28} 92.2%) have no nuclear spin. The yttrium nucleus(Y^{89}), does have a nuclear spin, but the moment is small (210 Hz/G). The narrowest reported homogeneous linewidths have been generated using Y_2SiO_5 and Y_2O_3 crystals doped with Eu^{3+}. The linewidths of these systems can be measured in the time domain using photon echoes and the reported values are 122 Hz for $Y_2SiO_5:Eu^{3+}$ [Equall *et al.* 94] and 625 Hz for $Y_2O_3:Eu^{3+}$ [Macfarlane *et al.* 1981a]. $Y_2O_3:Eu^{3+}$ was used in the present work, due to the availability of a suitable sample

The particular $Y_2O_3:Eu^{3+}$ sample used has been studied by a number of previous authors [Macfarlane *et al.* 1981a, Flinn *et al.* 94]. The sample was grown by the Verneuil process, with a measured Eu^{3+} concentration of 0.3%. The $^7F_0 \Rightarrow {}^5D_0$ transitions at 580.8 nm, associated with the C_2 sites, exhibited an inhomogeneous linewidth of 5 GHz. The lifetime of the excited state has been observed to be 900 μs [Sellars *et al.* 1994]. The dephasing time, determined by photon echo measurements performed in the wings of the inhomogenously broadened line (2 GHz from line centre), at a temperature of 1.8 K, was T_2=510 μs [Macfarlane *et al.* 1981a]. This implies a linewidth of 625 Hz. At line centre the dephasing time was found to be T_2= 130 μs. This increased rate was believed to be due to a greater susceptibility to instantaneous spectral diffusion of the ions nearer line centre rather than to an intrinsically larger homogenous linewidth [Macfarlane *et al.* 1981a].

3.4 Spectral holeburning measurement technique

A frequency-modulated spectroscopy technique similar to that demonstrated by Bjorklund [1980] is used for the holeburning measurements, and the measurements are discussed in this section.

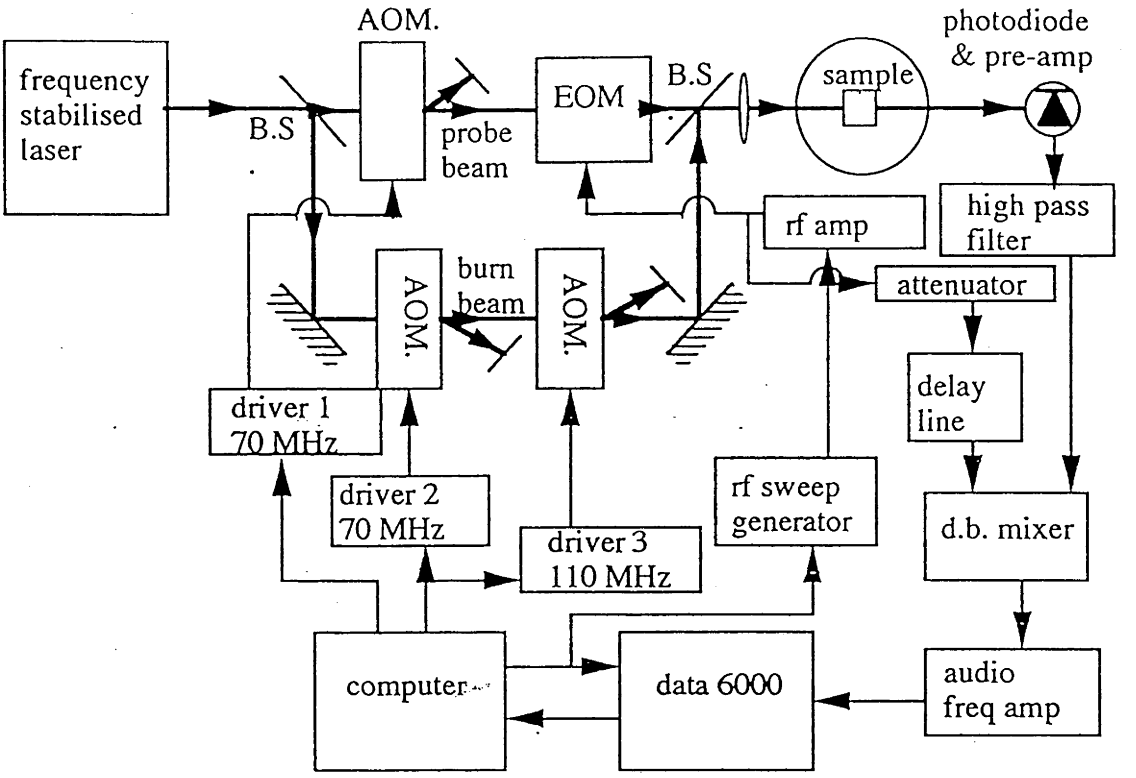

Figure 3.1. Shematic diagram depicting the experiment setup for FM detected holeburning spectroscopy. AOM; acousto-optic modulator, EOM.; electro-optic modulator, B.S.; Beamsplitter.

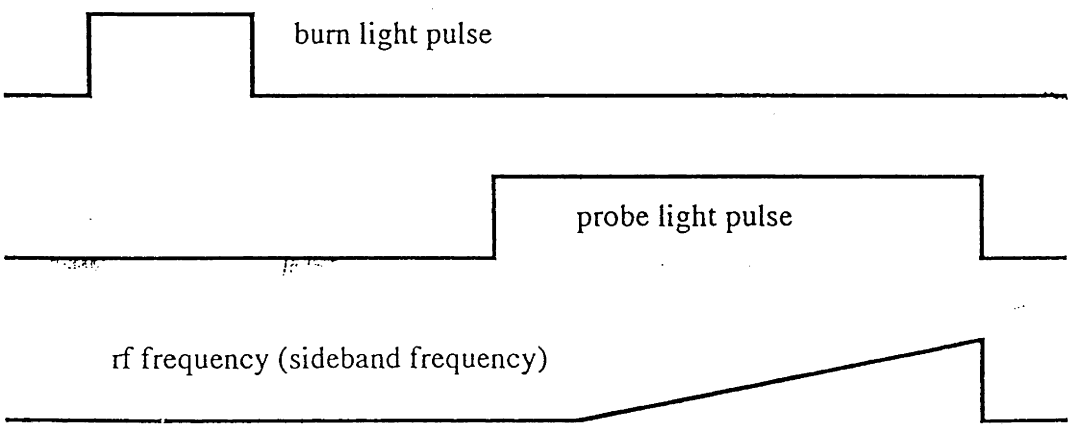

Figure 3.2 Laser and RF pulse sequence.

The output of the frequency stabilised dye laser is divided by a 50:50 beam splitter (see Fig 3.1). The frequency of one of the beams is upshifted by 40 MHz using a combination of two acousto-optic modulators, one driven at 110 MHz, the other at 70 MHz, to form the burn beam. The second beam is upshifted by 70 MHz with a single acoustic-optic modulator. An electro-optic phase modulator (Lasermetric 1039B) is used to frequency modulate the second beam. The resultant sidebands are swept about a centre frequency of 30 MHz, the difference frequency of the two beams. One of these sidebands forms the probe beam. The two beams are recombined on a second beam splitter and passed through the sample onto a photodiode (New Focus 125 MHz bandwidth). The optical and rf pulse sequence is shown in Fig 3.2.

Sweeping the rf frequency driving the electro-optic modulator causes one of the sidebands on the probe beam to pass through the optical hole created by the burn beam. This results in a change in both the phase and the amplitude of the sideband, producing an amplitude modulation on the transmitted light at the sideband frequency. The resultant electronic signal from the photodiode is then phase detected, with the swept rf used as the local oscillator. The main sources of noise in this technique are the frequency fluctuations of the probe beam within the holes it creates. This noise is almost completely restricted to the dispersive phase, thus still permitting a good signal-to-noise-ratio for the detection in the absorptive phase. This situation is very similar to the generation of the error signals presented in Chapter 2: changes of frequency give large changes at the locking frequency in the dispersive phase but not in the absorption phase (see Fig 2.2).

As will be shown later the electrical connections to the Newport Supercavity used as the reference cavity gave electrical pickup which resulted in frequency instability. For the highest resolution measurements the scan drive and the temperature controller circuitry were disconnected. Without the active temperature stabilisation of the supercavity the long term stability of the laser was degraded but the short term stability was significantly improved. To minimise the thermal drifts the cavity was encased in a polystyrene box.

3.5 Results: Holewidth

The holeburning pulses were varied between 0.4 ms and 4 ms long, with a power of 100 μW, and focused down to a diameter of about 200 μm. The power in the probe beam was typically 500 μW, with about 0.1% of this in each of the first order sidebands. To minimise undesirable holeburning associated with the probe beam, the probe beam was

gated on only during the measurement period. The narrowest holes were detected by scanning of the sidebands over a frequency ranges of only 100 kHz, with a scan time of 20 ms. The scan frequency ranges and times were adjusted according to the holewidth so as to minimise contributions to the width from bandwidth considerations.

The narrowest lines are obtained at low temperature and Fig 3.3 shows a typical single-scan spectrum taken with the temperature at 2.2 K. It is seen that the FWHM of the hole is 3.5 kHz. In other scans there are examples where the laser does not remain stable. Scans with two peaks were observed as shown in Fig 3.4, suggesting a sharp frequency jump of the laser frequency during either the burn or read periods. These jumps were of the order of 5 kHz. After averaging the widths of ten scans that did not show double peak structure, a hole width of 3.7±1 kHz was obtained. This width is attributed to contribution from laser jitter and the transition homogeneous linewidth.

To confirm that the observed lines are associated with holeburning in the $Y_2O_3:Eu^{3+}$ system a series of measurements were made for temperatures between 2.2 K and 14 K. The experimental values are plotted in Fig 3.5. Over this temperature region the variation of the transition's homogeneous linewidths is known from photon echo measurements. For example, experiments by Babbit *et al.* [1989] found a T^7 dependence on temperature consistent with a Raman phonon process. The prediction of the temperature dependence of the hole linewidth based on these latter photon echo results $[2(\pi T_2)^{-1}]$ is also plotted as a solid line curve in Fig 3.5. It is found that there is a close correspondence between the holeburning and the photon echo results for temperatures above 8 K. This evidence is taken as confirmation that the features do indeed arise from spectral holeburning. The deviation between the two methods at temperatures below 8 K and, in particular the larger linewidth in the case of the holeburning measurements is attributed to the increased contribution of the laser jitter, power broadening and the finite pulse length used to burn the hole.

By extending the delay between burning the hole and probing it to 1 sec, and measuring the offset of the hole frequency, the long term drift of the laser frequency was observed to be typically 100 kHz/s.

3.6 Generation of error signal from a spectral hole

Fig 3.6 is a schematic diagram of the experimental setup used to produce a frequency discriminator from a spectral hole. The principles are the same as for the error signal generated from the reference cavity. More significantly, the actual experimental

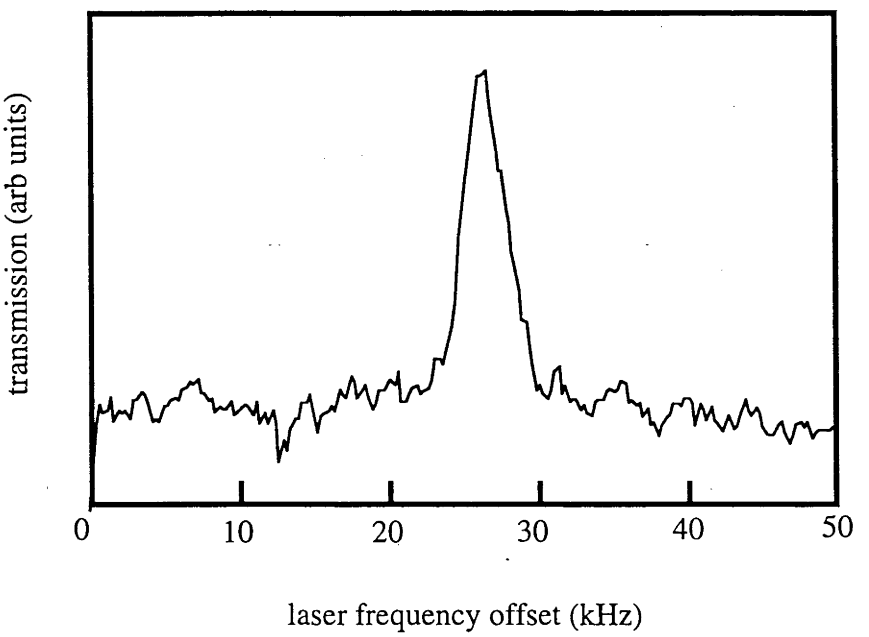

Figure 3.3 Optical hole-burning spectrum in $Y_2O_3:Eu^{3+}$ at temperature of 2.8 K. The hole was burnt with a 100 μW (~300 mW/cm^2) pulse, 2ms long. The sidebands were swept at a rate 5 kHz/ms. The delay between burning the hole and reading it was approximately 10 ms.

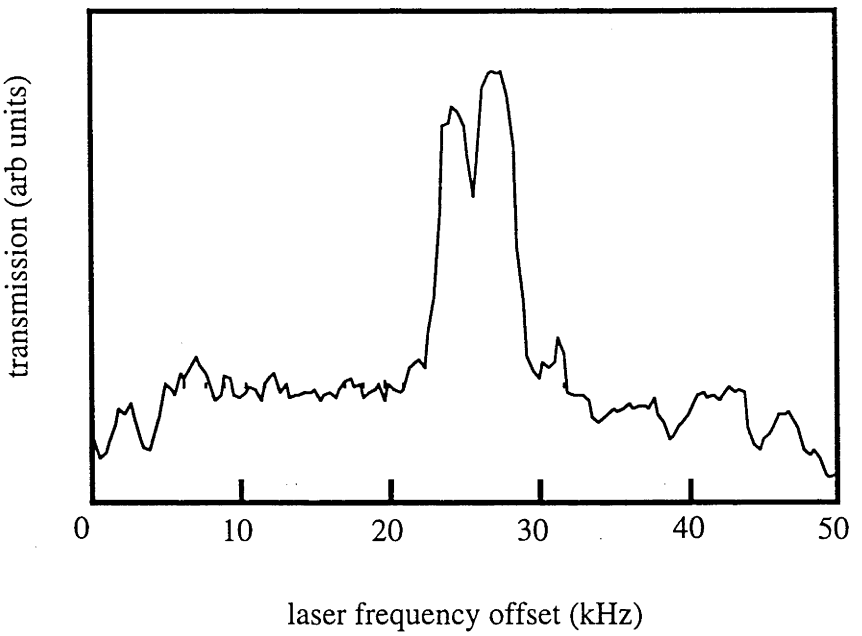

Figure 3.4 Optical hole-burning spectrum taken under the same conditions as in Fig 3.3, but where the laser has taken a frequency jump.

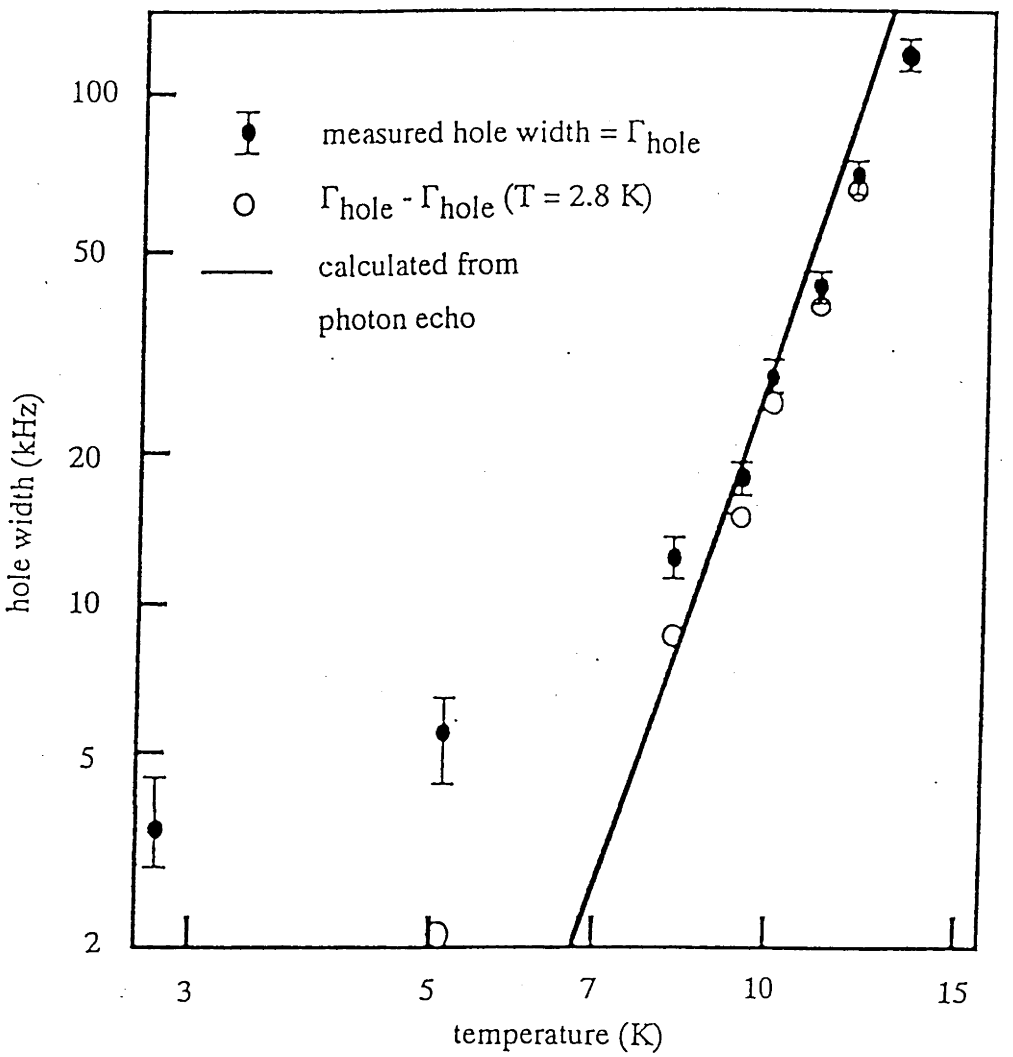

Figure 3.5 Temperature dependence of the optical hole width for $Y_2O_3:Eu^{3+}$. The hole width predicted from the photon echo results by Babbit *et al.* [1989] is shown by the solid line, which shows the T^7 behaviour associated with a two phonon Raman process.

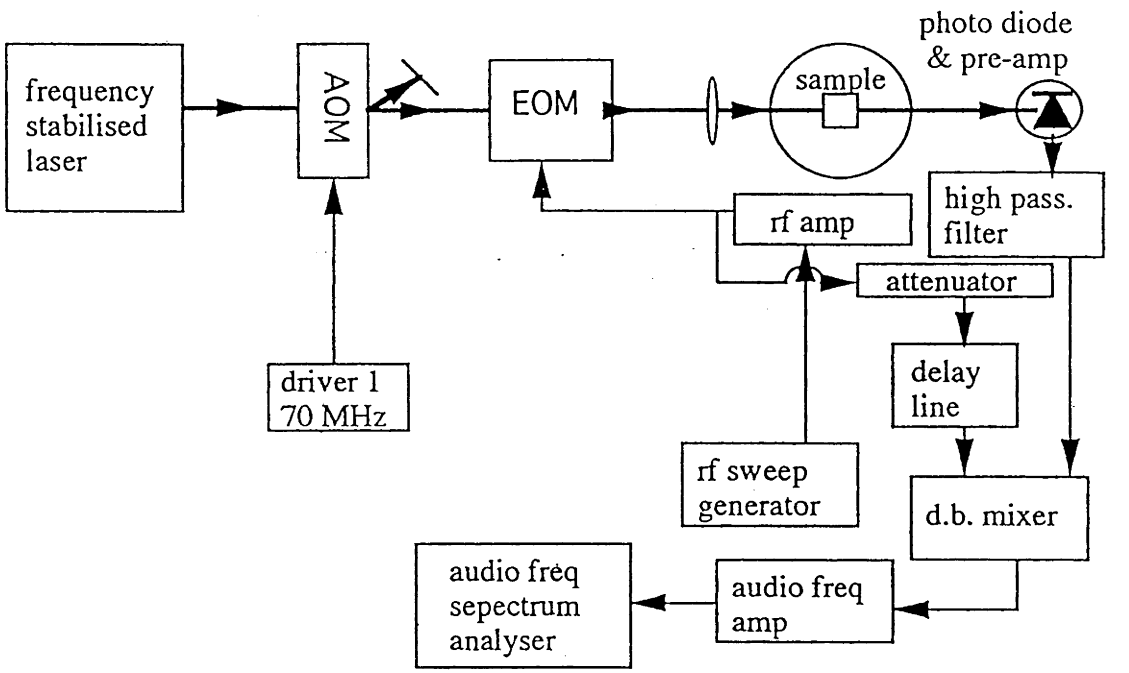

Figure 3.6 Shematic diagram depicting the experiment setup for generating a frequency discrimantor from a spectral hole. AOM; acousto-optic modulator, EOM; electro-optic modulator, B.S. Beamsplitter.

arrangement is similar to that used for the FM holeburning described above, but without a separate burn beam. With a 1 mW beam, and the sideband frequency fixed at 30 MHz, the transmission signal from the photodiode is mixed with a local oscillator delayed by 90 degrees. The resulting double-balanced mixer signal was displayed on an audio frequency spectrum analyser which could be averaged for improved display.

Fig 3.7 shows a comparison between the frequency spectra of the signal derived from the sample and the error signal from the laser stabilisation servo over a frequency range of 0 - 100 kHz. The spectra are very similar, with the main difference being the higher background of the error signal derived from the sample. It was not possible to calibrate this error signal as the width of the hole burnt by the laser over an extended period was not known. The gain at high frequencies of the laser stabilisation servo was set to below optimum for this spectrum. The lower gain reduced the suppression of the dye jet frequency fluctuations, seen in Fig 3.7 as a broad peak around 45 kHz.

In the 0 - 400 Hz range there is a striking difference between the two error signals, as is evident in Fig 3.8 Fig 3.8a shows the error signal from the laser stabiliser and Fig 3.8b is the spectrum of the signal from the sample. These spectra were recorded with the scan drive and the temperature controller connected. The error signal from the sample is dominated by a 50 Hz oscillation with a smaller oscillation at 73 Hz (less than one tenth the amplitude). In the case of the stabilisation control signal the oscillation at 50 Hz is smaller than the 73 Hz oscillation. This discrepancy is removed when the supercavity is completely disconnected from its control box, as demonstrated in Fig 3.8c. The 73 Hz oscillation was attributed to an oscillation in the cooling water to the argon ion pump laser and, hence is unaffected by disconnecting electronic circuits. The oscillations at 50 Hz and harmonics of 50 Hz are attributed to mains pickup within the reference cavity and are almost totally eliminated by disconnecting the electronics. The remaining 50 Hz signal implies that a residual mains pick up somewhere in the system but it is now only a minor contributor to the linewidth.

Fig 3.9 shows the spectrum of the error signal from the sample over 0 to 12.8 kHz. This spectrum was also recorded with the scan drive and temperature servo disconnected. The peaks at 950 and 1900 Hz, which were not visible in the laser stabilisation error signal, are almost certainly associated with mechanical resonances in the reference cavity. As it has been proposed to replace the reference cavity, in the long run, no attempt was made to locate or eliminate these resonances.

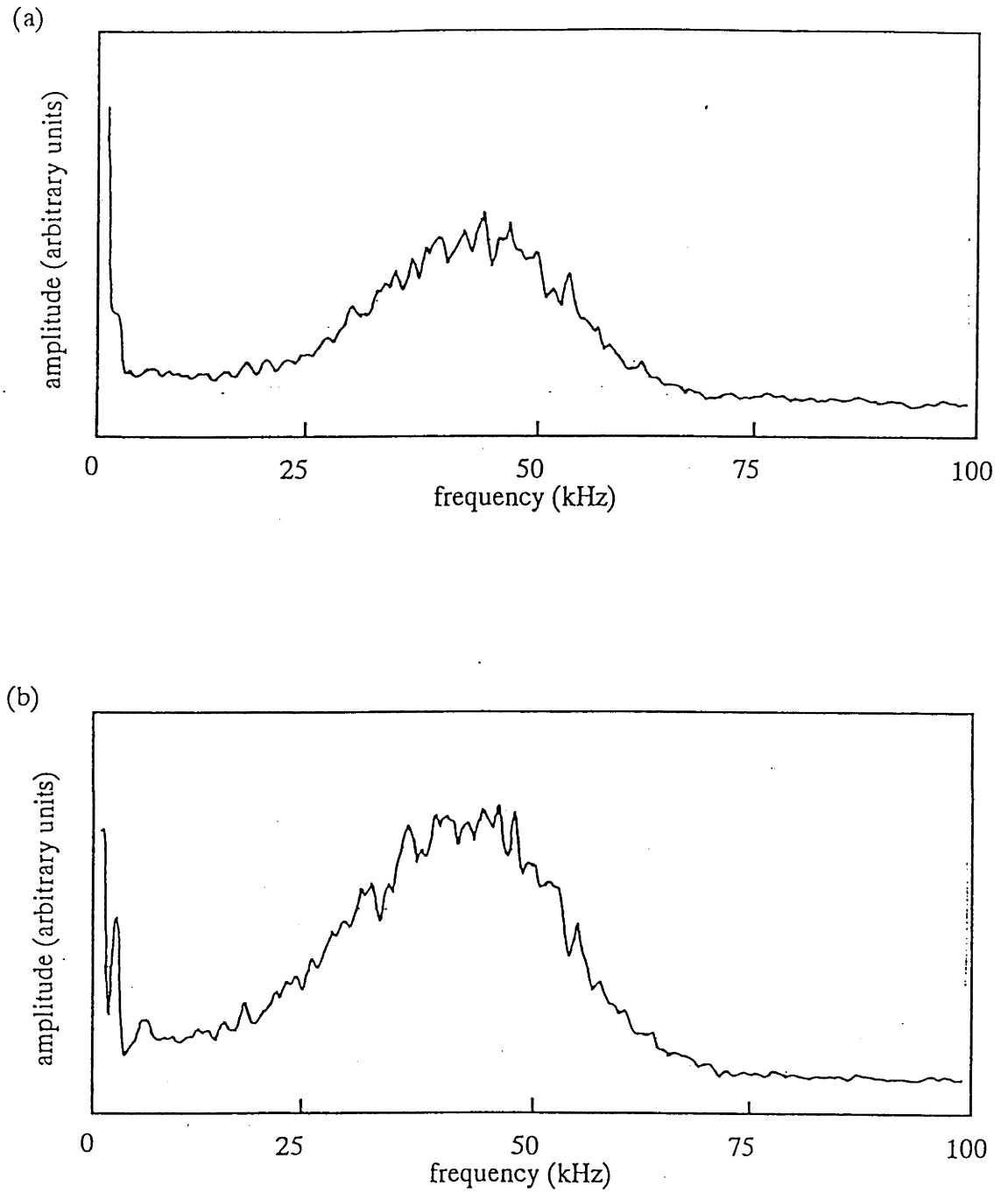

Figure 3.7. (a) Frequency response of the error signal generated from the transmission of the $Y_2O_3:Eu^{3+}$ sample, over the frequency range 0 - 100 kHz. (b) Frequency response of the error signal from the reference cavity, over the same range.

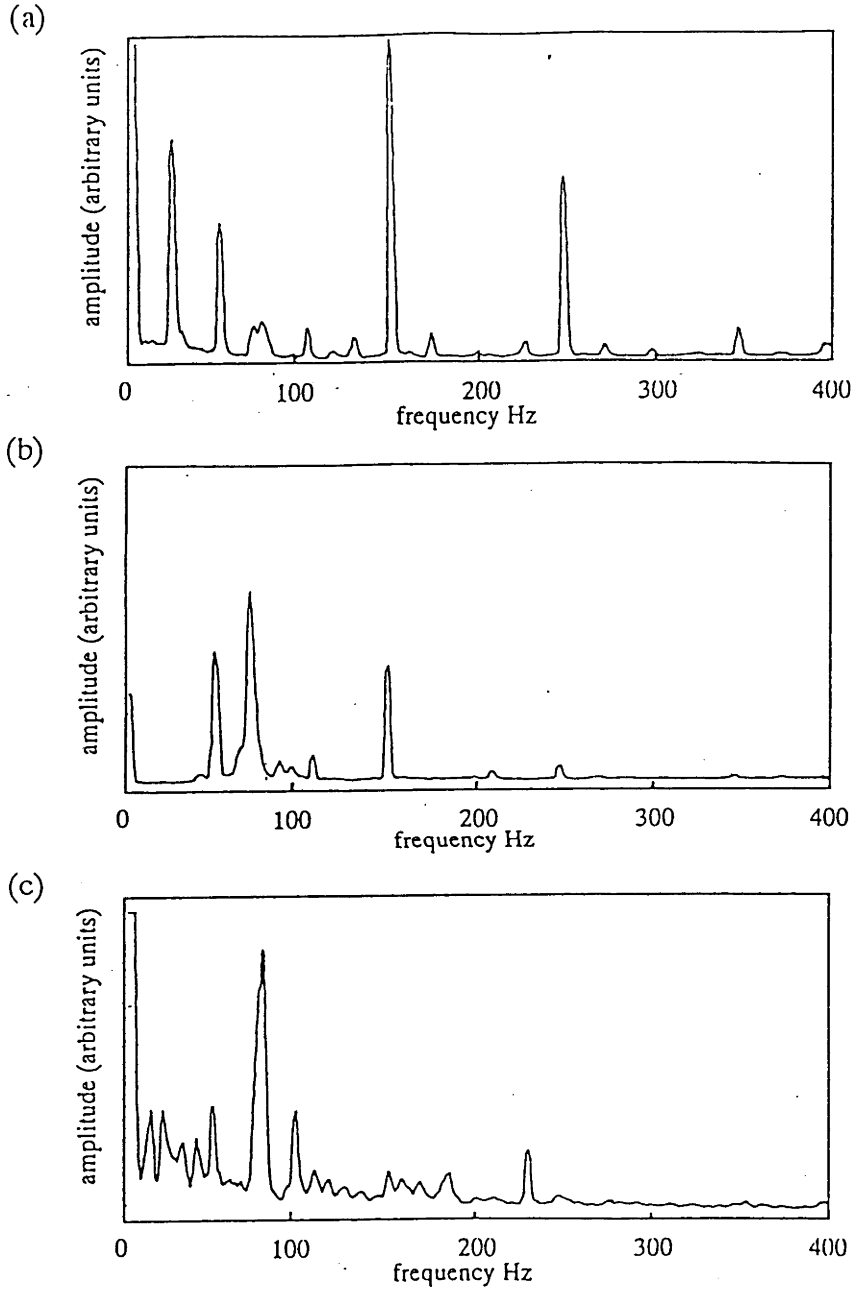

Figure 3.8 (a) Frequency response of the error signal generated from the transmission of the $Y_2O_3:Eu^{3+}$ sample, over the frequency range 0 - 400 Hz. (b) Frequency response of the error signal from the reference cavity over the same range. (c) frequency response of the error signal from the transmission of the sample after a source of an electrical pickup was eliminated.

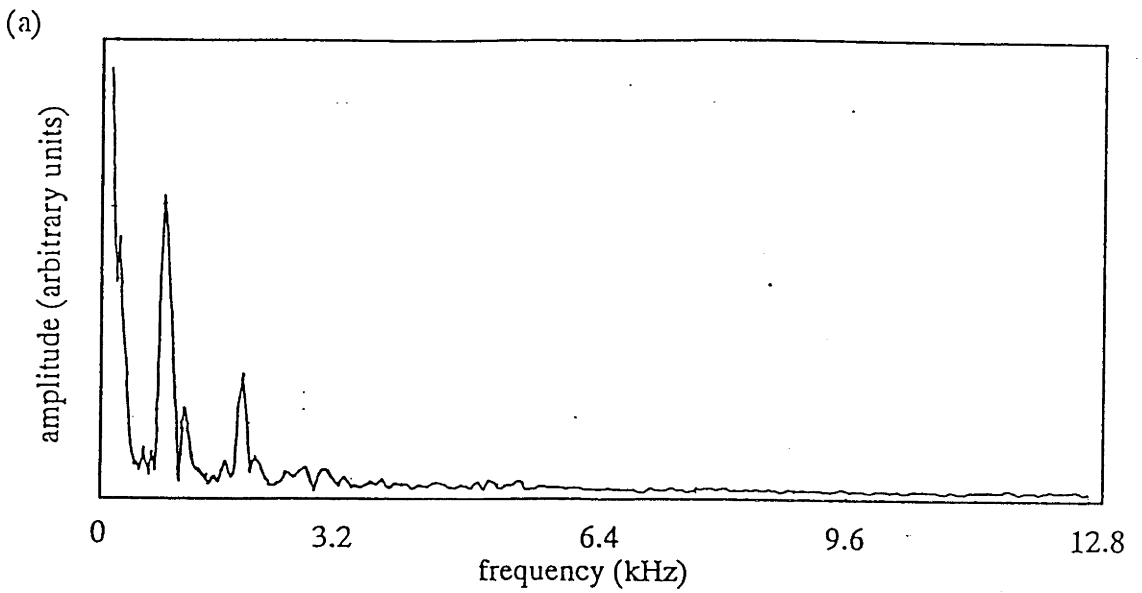

Figure 3.9 (a) Frequency response of the error signal generated from the transmission of the $Y_2O_3:Eu^{3+}$ sample, over the frequency range 0 - 12.8 kHz.

Further minor differences between the error signal generated from the spectral hole and that from the reference cavity exist and these could be used to give additional information about the laser. This will require additional work but could lead to some improvements to the laser stability in the future.

Preliminary experiments have been performed using the holeburning frequency discriminator to lock the reference cavity and, hence, the laser frequency to the hole [Manson *et al.* 1994]. The technique should be useful in improving the short to medium term stability of the laser frequency. In the long term the frequency of the hole is likely to drift as the laser probing the hole continues to burn it and, hence, "walk" the laser frequency. To establish whether this has been achieved here requires measurement with a second frequency reference such as another hole. This was beyond the scope of the present investigations and is not reported further. Ideally what is required is a transition which exhibits gated holeburning. One possibility is the $^7F_0 \Rightarrow {}^5D_0$ transition of an Eu^{3+} centre in an axially symmetric site. Normally such a transition does not exhibit persistent holeburning. This is because optical transitions between different hyperfine levels are now forbidden. By driving one of the hyperfine transitions in the optically excited state with an rf field, an optical pumping cycle which transfers ions out of one ground hyperfine level to another can effectively be turned on, resulting in holeburning (see Fig 3.10). If the rf is turned off the hole burnt during the preparation period will persist but no new holeburning will take place. For the optical pumping cycle to be efficient the Rabi frequency of the driven hyperfine transition has to be comparable to the relaxation rate from the $^5D_0$, of the order of kHz.

3.7 Discussion

In holeburning the transition linewidth enters in both the burning and reading process and so from a measured holewidth of 3.7 ± 1 kHz it is concluded that the maximum value of the transition linewidths is 1.9 ± 0.5 kHz. This value is smaller than the 2.5 kHz ($1/(\pi T_2)$) obtained from photon echo measurements made on the line centre of the inhomogeneous profile. However, both values are considered to be larger than the homogeneous linewidth. The photon echo measurements at line centre are considered to be broadened by what is termed spectral diffusion. The magnitude of the instantaneous spectral diffusion depends on the probability of the excitation of adjacent ions and in the holeburning measurements the rate is much smaller. For example, if it is assumed that there is no correlation between the frequency of the ions and their separation, then the probability of exciting adjacent ions will be proportional to the width of the spectral region of the inhomogeneous line excited. If we compare the case of burning a hole 5

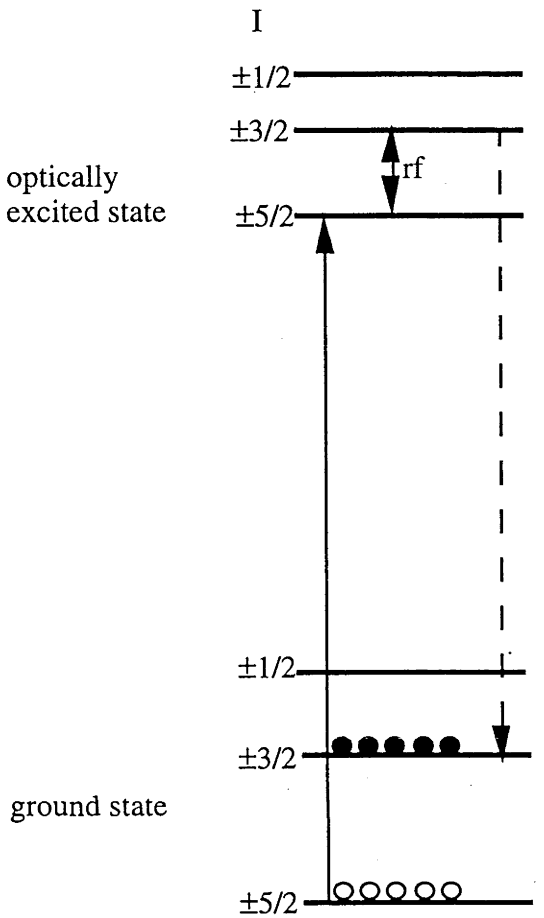

Figure 3.10 An example of an optical pumping cycle induced by driving a transition between hyperfine levels in the optically excited state. In an axial site where only $\Delta I=0$ optical transitions are allowed the rf driving field can be used to gate the holeburning process.

kHz wide, 100% deep with a photon echo measurement using a laser with a linewidth of 1 MHz, $\pi/2$ pulses of 1 μs a crude estimate tells us that 1 MHz/ 5 kHz = 200 times less ions are excited in the holeburning measurement. It is concluded that the spectral diffusion is not a contributing factor to the holeburning linewidth.

Echo measurements avoiding spectral diffusion by working in the wings of the line suggest that the homogeneous linewidth is at most 625 Hz. However, the magnetic field fluctuations and lifetime contributions to the homogeneous linewith have been estimated to be less than 300 Hz [MacFarlane *et al.* 1981]. If this was the homogeneous linewidth then the larger amount of the hole linewidth would arise from laser jitter. As the laser linewidth contributes to both the burning and the probing of the hole the laser linewidth must be less than 2 kHz over time scales of the order of 10 ms. If, however, the non-line centre echo measurement gives the true homogeneous linewidth then the conclusion would be that the laser jitter is smaller and closer to 1 kHz in the time scale of the holeburning.

The holeburning spectra showing double peaks demonstrates another characteristic of the laser; it occasionally makes frequency jumps of up to 5 kHz. As similar jumps are not observed in the error signal used in stabilising the laser it appears that these jumps are associated with the reference cavity.

In all of this section it is implied that the spectral hole serves as a completely stable frequency reference. Clearly, however, there are physical effects that can lead to the shift of the frequency of a hole. The frequency of the transition is sensitive to both the electric (crystal field) and magnetic fields in its environment. The crystal field depends on both the pressure on the crystal and the temperature so we can expect the hole frequency to shift with changes in either of these two parameters. Local changes in the crystal field due to the relaxation of strain field are also possible [Sellars *et al.* 94]. These may cause a drift in the centre frequency of the hole. Such drifts should be easy to diagnose as the local changes will tend to be random from site to site so their dominant effect on the hole will be to broaden it. Any drift in the hole centre frequency is likely to be seen as a distortion of the hole's symmetry as it broadens.

The sensitivity of the transition frequency to magnetic fields is, for moderate field levels, dominated by the enhanced nuclear magnetic moments associated with the ground and excited states of the Eu^{3+} ion, which are of the order of a few kHz/G. It is relatively straightforward to stabilise the external magnetic field to the mG level, so that the resulting frequency fluctuations will only be of the order of Hz. As discussed in Section

3.3 the local fluctuation in the magnetic field is likely to be of the order of hundreds of hertz. As with the local variations in the local crystal field, the local fluctuations in the magnetic
field will be random and will tend to broaden the hole rather than resulting in a significant drift in the hole frequency.

Further work is required to determine the long term stability of the hole frequency, which will have significance not only for the use of spectral holes as a frequency reference but also for the optical data storage applications of rare earth doped crystals.

3.8 Conclusion

Ultra-narrow optical holeburning has been demonstrated in $Y_2O_3:Eu^{3+}$, a system with very narrow homogeneous linewidths. A hole linewidth of 3.7 ± 0.5 kHz was observed. The claimed homogeneous linewidth is 625 Hz and from this linewidth a holewidth of 1.26 kHz could be anticipated using a laser with no jitter. From the observed linewidth, therefore, the laser linewidth was estimated to be less than 2 kHz on a 10 ms time scale. Thus the holeburning has been used to characterise the laser stability.

Although for these very narrow lines the laser jitter adds to the observed hole linewidth, at higher temperature, where the homogeneous linewidths are larger, the laser jitter makes a negligible contribution Hence, for the higher temperature measurements above 8 K we have shown that there is a strong correspondence between the linewidths determined by holeburning and the data from earlier photon echo measurements.

The generation of a frequency discriminator produced by transmitting FM modulated light through a holeburning medium has been demonstrated. This signal has been used to diagnose various instabilities in the stabilised laser described in Chapter 2 and with the information, the stability was further improved. Frequency drifts over a longer term are still known to be present and to eliminate such drifts a technique of locking to the hole has at least been demonstrated to be feasible.

I conclude that very narrow holeburning has been demonstrated, it has also been shown that holeburning provides a convenient reliable frequency reference technique.

Chapter 4 Coherence phase locking

4.1. Introduction

When a monochromatic field interacts with the electronic transition associated with an ensemble of identical atoms, the transition dipole moments will be driven in-phase with each other. After a period the oscillations of the moments get out of phase. The rate at which the moments dephase depends on various relaxation processes. The rate can be determined by measuring the response of the system to a change of amplitude or phase of the driving field. This response is known as a coherent transient and there are a variety of such responses commonly employed to obtain an understanding of the phenomenon associated with a driven transition.

For certain coherent transients it is necessary to have a laser stability better than the homogeneous linewidth of the transition and hence for the study of rare earth transitions, a laser such as the one described in Chapter 2 is essential. Such a laser enables coherent transients to be studied where the optical excitation has to be constantly in resonance with the transition. Moreover, because of this capability I show it is possible to introduce a new coherent transient effect in the visible, termed coherent phase locking (CPL). The technique parallels that of spin locking in the rf regime, which has long been used to study dephasing in NMR transitions [Solomon 59]. The equivalent technique has previously not been applied in the visible regime. A CW driving field is applied, and after a time corresponding to a $\pi/2$ pulse the phase is shifted by 90°. When the frequency of the driving field is on resonance with the transition, the consequence of the sequence is to lock the phase of the dipole moment of the atom in-phase with the driving field and the system is then transparent to the driving field. In this new coherent transient measurement the relaxation of the coherence of the system can be observed using phase sensitive detection while the system is driven. CPL can therefore be used to study the influence of the driving field itself on the relaxation associated with the transition.

The semi-classical, phenomenologically damped optical Bloch equations (OBE's) are routinely used to describe the response of a two level atom to a coherent optical driving field and in this presentation will be used to obtain an insight into the underlying physics. In the OBE's the response of an ensemble of identical atoms is described by the three dimensional Bloch vector [Allen and Eberly 75]. The three components of this vector comprise the component of the ensemble dipole moment in-phase with the driving field, the in-quadrature component of the dipole moment, and the population inversion of the ensemble. The OBE's assume that the relaxation of these quantities can be modelled by

two time constants, T_1 and T_2. T_1 is the decay time of the population inversion and T_2 is the decay time of the coherence of the ensemble's dipole moment. Both T_1 and T_2 are assumed to be independent of the driving field.

The OBE's are identical in form to the Bloch equations for NMR. The distinction between the instances is that for the NMR case, the Bloch vector represents the net magnetisation of the ensemble, driven by an rf field. It has long been recognised that for NMR measurements in solids, where the coherence relaxation rate is dominated by spin-spin coupling, the Bloch equations do not always adequately describe the atom field interaction. In particular the coherence relaxation rate has been found by Redfield to depend on the intensity of the driving field [Redfield 1955]. To model this behaviour Redfield introduced a modification to the Bloch equations, where for weak driving fields the component of the magnetisation aligned along the rf driving field still decays with the time constant T_2. For intense fields it decays with a longer time constant, which can be of the order T_1. The explanation given by Redfield for the modification was that the decay of the component of the magnetisation aligned along the rf field is (for driving fields above saturation) partially forbidden by entropy and energy considerations.

It was not until 1983 that it was demonstrated that the responses of optical transitions could also deviate from the OBE. In particular, experiments of DeVoe and Brewer [1983] showed that the intensity dependence of the third order free induction decay of the $^3H_4 \Rightarrow {}^1D_2$ optical transition of Pr^{3+} doped in LaF_3 deviates from the predictions of the OBE's. They found that their observations were consistent with the Redfield modifications to the OBE's, where the decay time T_2 for the component of the dipole moment in-quadrature with the driving field is replaced by a longer time constant approaching T_1 for intense fields. Not surprisingly it was suggested that the explanation may follow the same lines as Redfield's explanation for the NMR case [DeVoe and Brewer 1983].

A further aspect treated by DeVoe *a*nd Brewer, which has received much attention, is that the phase fluctuations due to interactions between the Pr^{3+} ion and the neighbouring F nuclei were averaged out at high Rabi frequencies. This averaging occurs when the period of the Rabi oscillation is comparable to the correlation time of the phase fluctuations perturbing the transitions. Considerations of this point led to a number of different models being proposed to explain DeVoe and Brewer's results [DeVoe and Brewer 1983, Schenzle *et al.* 1984, Szabo et al. 1989, Shakhmuratov *et al.* 1993]. The major differences between the various models can be attributed to the different statistics assumed for the frequency perturbations due to the F spin flips. The two most widely

studied models, probably because of their simplicity, are the Gaussian-Markov (GM) and random telegraph (RT) models. Reasonable fits to the FID results of DeVoe and Brewer have been obtained by applying these models with an appropriate choice of parameters, including the correlation time of the frequency fluctuations. A concern with these models is that (for reasonable parameters) they predict that the FID and photon echo measurements should show a non-exponential decay, contrary to observations [Berman 1986] Thus the most appropriate modification to the OBE is not firmly established.

Szabo and Muramoto subsequently demonstrated similar non-OBE behaviour for FID measurements in the $^4A_2(-1/2) \Rightarrow E(-1/2)$ transition in $Cr^{3+}:Al_2O_3$ [Szabo and Muramoto 1989]. They also measured the dephasing rate of the transition using the phase switching technique of rotary echoes (RE) [Muramoto and Szabo 1988]. Contradicting the models developed to describe the Pr^{3+} results, the dephasing rate as measured using RE was found to be independent of the laser intensity and was satisfactorily explained by the OBE. It has since been shown by Kilin and Nizovtev [1990], using a stochastic model of relaxing quantum systems, that the peculiarities observed in the experiments in ruby can be explained on the basis that $Cr^{3+}:Al_2O_3$ is a system with slow and yet strong modulation of the transition frequency . Kilin and Nizovtev do not clearly state why the relaxation of the coherence should depend so differently on intensity in the FID and RE techniques.

I will show in Section 4.2 that one significant difference between FID and RE measurements is the relative phase of the dipole moment and the driving field. For the case of FID the driving field is in-phase with the dipole moment whilst for RE it is in-quadrature. It is proposed in this chapter that the relative phase between the driving field and the dipole moment may be an important aspect in understanding non-OBE behaviour and should be considered when evaluating coherent transient techniques for study of such behaviour. In NMR a similar dependence on the relative phase of the driving field has long been recognised. For example, it should be noted that Redfield's modification of the Bloch equations does introduce an asymmetry between the relaxation of the in-phase and in-quadrature components.

For CPL, as for FID, the driving field is in-phase with the dipole moment and it may be expected that the coherence relaxation observed using CPL will depend on the driving field intensity in the same way as found for FID. A very significant advantage of CPL compared to FID measurements when studying an inhomogeneously broadened system, is that power broadening effects do not lead to a masking of changes to the coherence

relaxation rates. Consequently with increasing laser intensity the relaxation rates can be measured directly.

In this chapter the coherence relaxation of a single transition is studied using four separate coherent transients; CPL, RE, FID and photon echoes (PE). The results will be compared to the predictions of the OBE's.

The specific transition utilised is the $^7F_0 \Rightarrow {}^5D_0$ transition of the Eu^{3+} ion in $KEu(WO_4)_2$. This sample was chosen for its high absorption and high signal levels, a result of its high concentration of Eu^{3+}. The relaxation processes of the $^7F_0 \Rightarrow {}^5D_0$ transition of the Eu^{3+} ion in $KEu(WO_4)_2$ are currently poorly understood. It has been demonstrated that the dephasing rate as measured with photon echoes and FID's varies strongly across the inhomogeneous line profile, suggesting that the dephasing is dominated by interactions between the Eu^{3+} ions [Manson *et al.* 1990]. It is possible that a significant contribution to this dephasing results from what is termed instantaneous spectral diffusion. This occurs when the optical excitation of neighbouring ions perturbs the transition frequency of the active ion and hence generates dephasing. This dephasing mechanism adds an extra complicating factor. This weakens the impact of comparing any non-OBE behaviour of this transition with the various modifications to the Bloch model. For this reason no attempt will be made to model the system beyond comparing the observed coherent transient responses with the prediction of the unmodified OBE's.

4.2. Theory

In this Section the response of an inhomogeneously broadened transition to the CPL pulse sequence is investigated using the OBE's. The theory of FID, RE and PE will be reviewed and the relative phase of the driving field and the dipole moment of the atoms will be compared for free induction decay, rotary echoes and coherence phase locking.

4.2.1. Optical Bloch equations

According to the semi-classical theory of a two level atom interacting with a driving field the state of the atom can be described by the three quantities; w, the population inversion, u, the component of the transition dipole in-phase with the driving field E and v, the component of the transition dipole in-quadrature with the driving field. It is convenient to write these quantities in the form of a vector, known as the Bloch vector,

$$R = u\hat{1} + v\hat{2} + w\hat{3}. \qquad (4.1)$$

According to the optical Bloch equations, the evolution of the Bloch vector is given by,

$$\begin{aligned} \dot{u} + \Delta v + {}^{u}\!/_{T_2} &= 0, \\ \dot{v} - \Delta u - \chi w + {}^{v}\!/_{T_2} &= 0, \\ \dot{w} + \chi v + {}^{(w-w^0)}\!/_{T_1} &= 0, \end{aligned} \qquad (4.2)$$

where Δ is the detuning of the driving field from the atomic resonance and χ is the Rabi frequency. χ is given by the scalar product of the dipole moment and the amplitude of the driving field,

$$\chi = \mu \cdot E_0 / \mathrm{h}. \qquad (4.3)$$

where μ is the magnitude of the dipole moment. T_1 and T_2 have been given earlier as the population and dephasing relaxation times, respectively.

The observable quantity is the polarisation which is given by [Levenson 1988a]

$$P = \frac{N\mu}{2}(u - iv)e^{-i\omega t} + cc. \qquad (4.4)$$

When the optical transition has an inhomogeneous width Equation 4.4 must be integrated over the inhomogeneous broadening to give the total polarisation.

$$\langle P \rangle = \int_{-\infty}^{\infty} G(\omega_0) P(\omega_0) d\omega_o \qquad (4.5)$$

where $G(\omega_0)$ gives the spectral density of the atoms. In the context of this work, consistent with optical transitions in solids, it will be assumed that the width of the inhomogeneous line is much greater than the width of the homogeneous line and the Rabi frequency.

By defining a second vector, the pseudo field

$$\beta = \mathrm{Re}[\chi]\hat{1} + \mathrm{Im}[\chi]\hat{1} + \Delta\hat{3}. \qquad (4.6)$$

Equations 4.2 can be expressed in a form that leads to a geometrical interpretation of the evolution of the two level system,

$$dR/dt = \beta \times R + [relaxations \;\; terms]. \qquad (4.7)$$

If the relaxation terms are neglected Equation 4.7 indicates that the Bloch vector R precesses around the pseudo field B just as a spinning top precesses in a gravitational field.

To model the RE and CPL experiments it is necessary to solve the OBE's in the presence of a constant driving field, with the inclusion of the dephasing terms. In 1949, Torrey [Torrey 49] gave an analytic solution to the OBE's for a constant driving field, using Laplace transform techniques. His solution is reproduced in Appendix B and is made use of in Sections 4.2.3 and 4.2.4.

4.2.2. Optical detection

Before considering individual coherent transient techniques it is worth reviewing the detection of the optical signal. The generic experiment to be considered is illustrated schematically in Fig 4.1. A laser beam is modulated, either in amplitude, phase or frequency, and this beam is transmitted through a sample onto a detector. A second unmodulated beam may be used as a local oscillator to give phase sensitive detection. The total field incident on the detector is the sum of the transmitted laser field E_0, local oscillator E_{lo} and the signal field E_S.

$$\begin{aligned} \tilde{\tilde{E}}_T &= \tilde{\tilde{E}}_0 + \tilde{\tilde{E}}_{lo} + \tilde{\tilde{E}}_s \\ &= \tilde{E}_T e^{i(\omega t - kz)} + cc, \end{aligned} \qquad (4.8)$$

where the tilde denotes the slowly varying part of the field and

$$\tilde{E}_T = \tilde{E}_0 + \tilde{\tilde{E}}_{lo} + \tilde{E}_s \qquad (4.9)$$

The signal field

$$\tilde{\tilde{E}}_s(z,t) = \tilde{E}_s(z,t) e^{i(\omega t - kz)} \hat{e}_1 + cc \qquad (4.10)$$

obeys Maxwells equation

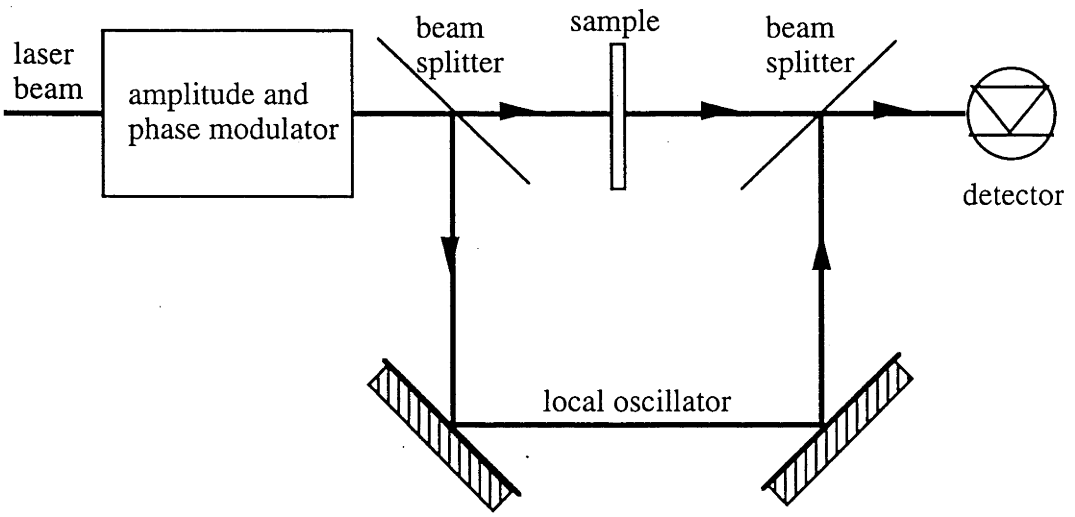

Figure 4.1. Schematic diagram of the generic coherent transient experiment.

$$\frac{\delta \tilde{E}_s}{\delta z} = -2\pi ik\langle \tilde{P} \rangle, \qquad (4.11)$$

where the angular brackets denote an average over the inhomogeneous line. For an optically thin sample, P does not depend on z explicitly. Substituting equation 4.5 into 4.11 and integrating over z gives

$$\tilde{E}_s = -2\pi kL\langle N\mu(u - iv) \rangle, \qquad (4.12)$$

where N is the number density of atoms across the inhomogeneous line and L is the sample thickness.

From the total light intensity $I = \tilde{\vec{E}}_T \bullet \tilde{\vec{E}}_T^*$, the observable transient signal for the case with E_{lo} or $E_0 >> E_S$ is given by

$$I_s = 2Re[\tilde{\vec{E}}_0 \bullet \tilde{\vec{E}}_s + \tilde{\vec{E}}_{lo} \bullet \tilde{\vec{E}}_s]. \qquad (4.13)$$

In the case where no local oscillator is used, such as in optical nutation and rotary echoes, the signal intensity is given by

$$I_s = 4\tilde{E}_0 \pi kLN\mu v, \qquad (4.14)$$

which is simply the absorptive signal. To observe u, the in-phase component of the dipole moment, it is necessary to use a local oscillator phase shifted from the transmitted beam. If the phase of E_{lo} is shifted by θ from that of E_0 the signal intensity is given by

$$I_s = 4(\tilde{E}_0 + \tilde{\vec{E}}_{lo} \sin\theta)\pi kLN\mu v + 4(\tilde{\vec{E}}_{lo} \cos\theta)\pi kLN\mu u \qquad (4.15)$$

It can be seen from Equation 4.15 that the use of a local oscillator allows the addition detection of the in-phase component of the dipole moment u.

Finally for FID and photon echo measurements either E_0 and E_S are both zero and $I_s = \tilde{\vec{E}}_s \bullet \tilde{\vec{E}}_s^*$ or alternatively heterodyne detection is used where E_0 is non-zero and is shifted in frequency by $\delta\upsilon$ from the frequency used to prepare the atoms and

$$I_s = 4\pi kLN\,\mathrm{Re}[E_0 e^{i\delta\nu t}\mu(v + iu)]. \qquad (4.16)$$

For FID and PE measurements, where the free evolution of the atoms is being observed, both components of the polarisation are monitored.

4.2.3. Coherence phase locking

The pulse sequence used for coherence phase locking consists of a $\pi/2$ pulse followed by a 90^{o} phase shift in the driving field. This pulse sequence is illustrated in Fig 4.2. The motion of the Bloch vector resulting from this pulse sequence can be calculated using Torrey's solution of the Bloch equations (see Appendix C). The evolution during the $\pi/2$ pulse is determined by setting the initial conditions $u_0=0$, $v_0=0$ and $w_0=-1$ in Equations C.4 and C.5. The values of u, v and w at the end of this pulse can be used as the initial conditions for the evolution of the Bloch vector after the 90^{o} phase shift, where $u_0=v(\pi/2)_-$, $v_0=-u(\pi/2)_-$, $w_0=w(\pi/2)_-$. Figs 4.3 a and b show the evolution of the Bloch vector for the on-resonance case ($\Delta=0$) and the off-resonance case ($D=0.1\ \chi$) respectively. For both these cases T_2 was chosen to be 55 μs, T_1 to be 500μs and, the Rabi frequency was set to 100 kHz.

The effect of the coherence phase locking pulse sequence is clearly seen in the on-resonance case. The $\pi/2$ pulse brings the Bloch vector up to the v-axis and the 90^{o} phase shift in the driving field then rotates the coordinate frame such that Bloch vector points along the 1-axis. In this state the atomic dipole moment is in-phase with the driving field and cannot coherently transfer energy with the driving field. The Bloch vector then relaxes back to a point near the origin. For the off-resonance case after the phase is switched the Bloch vector precesses about an axis in the 1-3 plane, maintaining a finite component along the 1-axis. As this component relaxes the Bloch vector spirals toward a point close to the origin. The sign of the component along the 1-axis is independent of the sign of the detuning, so the total polarisation can be expected to have a finite component in-quadrature with the driving field.

Figures 4.4a and b show the evolution of the in-phase and in-quadrature components of the total polarisation due to the CPL pulse sequence, calculated using Torrey's solution and numerically integrated over the laser detuning from -500 kHz to +500 kHz for the same parameters used in Figure 4.3. The long-lived decay is visible only in the in-quadrature component of the total polarisation, necessitating the use of phase sensitive detection. The long lived component of the CPL signal in Fig 4.4a decays exponentially with a decay time of 60 μs. Reducing the Rabi frequency by 50% was found to reduce the decay time to 58 μs, indicating only a slight intensity dependence. Both these decay times are slightly larger than the value 55 μs used for in the calculation T_2.

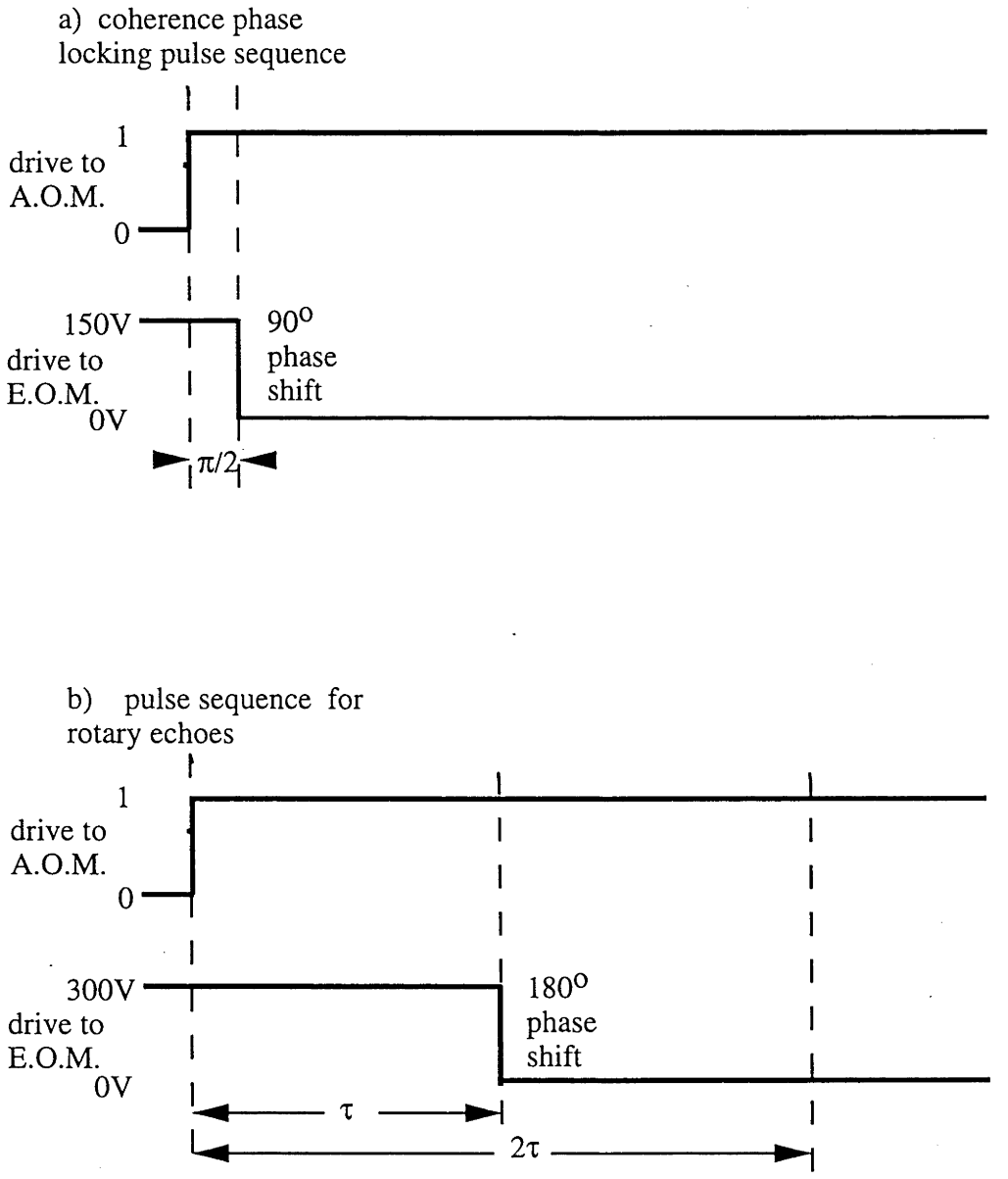

Figure 4.2. The pulse sequences used to generate the phase switching coherent transients for (a) coherence phase locking, for (b) and rotary echoes. Indicated in the figures are the drive levels to the acousto-optic modulator and electro-optic modulator, used to control the amplitude and phase of the optical driving field respectively.

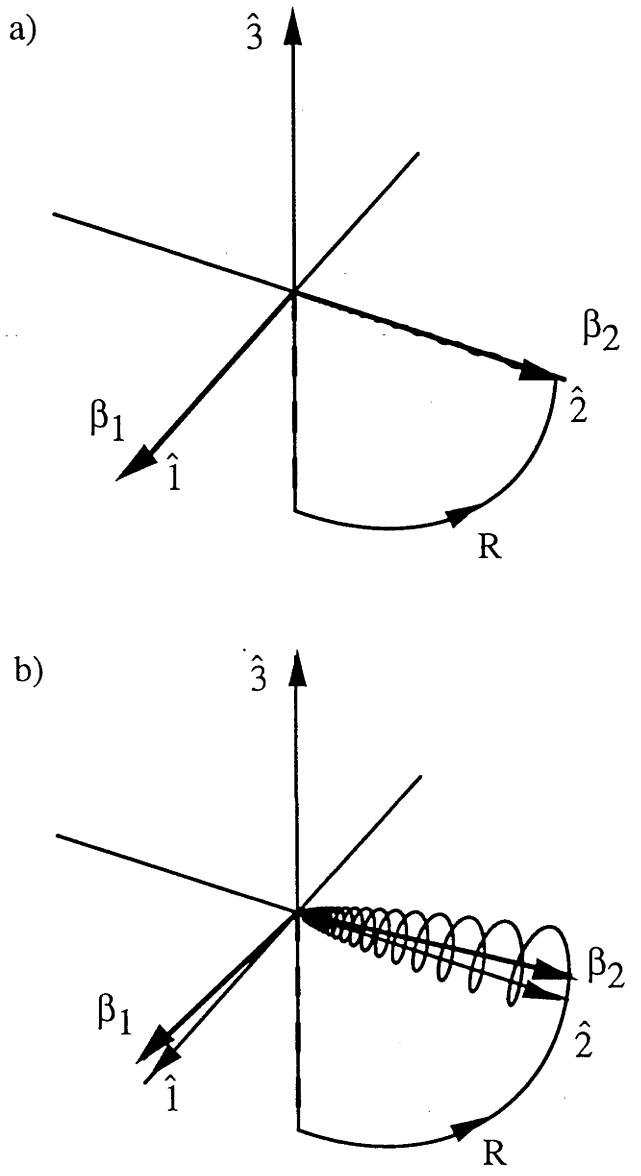

Figure 4.3. Evolution of the Bloch vector driven by a coherence phase locking pulse sequence, for both the on and off resonant cases, calculated using Torrey's solution. T_1 was set to 500 μs, T_2 to 55 μs and the Rabi frequency to 100 kHz. a) shows the on resonant case and b) the case for a 10 kHz detuning. β_1 and β_2 indicate the position of the generalised Rabi vector before and after the phase of the driving field is switched.

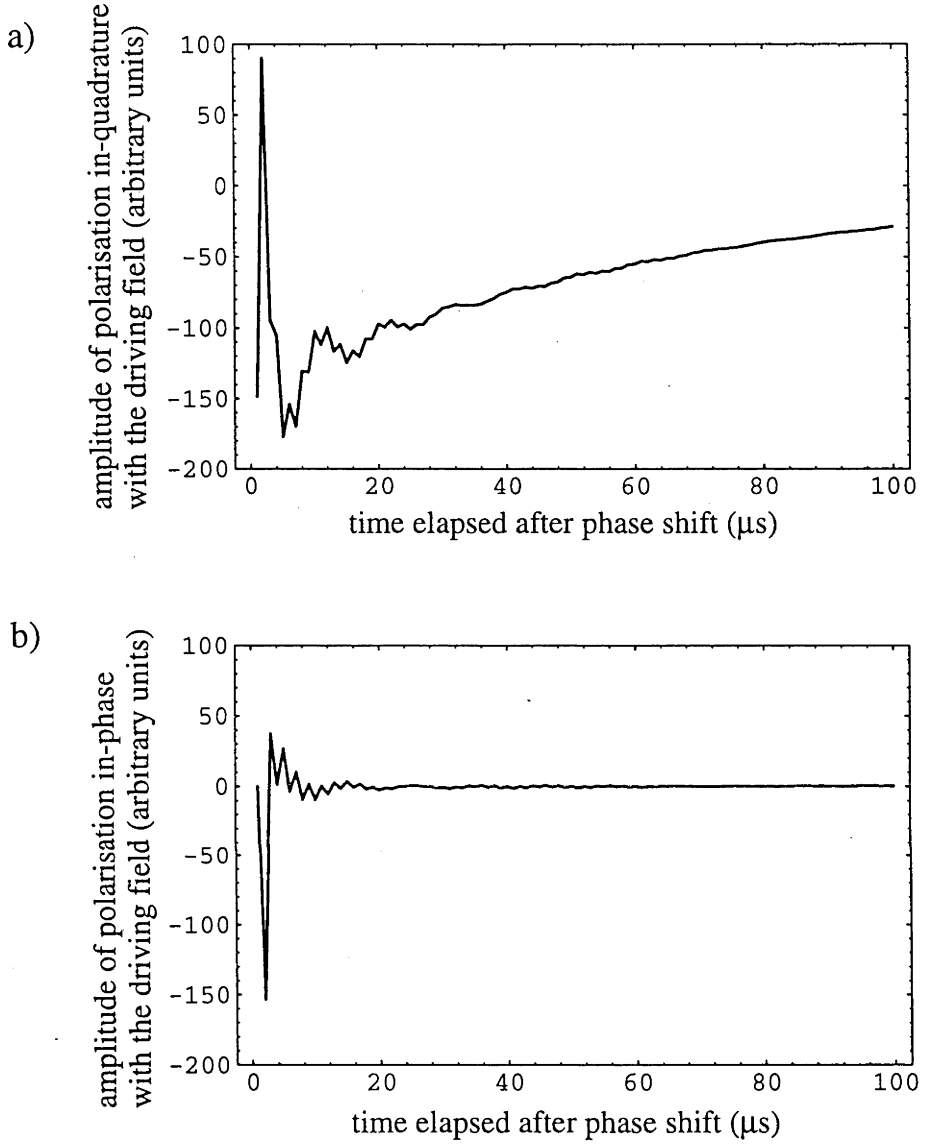

Figure 4.4 Evolution of the in quadrature and in phase components of the total polarisation due to the coherence phase locking pulse sequence acting on an inhomogeneously broadened line. The decay rates and Rabi frequency used are as for Fig 4.3.

The CPL signal is due to the component of the Bloch vector aligned along the 1-axis. The atoms closest to resonance with the driving field are the atoms with the largest component of their Bloch vector aligned along the 1-axis and will therefore make the largest contribution to the CPL signal. Clearly CPL provides information about the relaxation of the Bloch vector for atoms driven primarily by a field in-phase with their dipole moments.

4.2.4. Rotary photon echoes.

The pulse sequence used in rotary echoes is illustrated in Fig 4.2b. It consists of one pulse of length τ followed immediately by a second pulse phase shifted from the first by 180^o. The intensity of the driving field is chosen such that the Rabi period is significantly faster than the dephasing. The motion of the Bloch vector due to this pulse sequence can again be calculated using Torrey's solution. The evolution during the first pulse is determined by setting the initial conditions as $u_0=0$, $v_0=0$ and $w_0=-1$. The values of u, v and w at the end of this pulse can then be used as the initial conditions for the evolution of the Bloch vector after the 180^o phase shift, where $u_0=-u(\tau)_-$, $v_0=-v(\tau)_-$, $w_0=w(\tau)_-$. Figure 4.5a shows the evolution of the Bloch vector for the on resonance case. The effect of the 180^o phase shift is to reflect the pseudo field vector through the 2-3 plane, reversing the evolution of the Bloch vector, returning it to the 3-axis after a delay of τ from the phase shift. In the off resonance case shown in Fig 4.5b the reversal of the evolution is only partial, because the component of the pseudo field vector in the z direction is unchanged by the phase shift.

Rotary echoes are used to study the decay of optical nutations on inhomogeneously broadened lines. By at least partially reversing the evolution of the Bloch vector, the dipole moments of the inhomogeneously broadened ions can be rephased. Figs 4.6 a and b show the evolution of the total polarisation due to a rotary echo pulse sequence, calculated using Torrey's solution and numerically integrating over the laser detuning from -500 kHz to +500 kHz for the same parameters used in Fig 4.5. The initial nutation created by switching the laser on quickly decays, as the atoms at different detunings from the laser get out of phase with each other. The 180^o phase shift results in a partial rephasing of the atoms across the inhomogeneously broadened line, for times close to τ after the phase shift. This rephasing results in the reappearance of the nutation oscillations, seen as a modulation in the in-phase component of the total polarisation and hence in the transmitted laser intensity. The peak-to-peak amplitude of the echo nutations can be plotted as a function of the delay τ. The decay of the echo amplitude with increasing τ reflects the intrinsic relaxation of the coherence.

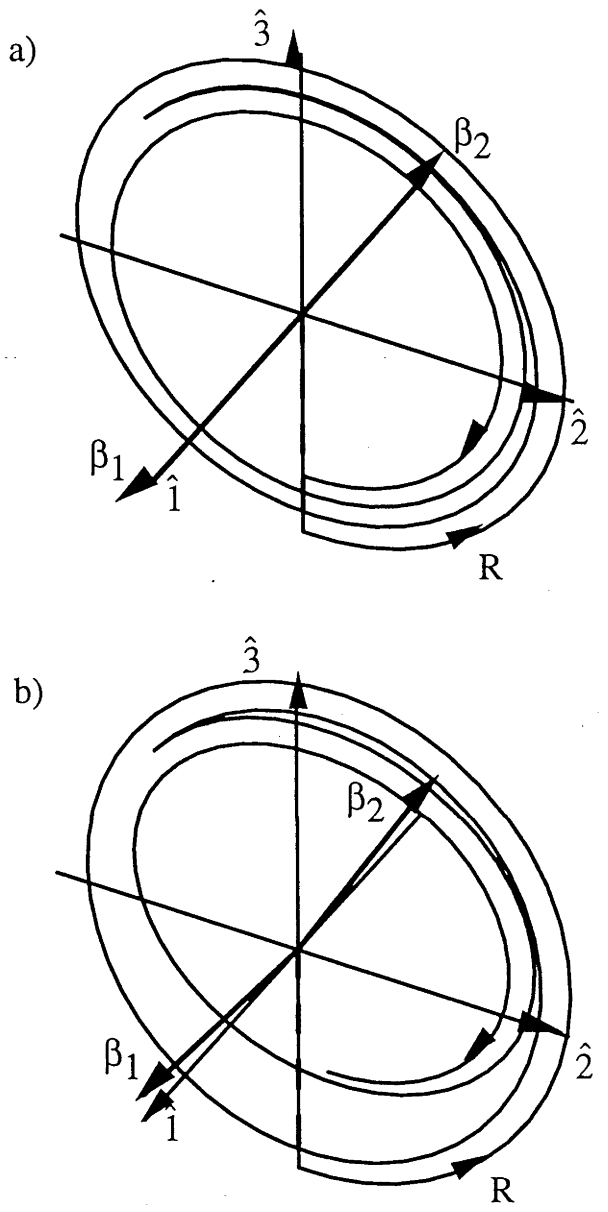

Figure 4.5. Evolution of the Bloch vector driven by a rotary photon echo pulse sequence, for both the on and off resonant cases, calculated using Torrey's solution. T_1 was set to 500 μs, T_2 to 55 μs and the Rabi frequency to 100 kHz. a) shows the on resonant case and b) the case for a 10 kHz detuning. β_1 and β_2 indicate the position of the generalised Rabi vector before and after the phase of the driving field is switched.

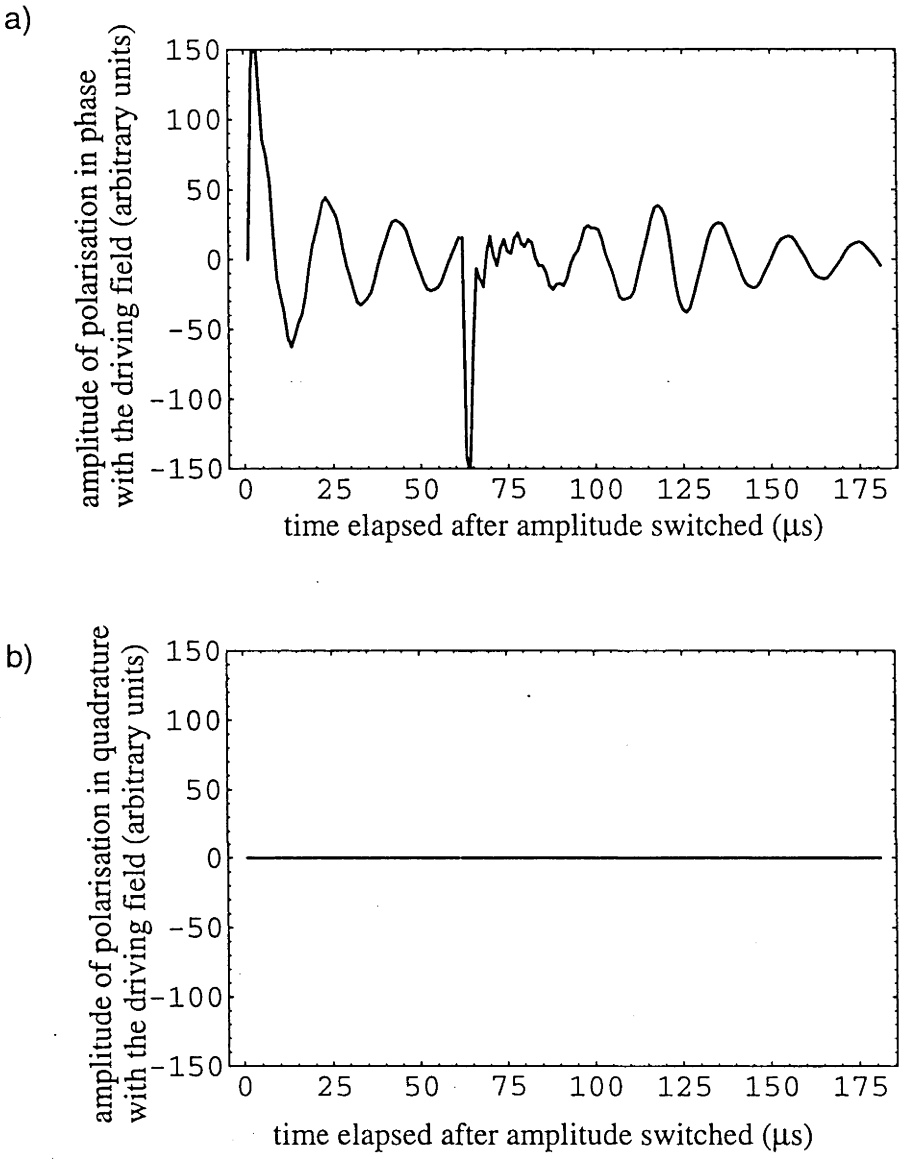

Figure 4.6 Evolution of the in phase and in quadrature components of the total polarisation due to the rotary echo pulse sequence acting on an inhomogeneously broadened line. The decay rates and Rabi frequency used, are as for Fig 4.5.

It is the atoms closest to resonance with the driving field which generate the dominant contribution to the rotary echo signal, since these atoms undergo the greatest rephasing. As the near-resonant atoms have the largest component of their dipole moments in-quadrature with the driving field, rotary echoes provides information about the relaxation of the Bloch vector for atoms driven primarily by a field in-quadrature with their dipole moments.

4.2.5. Free induction decay

Free induction decay coherent signals are generated by rapidly switching off of a driving field. The case we will consider here is the simplest, which previously derived elsewhere [Levenson 1988b], where the driving field is on long enough prior to being switched off for the system to reach a steady state. The steady state solution of the optical Bloch equations is,

$$
\begin{aligned}
u(\infty) &= \frac{-\Delta\chi}{\Delta^2 + T_2^{-2} + \chi^2 T_1/T_2} \\
v(\infty) &= \frac{-\chi}{\Delta^2 + T_2^{-2} + \chi^2 T_1/T_2} \\
w(\infty) &= \frac{-\chi^2 T_1/T_2}{\Delta^2 + T_2^{-2} + \chi^2 T_1/T_2}
\end{aligned}
\qquad (4.17)
$$

The components of the steady state Bloch vector are plotted as function of the laser detuning in Fig 4.8 for a saturating field with a Rabi frequency $\chi=10(1/T_2)$.

The FID signal is found by substituting the steady state solution given in equations 4.17 for the initial conditions of the free evolution solution of the Bloch equations,

$$
\begin{aligned}
u(t) &= \left[u_o \cos(\Delta t) - v_o \sin(\Delta t)\right] e^{-t/T_2}, \\
v(t) &= \left[v_o \cos(\Delta t) + u_o \sin(\Delta t)\right] e^{-t/T_2}, \\
w(t) &= -\left[1 - (w_0 + 1) e^{-t/T_1}\right].
\end{aligned}
\qquad (4.18)
$$

This is then substituted into Equation 4.4 and integrated over the inhomogeneous line to give the total polarisation,

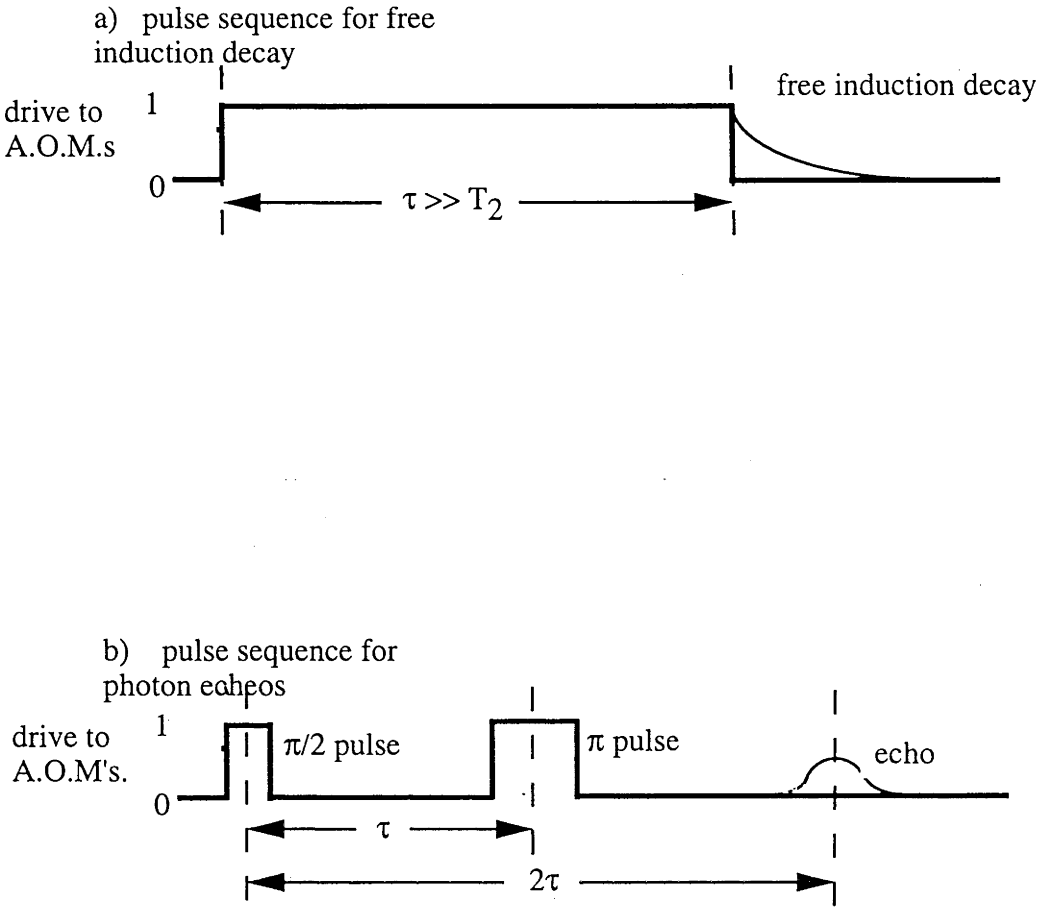

Figure 4.7. The pulse sequences used to generate the amplitude switching coherent transients free induction decay (a) and photon echoes (b). Indicated in the figures are the drive levels to the acousto-optic modulators used to switch the amplitude of the optical driving field.

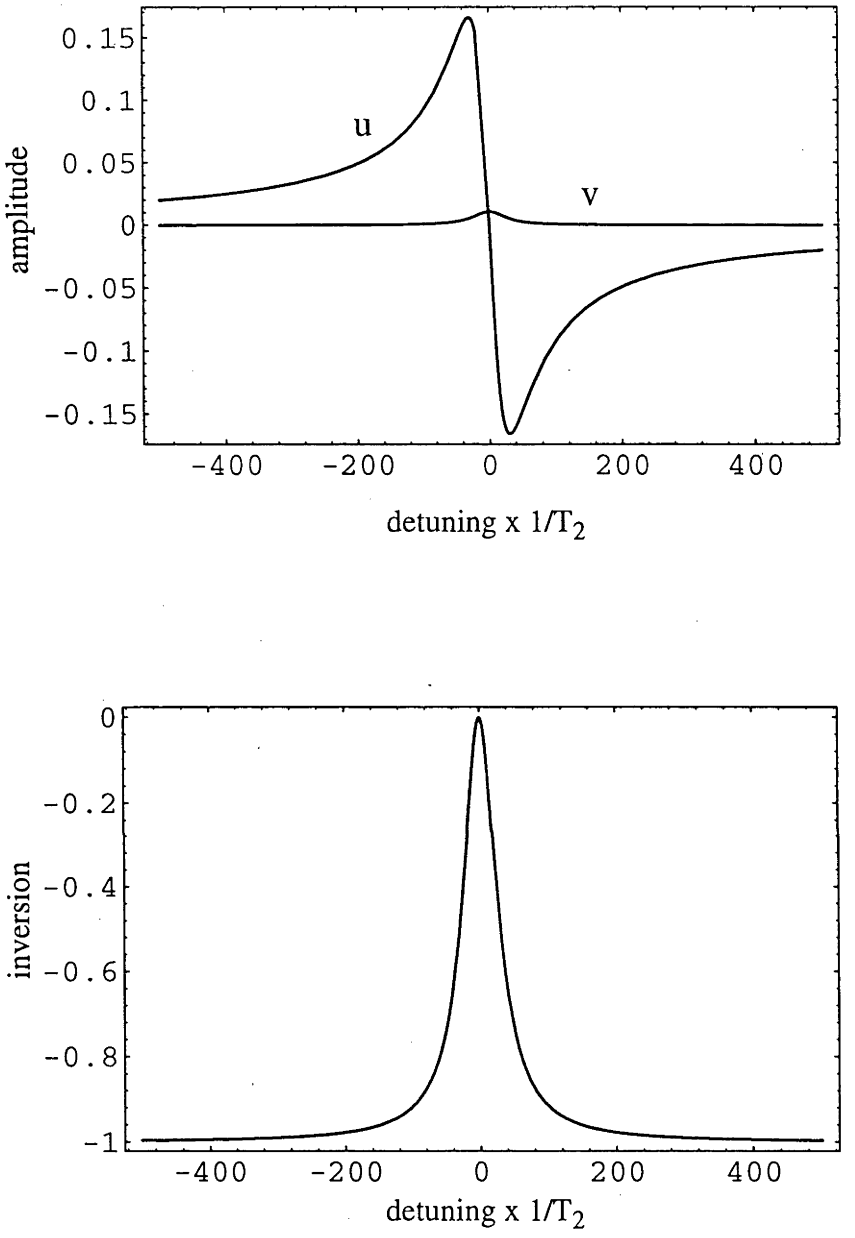

Figure 4.8. The components of the steady state Bloch vector as a function of the detuning of the driving field for a saturating field with a Rabi frequency of $\chi=10/T_2$ and $T_1=10T_2$.

$$\langle P\rangle = \mu\chi e^{-t/T_2}\int_{-\infty}^{\infty}\frac{-G(w_o)(\Delta+i/T_2)}{(\Delta^2+T_2^{-2})}e^{-iw_0t}dw_o$$
$$+\mu\chi^3 e^{-t/T_2}\int_{-\infty}^{\infty}\frac{-G(w_o)(\Delta+i/T_2)T_1/T_2}{(\Delta^2+T_2^{-2})((\Delta^2+T_2^{-2}+\chi^2T_1/T_2)}e^{-iw_0t}dw_o \qquad (4.19)$$

The first term in equation 4.19 is the linear FID polarisation which decays with a time constant of the order of the reciprocal of the inhomogeneous linewidth. The second term is the third-order FID polarisation. This nonlinear term is due to the saturation of the atoms whose transition frequencies are close to that of the driving field. Assuming $G(\omega_0)$ is so slowly varying that it can be considered constant and removed from the integral, the third-order total polarisation is given by,

$$\langle P\rangle^3 = \frac{\pi i G(\omega)\mu\chi^3 T_1 \exp\left[-(t/T_2)\left(1+\sqrt{\chi^2T_1T_2+1}\right)\right]}{T_2^{-1}+\chi^2T_1+\left(T_2^{-1}+\chi^2T_1/T_2\right)^{1/2}}\exp^{-i\omega t}. \qquad (4.20)$$

From equation (4.20) it is seen that the decay rate of the third-order FID amplitude is,

$$T_{obs}^{-1} = (1/T_2)\left(1+\sqrt{\chi^2T_1T_2+1}\right) \qquad (4.21)$$

In the weakly saturated regime the decay rate is $2/T_2$. Half of this decay rate represents inhomogeneous broadening due to the width of the hole burnt during the preparation stage, and half represents the intrinsic transverse relax rate of the ensemble of saturated atoms. As the amplitude of the driving field is increased the rate of the decay of the third-order FID decay increases. This is because of the increased power broadening of the hole burnt in the preparation stage. The non-OBE behaviour results in a reduced level of power broadening in the preparatory stage, and hence a slower decay of the FID signal, than is predicted by the OBE's. DeVoe *et al.* [1983] and Szabo *et al.* [1989] both observed for a saturating field that

$$T_{obs}^{-1} = 1/T_2(1+\chi T_1). \qquad (4.22)$$

It can be seen in Fig 4.8 that the ions on resonance have their dipole moments in-quadrature with the driving field. Nevertheless these ions contribute little to the third order FID. In fact it is the saturation of the ions on or close to resonance and the absence of their emission that is responsible for the third order FID. It is the ions off-resonance

which make the major contribution to the signal. These ions have their dipole moments predominantly in-phase with the driving field.

4.2.6 Photon echoes

The PE pulse sequence is shown in Fig 4.7 The sequence starts with a hard pulse of ideally an area of $\pi/2$. During a period τ the individual Bloch vectors undergo free evolution and get out of phase with each other at a rate characterised by their detuning. After this period a second pulse is applied. The length of the second pulse is twice that of the first pulse, ie a π pulse. The second pulse has the effect of rotating the Bloch vectors through an angle of 180° around the 1-axis. This reverses the phase of the Bloch vectors. The Bloch vectors are then allowed to evolve freely again. During this period the Bloch vectors rephase with each other. At a time τ after the second pulse the Bloch vectors realign and an echo signal is produce. It has been shown that the amplitude of the polarisation at 2τ varies as [Kurnit *et al.* 1964]

$$|P(2\tau)| \propto e^{-2\tau/T_2} \qquad (4.23)$$

The decay of the photon echo with increasing delay time τ gives a measurement of the relaxation of the coherence decay in the absence of the driving field.

4.3 Experimental apparatus and techniques

The experimental arrangement used for both the coherence phase locking and rotary echo measurements is shown in Fig 4.9. The modified Coherent 699 dye laser, described in chapter 2, was tuned to the $^7F_0 \Rightarrow {}^5D_0$ Eu^{3+} transition at 582 nm. The laser typically generated 500 mW at this wavelength with a roughly Gaussian beam profile. The laser linewidth was estimated from the error signal to be of the order of 1 kHz on the time scale of milliseconds (see Chapter 2 and 3).

The $KEu(WO_4)_2$ sample was 0.8 mm thick with 100 % absorption within 2 GHz of line centre. The laser was tuned to the low frequency side of line centre by 14 GHz where the absorption was 20%. By operating away from line centre the dephasing due to instantaneous spectral diffusion should be reduced, by reducing the number of ions excited by the laser. The crystal was orientated with the laser beam passing approximately down the C axis, so that it absorbed linearly polarised light. The sample was cooled to below 2.0 K by immersing it in liquid helium pumped to below its lambda point.

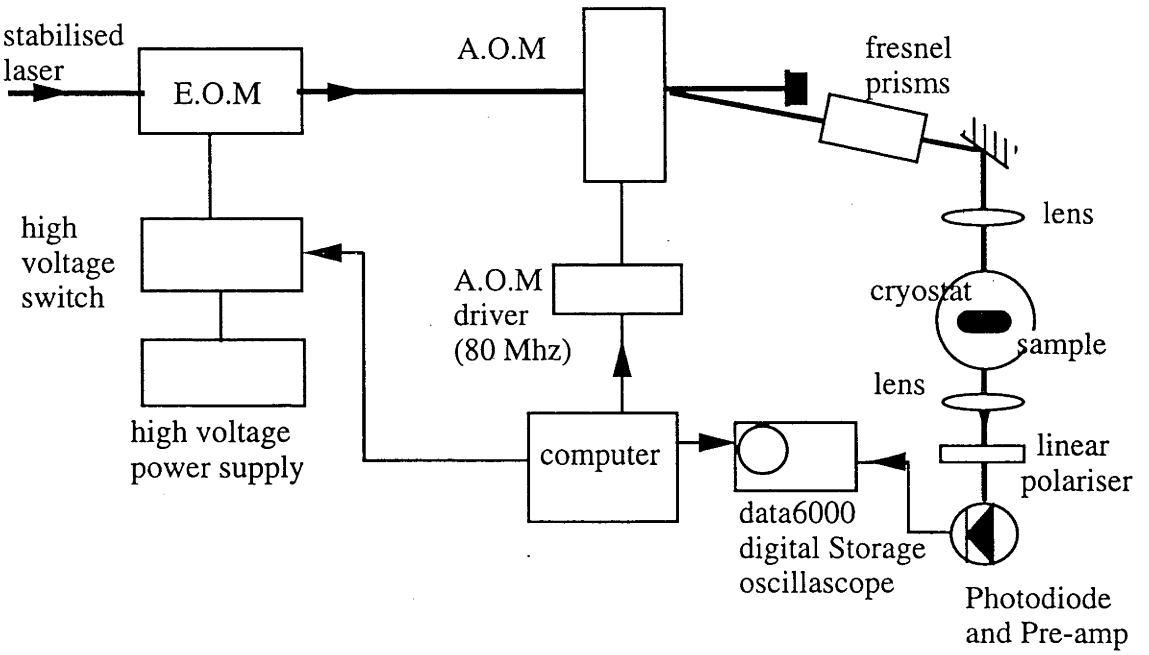

Figure 4.9. Schematic diagram of experimental setup for phase switching measurements. A.O.M., acousto-optic modulator; E.O.M., electro-optic modulator.

The phase of the light was switched using a 1039D Pulse Technology electro-optical phase modulator, a high voltage power supply and a high voltage switch. The phase modulator had a halfwave voltage of 290 V at 582 nm. It was found to have negligible amplitude modulation and a flat drive frequency response from DC to 500 MHz. The switch consisted of a high voltage FET that pulled the drive input of the phase modulator to ground when switched on. The modulator was charged by the high voltage supply via a 1000 ohm resistor limiting the current drawn by the FET. This arrangement was capable of pulling the drive input from 900 V to within a few volts from ground in 20 ns. The phase switching was tested by placing the E.O.M. in an arm of a Michelson interferometer and observing the phase shift in the laser by monitoring the output of the interferometer with a photodiode. The transient response of the E.O.M. was found to be completed within 200 ns.

An 80 MHz acoustic optical modulator (AOM) was used to gate the laser beam and control its intensity. The rise time (switching from off to on) was of the order of tens of ns. The first-order beam from the AOM was focused with a 20 cm lens and then transmitted through the sample. The maximum laser intensity that could be delivered to the sample was 150 mW. The polarisation of the beam could be rotated with a pair of Fresnel rhomb prisms, situated just before the lens. The transmitted beam was attenuated with neutral density filters, and a linear polariser was used to select the detected polarisation. The detector used was a New Focus photodiode and pre-amplifier with a flat modulation frequency response from DC to 125 MHz. A computer was used to control the high voltage switch and AOM drive, and triggered the digital storage oscilloscope. The delays between trigger pulses could be changed in 1 μs steps.

The phase sensitive detection for the coherence phase locking was obtained by using orthogonal polarisations for the reference and probe beams. The polarisation of the laser beam was rotated about 35 degrees away from that of the transition. The reference beam was the component of the laser beam's polarisation orthogonal to the polarisation of the transition. The phase of the reference beam was shifted relative to the probe by the birefringence of the sample. The polariser in front of the detector analysed the now ellipitically polarised light, effectively combining a component of the reference beam with a component of the probe beam. As an indication of the ellipticity of the transmitted light the maximum attenuation of the beam obtained by rotating the analysing polariser was 80%. For the phase locking measurement the polariser was rotated to give the maximum transient signal. For the rotary echo measurements the analysing polariser was removed.

For both the coherence phase locking and the rotary echoes the signals were averaged over 20 shots, using a repetition of 0.2 Hz.

The photon echo experiments were performed with the experimental setup illustrated in Fig 4.10 The beam from the stabilised laser was gated with two A.O.M.s in series. The A.O.M.s were arranged so that the up-shifted beam from the first A.O.M., driven at 80 MHz, was down-shifted by the second drive at 85 MHz. This probe beam was focused with a 20 cm lens, transmitted through the sample, a beam splitter and a ND filter onto the New Focus photodiode and preamplifier. Care was taken to use the same beam profile and position of the 20 cm lens used in the phase switching measurements. The diameter of the beam on the sample was 200 μm and the maximum available laser intensity, as measured after the 20 cm lens, was 180 mW. The unshifted beam from the first A.O.M. was mode-matched and combined with the probe beam on the beam splitter to provide a local oscillator for heterodyne detection. The signal from the preamplifier was fed to the input of a spectrum analyser. The analyser was tuned to 5 MHz and its bandwidth set to 300 kHz. The video output from the spectrum analyser was recorded on a digital storage oscilloscope. The spectrum analyser was set to measure voltage. The trace could then be stored on the PC. The computer was also used to trigger the A.O.M.s and the storage oscilloscope.

The amplitude of the photon echo signal was measured as a function of the delay between the $\pi/2$ and π pulses, for five different laser intensities; 8, 31, 125, 159 and 172 mW. The length of the "$\pi/2$" pulses at each intensity was selected to give the largest echo signal. For each time delay the signal was averaged over 10 shots.

The FID measurements were performed with an experimental setup optically identical to the one used to detect the photon echoes. For the FID measurements, though, the 5 MHz signal from the pre-amplifier was fed directly to the digital storage oscilloscope. It was necessary to do this to prevent limitation of the bandwidth of the signal. The 300 kHz bandwidth of the spectrum analyser would have made it impossible to distinguish the FID signal from the transients in the detector due to the switching off of the laser. As no provision was made to fix the phase of the heterodyne signal it was not possible to average the signal in real time as was done with the photon echoes.

FID signals were recorded for a number of different laser powers ranging from 0.05 mW to 120 mW. The preparatory pulse was 400 μs long. At each laser power 5 shots were recorded.

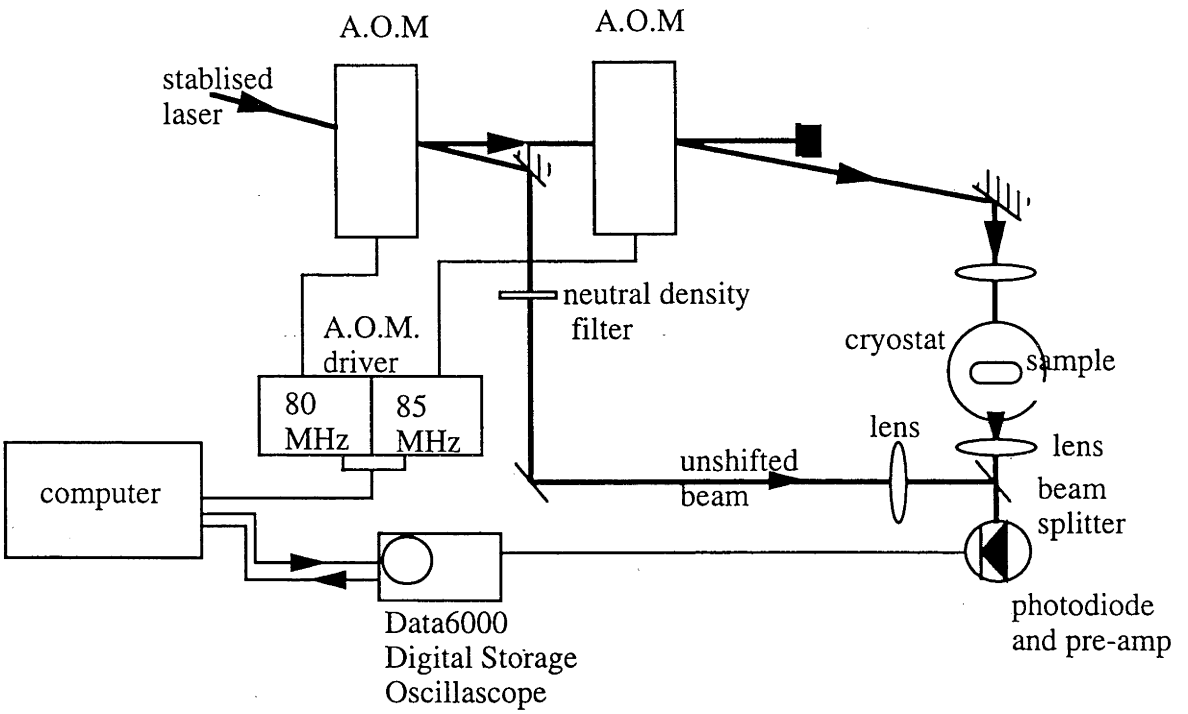

Figure 4.10. Schematic diagram of experimental setup for amplitude switching measurements. A.O.M., acousto-optic modulator; E.O.M., electro-optic modulator.

4.4. Results

The lifetime of the $^5D_0$ state, T_1, was determined by monitoring the decay of the fluorescence at 582 nm from the sample after exciting the $^7F_0 \Rightarrow {}^5D_0$ transition for 400 μs with 50 mW of laser power. The fluorescence was observed to decay exponentially with a decay time of 500 ± 50 μs.

To determine T_2 for the free evolution of the transition the decay rate of the photon echo decay rate was measured for the five different intensities. The lengths of the pulses were set to maximise the echo amplitude. The echo decay rate as a function of the laser intensity is shown in Fig 4.11. The echo decay rate clearly has an intensity dependence, indicating the presence of instantaneous spectral diffusion. Only a relatively weak intensity dependence is seen at low laser intensity, and increasing the laser intensity from 8 to 31 mW only resulted in a 10% increase in the decay rate. This suggests that the limiting value of T_2 (twice the observed decay rate) as the laser intensity approaches zero will be close to the value observed with a laser power of 8 mW, 55 μs.

Examples of rotary echo signals for a laser intensity of 170 mW are shown in Fig 4.12. The observed nutation frequency was 150 ±10 kHz. The decay of the nutation oscillations is more rapid than in the theoretical trace shown in Fig 4.6 because of the distribution of the laser intensity across the beam profile. By integrating Torrey's solution across the laser beam (assumed Gaussian) and the inhomogeneous line profile, a Rabi frequency at the centre of the laser beam of 2π(150 kHz), was found to give an echo nutation frequency of 150 kHz. This result was used to calibrate the relationship between the laser power and the Rabi frequency across the laser beam profile:

$$\text{peak Rabi}/2\pi = 150\sqrt{\frac{power}{172mW}}\ \text{(kHz)}$$

This calibration is for the laser intensity as measured before the laser beam entered the cryostat. No correction was made for the loss from passing through two glass windows.

A plot of the rotary echo amplitude vs the delay in switching the phase τ is shown in Fig 4.13 for the two laser intensities 170 mW and 35 mW. The amplitude was taken as the peak-to-peak nutational signal centred at 2τ. Also shown in this figure is the OBE prediction, obtained using Torrey's solution as described in Section 4.2 with T_1=500 μs and T_2=55 μs and χ=150 kHz. The observed decay times for the two laser intensities 170 mW and 35 mW were 14 ± 2 μs and 15 ± 2 μs respectively. Fig 4.13 shows that,

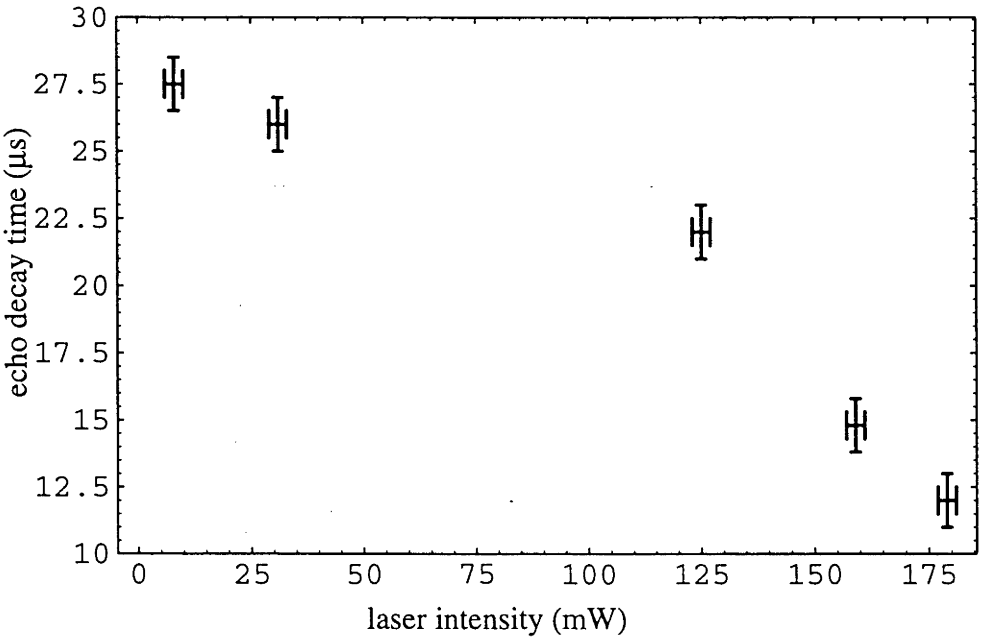

Figure 4.11. Observed decay time of the photon echo signal as a function of the laser intensity.

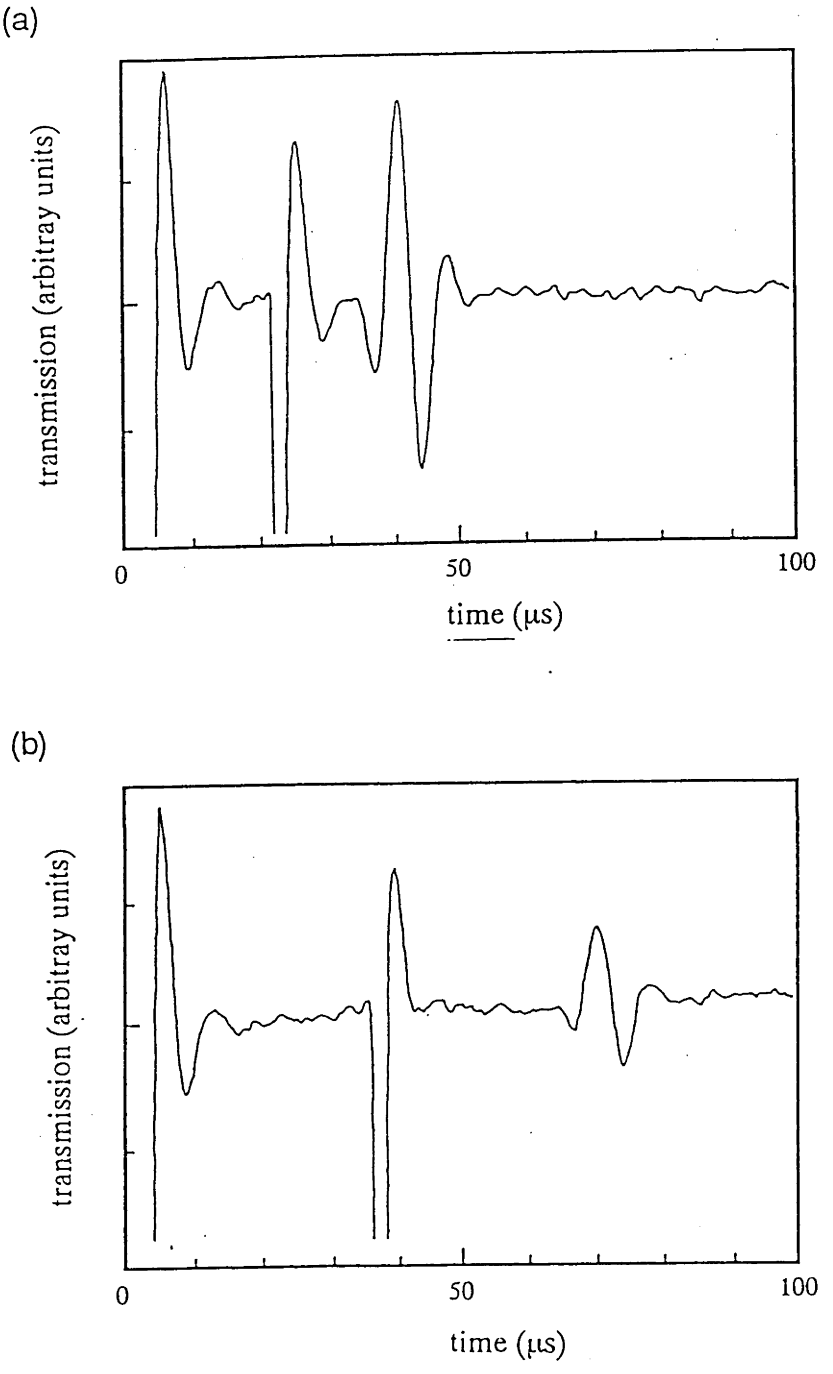

Figure 4.12. The transient response due to the rotary echo pulse sequence. The laser intensity was 170 mW. (a) Delay in switching the phase was 20 μs. (b) Delay in switching the phase was 35 μs.

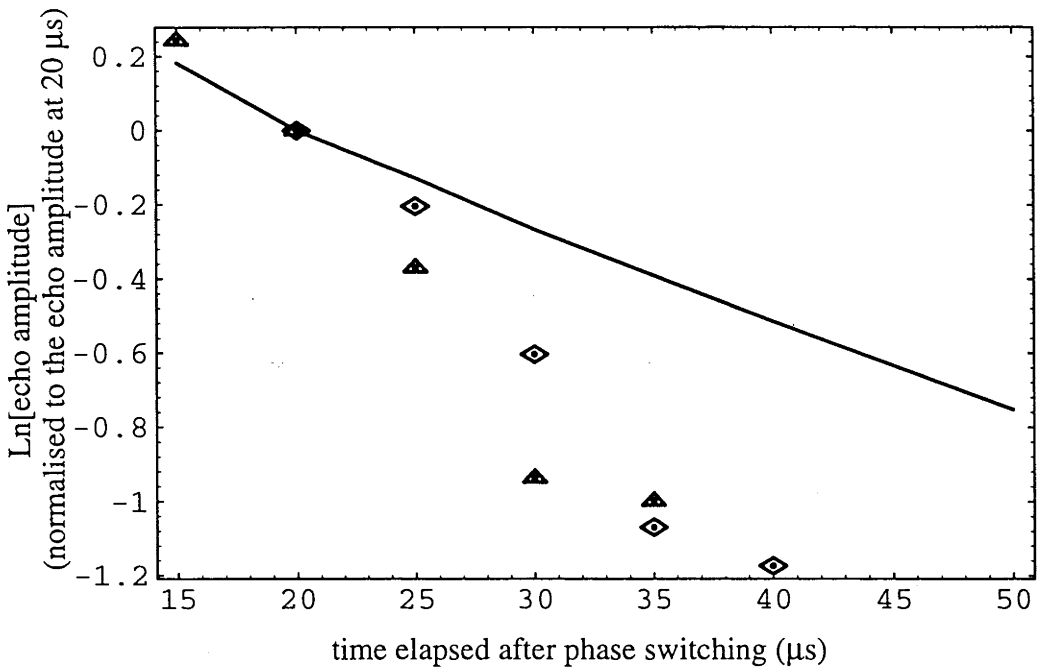

Figure 4.13. Experimental and theoretical rotary echo decay. The experimental points are for nutation frequencies of 120 kHz (Δ) and 65 kHz (◇). The solid line is the decay predicted by the OBE's.

for both laser intensities, the observed decay time was much less than the value predicted by the OBE's of 42 μs.

Fig 4.14 shows a FID signal for a laser intensity of 0.05 mW, the lowest intensity used. The decay time of the signal is 21.5 ± 1 μs. The predicted decay time is 18 μs, obtained by integrating equation 4.20 across the laser beam profile, using the relationship between the laser power and the Rabi frequency across the laser beam, determined above, and setting T_2=55 μs.

The optical linewidth of the prepared hole vs laser intensity according to the FID measurements and the Bloch theory is shown in Fig 4.15. The laser intensity is expressed as the 1/2π x Rabi frequency at the centre of the laser beam. The holewidth was calculated from the observed FID decay time T_{obs} using the relationship

$$\Delta\nu = (1/2\pi)\left(\frac{1}{T_{obs}} - \frac{1}{T_2}\right) \qquad (4.24)$$

Also shown in Fig 4.15 are three theoretical results. The first (a) shows the result of integrating Equation 4.20 across the beam profile and setting T_2=55 μs, the value determined from the PE measurements. The second (b) trace is identical except that T_2 was adjusted to fit the experimental results. The value of T_2 obtained in this way is 125 ±15 μs. The final (c) trace assumes that the laser is plane wave and that the Rabi frequency is given by 2π times the nutation frequency.

Fig 4.16a shows the transient signal observed on applying the CPL pulse sequence. The laser power was 45 mW and the π/2 pulse was 4 μs long. After the initial nutation signal decays, a long-lived transient response was observed to decay exponentially with a lifetime of 115 ± 5 μs. The magnitude of this transient was found to be maximised for the 4 μs delay. This signal was also found to be reduced if the 90° phase shift in the driving field was increased or decreased by 30°. Fig 4.16b shows the transient response when the phase shift was reduced to zero. For this case no long-lived transient signal was observed.

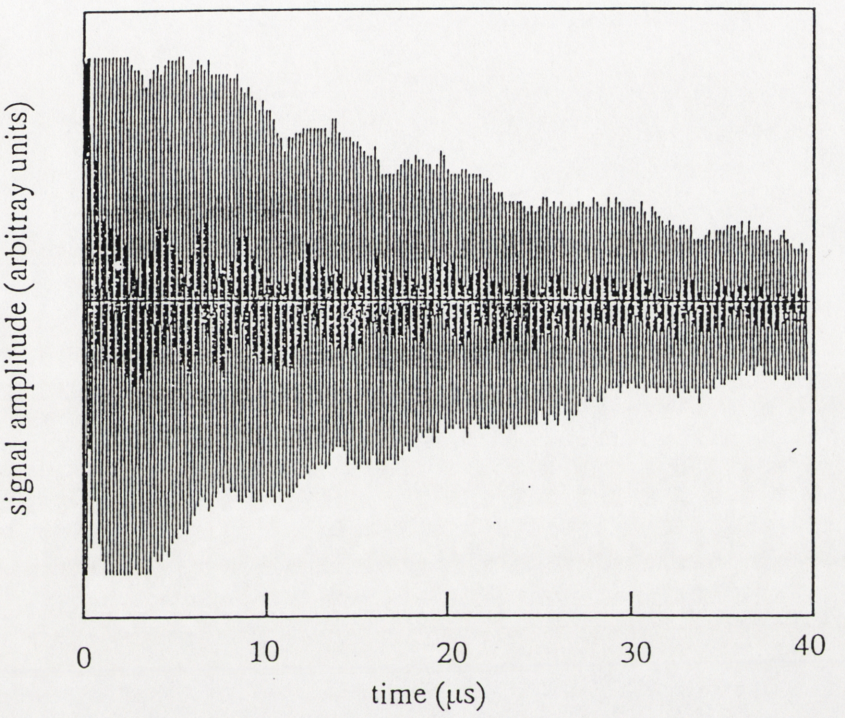

Figure 4.14. FID signal obtained with a laser power of 0.05 mW. The decay time of the signal is 21.5 μs. The high frequency fluctuations on the signal are at the heterodyne frequency. The slower modulation of the envelope is a result of an aliasing of the digital storage scope's sampling rate with the high frequency modulation.

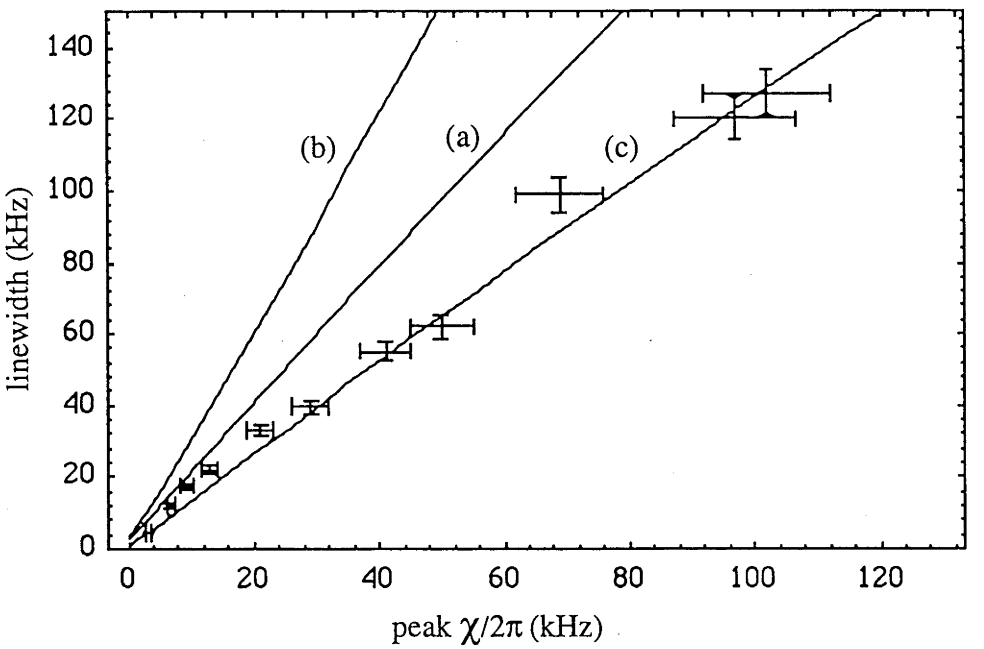

Figure 4.15. Optical linewidth $\Delta\upsilon$ (HWHM) of the prepared hole (as inferred from FID measurements) vs $1/2\pi$ times the peak Rabi frequency. Curve (a) represents the prediction of the OBE's (with T_2=55 μs, as measured using PE) where the polarisation was integrated across the laser beam profile. Curve (b) is the same as (a) but with the laser treated as a plane wave. Curve (c) is the same as (a) but with T_2 adjusted to fit the experimental data. The resulting value for T_2 was 125 μs.

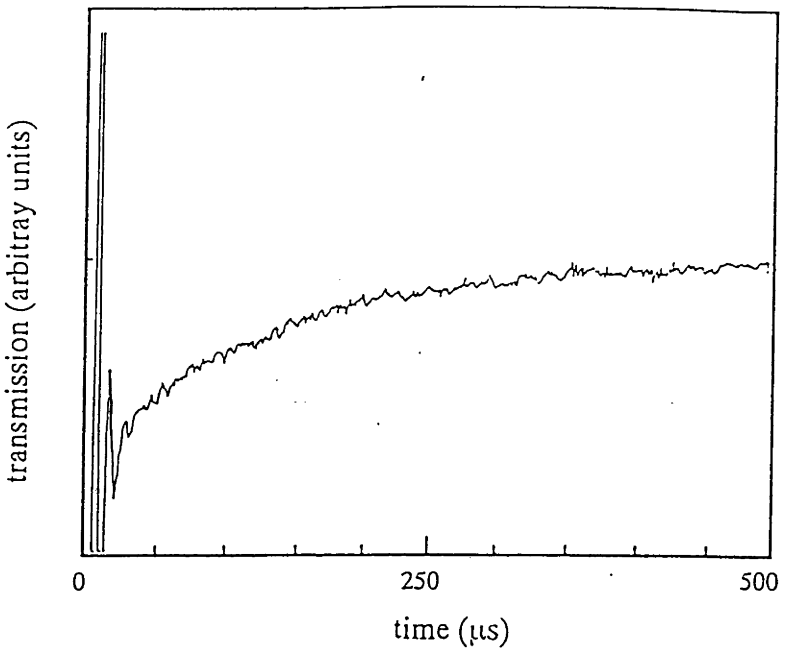

Figure 4.16 a. The transient response resulting from the CPL pulse sequence. The laser intensity was 45 mW, and the initial $\pi/2$ pulse was 4 μs long.

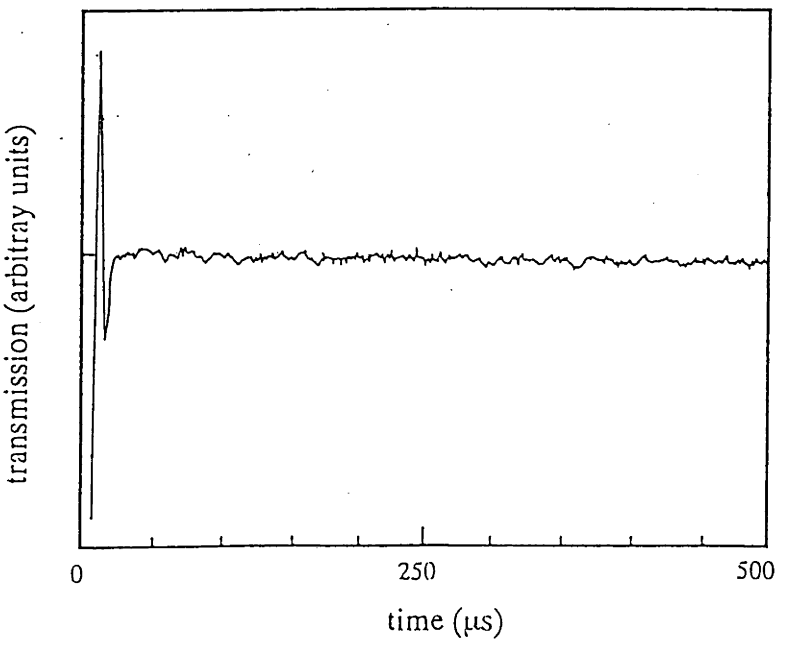

Figure 4.16 b. The transient response resulting from switching the laser power from zero to 45 mW.

The lifetime of the decay as predicted by Torrey's solution using T_2=55 μs is 58 μs, significantly shorter than the observed value. For this calculation it was assumed that the laser beam was a plane wave. As the decay rate of this transient is not very sensitive to laser intensity this assumption results in only a small error. The value of T_2 obtained by fitting the OBE's to Fig 4.16 a was 110± 5 μs. This value is in reasonable agreement with the value of T_2 determined from the high intensity FID measurements of 125 ± 15 μs.

4.5. Discussion

In the present work it was found that the holewidths inferred from the FID measurements are power broadened to a lesser extent than predicted by the OBE's. This result bears similarities to the FID observations of DeVoe and Brewer [1983] in $LaF_3:Pr^{3+}$, and Szabo and Muramoto[1989] in ruby. Both experiments demonstrated that T_2 approached T_1 for strong driving fields. In the present case T_2 increased to only 125 μs, one-fourth the value of T_1. There are two likely contributions to this discrepancy between the present work and the previous observations. The first is that in the present work the intensity profile of the laser beam was taken into account when calculating the intensity dependence of the FID decay rate, which as stated earlier was not in the other two works. As can be seen in Fig 4.15, failing to consider the beam profile exaggerates the line narrowing effects attributed to the non-OBE behaviour. The other possible contribution to the discrepancy is the presence of strong instantaneous spectral diffusion in $KEu(WO_4)_2$. The phase perturbations acting on the ions, due to instantaneous spectral diffusion, will increase as the laser intensity is increased, partially counteracting the line-narrowing effect of the intense driving field.

Instantaneous spectral diffusion may also account for the observed decay rate of the RE measurements being significantly greater than predicted by the OBE's. Any effect of line-narrowing due to the strong driving field, evident in the FID measurements, appears to be destroyed by instantaneous spectral diffusion. As with the results in rotary echo measurements in ruby [Muramoto and Szabo1988] the line-narrowing effects due to a strong driving field appear to be stronger in the FID measurements than in the RE measurements.

The observation that the decay rate of the CPL signal was longer than the prediction of the OBE's is the first direct observation, in an optical system, of line narrowing due to a strong driving field. In FID measurements the line narrowing must be inferred from the reduced power broadening and depends on the reliability of the measurement of the Rabi

frequency. Although both CPL and FID are predominantly sensitive to ions whose dipole moments are in-phase with the driving field, these transient techniques are otherwise very different from each other. That similar line narrowing effects were observed in CPL and FID measurements, but not for RE, lends weight to the proposal that the relative phase of the driving field and the dipole moment is an important parameter in non-OBE behaviour and merits further investigation.

With the demonstration of CPL it is now possible to consider more general experiments, that measure the relaxation of the coherence for a wider range of the relative phase of the driving field and dipole moment. The simplest extension is to use the CPL pulse sequence but to vary either the initial pulse area or the amplitude of the phase shift in the driving field. This will result in a component of the dipole moment of the on resonance ion being in-quadrature with the driving field. As with the pure CPL measurements, phase sensitive detection can be used to observe the relaxation of the in-phase component of the dipole moment.

To observe the relaxation of the in-quadrature component of ions driven by a field predominantly in-phase with the dipole moments a pulse technique can be used which is a hybrid of the CPL and RE pulse sequence. The pulse sequence is shown in Fig 4.17. It consists of a $\pi/2$ pulse followed by a 90^{o} phase shift and then a 180^{o} phase shift. Either the initial pulse area, or the amplitude of the phase shift in the driving field, could be varied. The 180^{o} phase shift in the driving field is used to rephase the in-quadrature component of the dipole moments of the inhomogeneously broadened line. This rephasing will result in an echo which is observable as an amplitude modulation. The decay of the amplitude of this echo with the delay of the 180^{o} phase shift is a measure of the relaxation of the in-quadrature component of the dipole moment.

Although the CPL technique has been clearly demonstrated in this present work, before making further use of this technique in the study of non-OBE behaviour a number of improvements should be made to the experimental procedure. One obvious improvement is to use a variable phase plate to control the phase of the local oscillator with respect to the probe beam. Another is to use a sample whose dephasing mechanism can be more easily characterised, such as Pr^{3+}:LaF_3 or ruby. To extend this technique to samples like Pr^{3+}:LaF_3, which absorbs all polarisations of light, it will be necessary to use a local oscillator external to the sample. It would also be useful to allow for the switching of the laser intensity immediately after the $\pi/2$ pulse in the CPL pulse sequence. The intensity dependence of the CPL signal could easily be studied using the same length $\pi/2$ pulse.

4.6. Conclusion

The intensity dependence of FID rates displayed a non-OBE behaviour similar to that observed by DeVoe and Brewer [1983] in Pr^{3+}:LaF_3 and Szabo in ruby [Szabo and Muramoto 1989]. The value of T_2 determined from the intensity dependence of the FID rates was 125 ± 15 μs. In a result similar to that from previous work in ruby [Muramoto and Szabo1988] the rotary echo signals did not show any sign of line narrowing effects due to the presence of a strong driving field. In fact their decay rate was found to be significantly faster than predicted by the non-OBE's. Coherence phase locking has been demonstrated in the inhomogeneously broadened $^7F_0 \Rightarrow {}^5D_0$ optical transition in $KEu(WO_4)_2$. The lifetime of the signal was found to be 115 ± 5 μs . This value is nearly twice the value predicted by the OBE using the value for T_2 of 55 ± 2 μs (determined from photon echo measurements). This is the first direct observation of the decrease in the dephasing rate due to the presence of a strong optical driving field. The value for T_2 determined by fitting the OBE's predictions to the observed decay rate was 110 ± 5 μs. This value was found to be in agreement with the value determined from the intensity dependent FID measurements.

It was further shown in the theoretical section that for both FID and CPL the ions contributing to the signal have their dipole moments predominantly in-phase with the driving field, while for RE the dipole moments of the ions contributing to the signal are predominantly in-quadrature with the driving field. It was proposed that the apparent inconsistency between the different transient techniques in regard to the non-OBE behaviour is related to the relative phase of the driving field and the ions' dipole moments. The observation of similar line narrowing effects in the CPL and FID measurements, but not for RE, is strong evidence for the validity of this proposal. Further experiments to investigate the dependence of the coherence dephasing on the relative phase of the driving field and the dipole moment have been suggested.

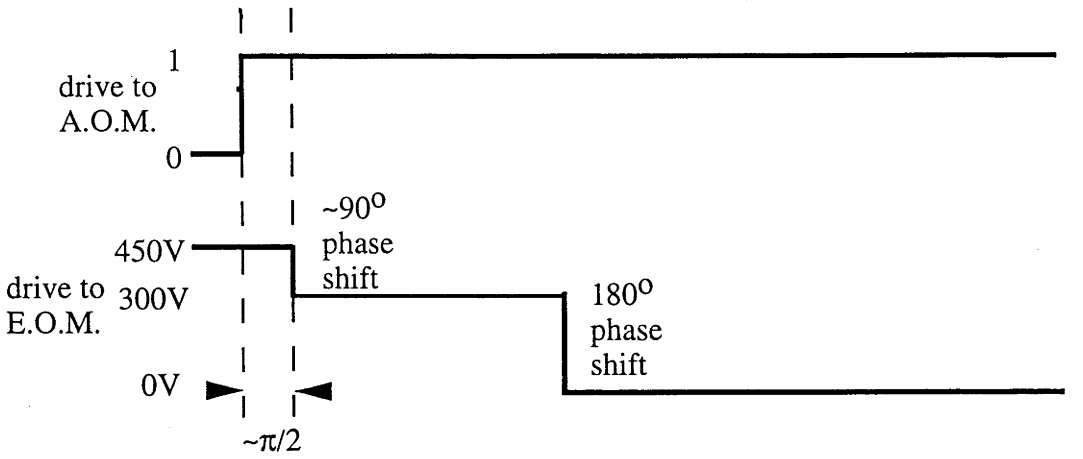

Figure 4.17. Hybrid pulse sequence for observing the in-quadrature component of the dipole moment of ions driven by a field predominantly in-phase with the dipole moments. The phase between the driving field and the dipole moment can be controlled by adjusting the area of the initial "π/2" pulse or the amplitude of the 90°" phase shift. Indicated in the figures are the drive levels to the acousto-optic modulator and electro-optic modulator, used to control the amplitude and phase of the optical driving field respectively.

Chapter 5 Spectral holeburning in $LaF_3:Pr^{3+}$

5.1 Introduction

As discussed in Chapter 1, $LaF_3:Pr^{3+}$ possesses nuclei with relatively large magnetic moments. It is therefore not the sample of first choice for applications where the narrowest possible homogeneous linewidth is desired. The $^3H_4 \Rightarrow {}^1D_2$ transition in $LaF_3:Pr^{3+}$ provides an interesting case study on the effects magnetic interaction can have on a rare-earth optical transition, however. It is important to understand these interactions because whilst they are significantly reduced in samples like $Y_2O_3:Eu^{3+}$ they are nevertheless present. Besides increasing the homogeneous linewidth by increasing the dephasing rate, magnetic interactions can also wash out holes burnt into an inhomogeneous optical profile. This may occur either through the relaxation of the groundstate hyperfine levels or via a process known as spectral diffusion (SD). Spectral diffusion is the result of random shifts in the transition frequencies of the individual ions, occurring on time scales comparable or longer than the transition's coherence memory.

In spectral holeburning measurements spectral diffusion is expected to be seen as a broadening of the hole over time. In this chapter, time resolved spectral holeburning of the $^3H_4 \Rightarrow {}^1D_2$ optical transition in $LaF_3:Pr^{3+}$ is used to study the evolution of holes over time intervals from 1 ms to 10 s after burning the hole. The magnetic field dependence of the observed hole broadening is studied to determine the nature of the mechanism producing it. It is shown that a major contribution to the hole broadening is in fact not a spectral diffusion process but rather a process related to the cross-relaxation between Pr^{3+} ions, involving their groundstate hyperfine levels.

The optical transition to be studied is at 592.52 nm and involves the lowest crystal field levels of the $^3H_4$ and $^1D_2$ states of the Pr^{3+} ion (see Fig 5.1). The LaF_3 crystal possesses a D_{3d}^4 symmetry [Zalken *et al.* 1966]. The Pr^{3+} ion occupies the La position in the crystal, which has a C_2 symmetry. There are three pairs of such sites in the LaF_3 crystal, related by transformations about the C_3 axis of the crystal. The sites within each pair are related by inversion. In this C_2 symmetry all the Pr^{3+} ion's electronic levels are non-degenerate. The nuclear spin levels of the ground and excited states for ^{141}Pr (the only stable isotope), with spin 5/2, each consist of three doubly denegerate levels with splittings on the order of 10 MHz. The splittings are due to the second order hyperfine interaction and electric quadrupole interactions. Erickson demonstrated laser induced optical holeburning on the $^3H_4(\Gamma_1) \Rightarrow {}^2D_1(\Gamma_1)$ resulting from an optical pumping cycle that redistributes the ground state hyperfine population [Erickson 1977a] (see Fig 5.2).

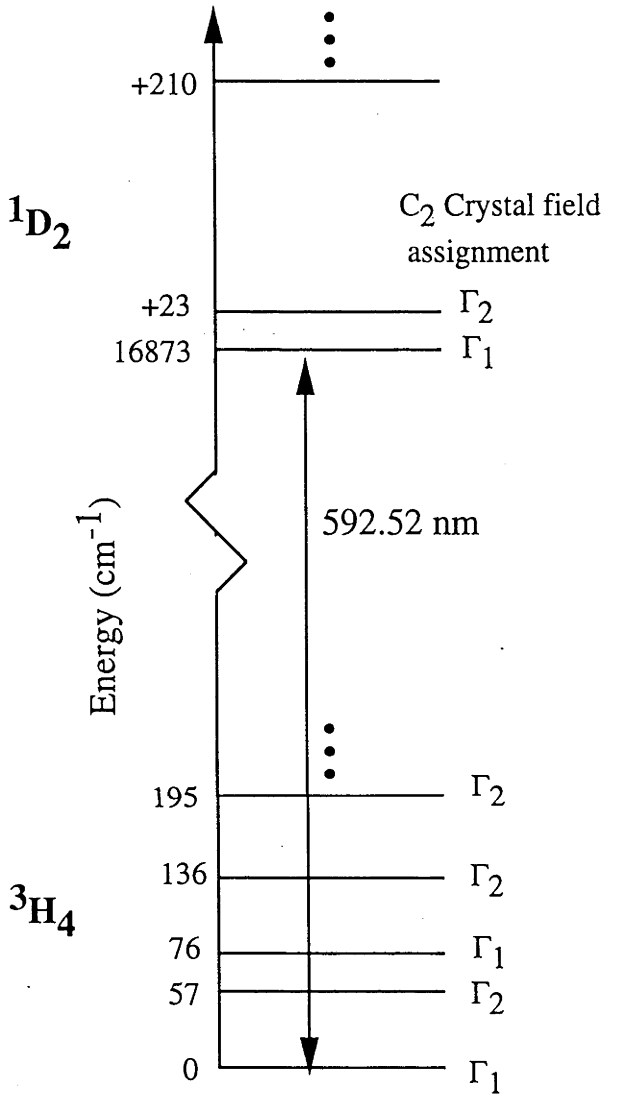

Figure 5.1. Crystal field energy level diagram of $LaF_3:Pr^{3+}$, indicating the optical transition of interest between the lowest crystal field levels of the $^3H_4$ and $^1D_2$ states

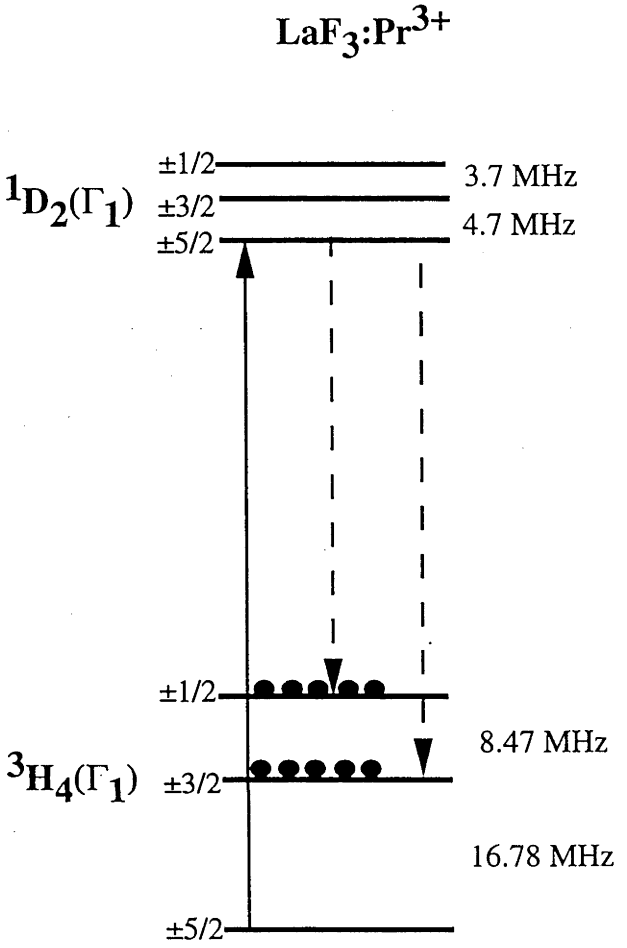

Figure 5.2 Quadrupole energy level splittings of the $^3H_4(\Gamma_1)$ and $^1D_2(\Gamma_1)$ electronic levels of $LaF_3:Pr^{3+}$. One of the nine possible optical pumping cycles is illustrated.

The relaxation of the population within the ground state hyperfine levels was found to depend on temperature, the Pr^{3+} concentration and the particular hyperfine levels involved [Shelby *et al.* 1980]. Below temperatures of 2 K the hole lifetime was found to be independent of temperature and for Pr^{3+} concentrations less than 0.05% hole lifetimes in excess of several seconds were observed. Spectral holeburning allows narrow frequency packets of Pr^{3+} ions to be tagged and the evolution of their optical frequencies to be observed over time intervals considerably longer than the lifetime of the optically excited state.

The magnetic interactions affecting the $^3H_4(\Gamma_1) \Rightarrow {}^2D_1(\Gamma_1)$ optical transition in $LaF_3:Pr^{3+}$ have been studied by a number of authors[Muramoto *et al.* 1992,Wald *et al.* 1992, Shelby *et al.* 1980, Rand *et al.* 1979, Macfarlane *et al.* 1980]. Much of this interest has been concerned with interactions between the Pr^{3+} ion and the magnetic moments of the surrounding ^{19}F nuclei, and the dynamics of these ^{19}F nuclear spins. The two electronic states of interest possess no first order magnetic moment but they do possess enhanced nuclear moments which are of the same order of magnitude as the moments of the ^{19}F nuclei. The presence of the enhanced moment of the electronic groundstate detunes the Larmor frequency of the nearest neighbour (N-N) ^{19}F nuclei from that in the bulk crystal [Shelby *et al.* 1978]. The detuning of these ^{19}F nuclei will affect their dynamics.

The magnetic interactions between the Pr^{3+} ion and the ^{19}F nuclei have also be investigated by studying the hyperfine transitions associated with the Pr^{3+} ion. Erickson using CW optical detected NMR (ODNMR) determined the inhomogeneous linewidth of the ground state I=5/2 to 1/2 transition to be 180 kHz [Erickson 1977b]. This width agreed with estimates he made based on the magnitude of the magnetic moments of the Pr^{3+} ion and ^{19}F nuclei. Using ODNMR free induction decay Shelby *et al.* found the linewidth of the ground state I=5/2 to 3/2 hyperfine transition to be 230 kHz; in reasonable agreement with Erickson's result [Shelby *et al.* 1978]. Using ODNMR spin echoes, Shelby also measured the homogeneous linewidth of the same transition and found it to be only 20 kHz.

It was concluded by Shelby *et al.* that inhomogeneities in the local magnetic field from the ^{19}F nuclei at Pr^{3+} sites were responsible for the 230 kHz linewidth. The 20 kHz homogeneous linewidth was explained by assuming that the greater proportion of the local magnetic field is static on the time scale of the dephasing time T_2.

From NMR measurements the cross relaxation rate between ^{19}F nuclei in the bulk crystal has been determined to be of the order of 100 kHz [Wong *et al.* 1983]. If this rate applied to all the ^{19}F nuclei interacting with the Pr^{3+} ion then the entire local field would be expected to be dynamic on the time scale of the hyperfine coherence time $T_2 = 16$ μs. It was proposed by Shelby *et al.* , to explain their observed value for the homogeneous linewidth of the F=5/2 ⇒ 3/2 transition, that the N-N ^{19}F nuclei are inhibited from making a resonant spin flip-flop in times of the order of T_2 or shorter [Shelby *et al.* 1978].

The dephasing of the optical transition has also been shown to be dominated by the response of the ground and excited state hyperfine levels to the fluctuations in the local field from the ^{19}F nuclei. The first measurement of the homogeneous linewidth of the optical transition not limited by instrument resolution was made by MacFarlane *et al.* using photon echo measurements [MacFarlane *et al.* 1979b]. They found the homogeneous linewidth to be 56 kHz (FWHM) in zero applied magnetic field, 14 kHz for a 80 G field applied perpendicular to the C_3 axis of the crystal, and 12 kHz for the same field applied along the C_3 axis. The narrowing of the homogeneous linewidth with the application of a magnetic field was attributed to the applied field quantising the fluorine nuclear spins along the field reducing the off-diagonal coupling between the fluorine nuclei and thus slowing the mutual flip rate. The remaining dephasing in the presence of the field was attributed to the interaction with ^{19}F nuclei outside the frozen core of N-N ^{19}F nuclei.

That the dephasing in the optical transition was primarily due to the ^{19}F nuclear spins was conclusively proven by reducing the dephasing rate through the use of nuclear spin decoupling techniques on the ^{19}F nuclei [Rand *et al.* 1979, Macfarlane *et al.* 1980].

Because the rate of mutual spin flips involving the N-N ^{19}F nuclei is slower than the dephasing rate of the optical transition, the fluctuations in the local field at the Pr^{3+} site due to these mutual spin flips will be a source of spectral diffusion rather than dephasing. This spectral diffusion should saturate after reaching the total contribution to the inhomogeneous linewidth due to the Pr - F magnetic interaction. The rate of this spectral diffusion depends on the spin flip rate of the N-N F's. Two apparently conflicting estimates of the rate at which the N-N ^{19}F undergo mutual spin-flips have been made based on the results of two experiments.

T.Muramoto *et al.* [1992] studied the spectral diffusion in the hyperfine transitions in the $^3H_4$ ground state, over the time interval of 10 μs to 1000 μs. They measured the decays

of two pulse spin echoes, three pulse stimulated spin echoes and Carr-Purcell multiple pulse spin echoes for the hyperfine transitions using the Raman heterodyne detection technique between each other. The decay rates observed were consistent with the presence of spectral diffusion, which they attributed to the reorientation of the spins of the N-N F's through cross-relaxation. The spectral diffusion was observed to saturate after several hundred μs. This suggests a mutual spin-flip rate for the N-N F's in the 1 - 10 kHz range. Muramoto also observed on the same time scale spectral diffusion in the $^3H_4(\Gamma_1) \Rightarrow {}^2D_1(\Gamma_1)$ optical transition using 3 pulse photon echoes.

Wald *et al.* obtained an estimate of the N-N F spin flip rate by studying the cross-relaxation rate of the N-N ^{19}F nuclei with the Pr ground state hyperfine levels and also with the bulk F nuclei [Wald *et al.* 1992]. A magnetic field was chosen such that a pair of the $^3H_4$ ground state hyperfine energy levels of the Pr^{3+} ion matched the ^{19}F Larmor frequency. At this level crossing condition cross-relaxation interactions between the Pr^{3+} hyperfine transitions and the N-N F spins can repopulate Pr^{3+} hyperfine levels emptied by optical pumping. The level crossing condition was detected as an enhanced absorption of the pumping laser. From holeburning measurements the cross relaxation rate between the Pr spins and the N-N F was determined to be 100 Hz. The coupling of N-N F spins to the bulk F spins during Pr - F cross-relaxation was determined by NMR measurements of the bulk F spin magnetisation using free induction decay. The rate of cross-relaxation between the Pr^{3+} spins and the bulk F was measured by maintaining the Pr^{3+} spins at an infinite temperature, using two rf sources tuned to two of the hyperfine splittings, and monitoring the spin temperature of the bulk F's. This should reflect the cross relaxation rate of the N-N F's with the bulk F's as the strongest mechanism for the cross relaxation between a Pr ion and a bulk F is via N-N F nuclei as intermediaries. No cross relaxation between the Pr spins and the bulk F's was observed. From this result an upper limit on the cross relaxation rate between the N-N F's and the bulk F's of 0.03 Hz was set. This value is 5 orders of magnitude slower than the cross relaxation rate determined by Muramoto.

In comparing these results, there are two fundamental differences between these two experiments that should be considered. One major difference is in the applied magnetic field used in the two experiments. Due to a chemical shift the detuning of the N-N F's from the bulk F's continuously increases with increases in the applied magnetic field. The cross-relaxation rate of the N-N F's can therefore be expected to slow down with increasing magnetic field. Wald *et al.* used a field of 2.8 kG applied along a C_2 axis of the crystal, chosen to give a level crossing condition. The spectral diffusion measurements of Muramoto were made in a relatively small field of 100 G along the C_3

axis of the crystal. The effect of the 2.8 kG magnetic field used by Wald will be considered in Section 5.2.9.

A further difference was that Muramoto *et al.* by monitoring the spectral diffusion of the ground state hyperfine transitions, observed the reorientation of the N-N F's. This reorientation could occur through cross relaxation amongst the N-N F's as well as through cross-relaxation with the bulk F's. The measurements of Wald *et al.* were sensitive only to cross-relaxations of the N-N F's with the bulk F's.

By using spectral holeburning to study the spectral diffusion operating on time scales longer than investigated by Muramoto and over a wider range of magnetic fields, it was hoped that further insight into the dynamics of the N-N ^{19}F nuclei could be gained and the measurements of Wald *et al.* and Muramoto *et al.* could be reconciled.

An important mechanism that must be considered when making holeburning measurements, and one that may hinder investigations of spectral diffusion is the cross-relaxation of the groundstate hyperfine levels between Pr^{3+} ions. The cross relaxation of the ground state hyperfine levels was identified by Shelby *et al.* as a likely mechanism for recovery of the optical hole [Shelby *et al.* 1980]. The hole filling comes about because the two Pr^{3+} ions participating in the cross-relaxation can have different optical transition frequencies (see Fig 5.3). If the optical frequencies of the ions are uncorrelated with their positions, the cross-relaxations will redistribute the hyperfine excitations associated with the hole, across the optical inhomogeneous line. In the same work Shelby *et al.* also suggested that this mechanism may broaden the hole, rather than filling it in, if a correlation exists between the crystalline environments (and hence between the optical frequencies) of nearby Pr^{3+} ions. They cited the slower than predicted decay rate of the spectral hole (from an estimate of the Pr-Pr cross relaxation rate) as evidence that this broadening was possibly operating. The exact behaviour of this hole broadening depends on both the spatial distribution of the Pr^{3+} ions and on the spatial correlation of the crystal strain field.

Spectral holeburning will also be used to look for structure in the optical transition associated with the Pr-F magnetic interactions. Because the enhanced nuclear moment of the Pr^{3+} ion is different for the $^3H_4$ and $^1D_2$ states optical transitions between these states will change the magnitude and direction of the local field seen by the N-N F. This change in the magnetic field results in a finite probability of optical transitions where the spin of a F nuclei is flipped. The relative strength of these transitions will be estimated in Section 5.2.6. These transitions should appear as side hole structure in the holeburning

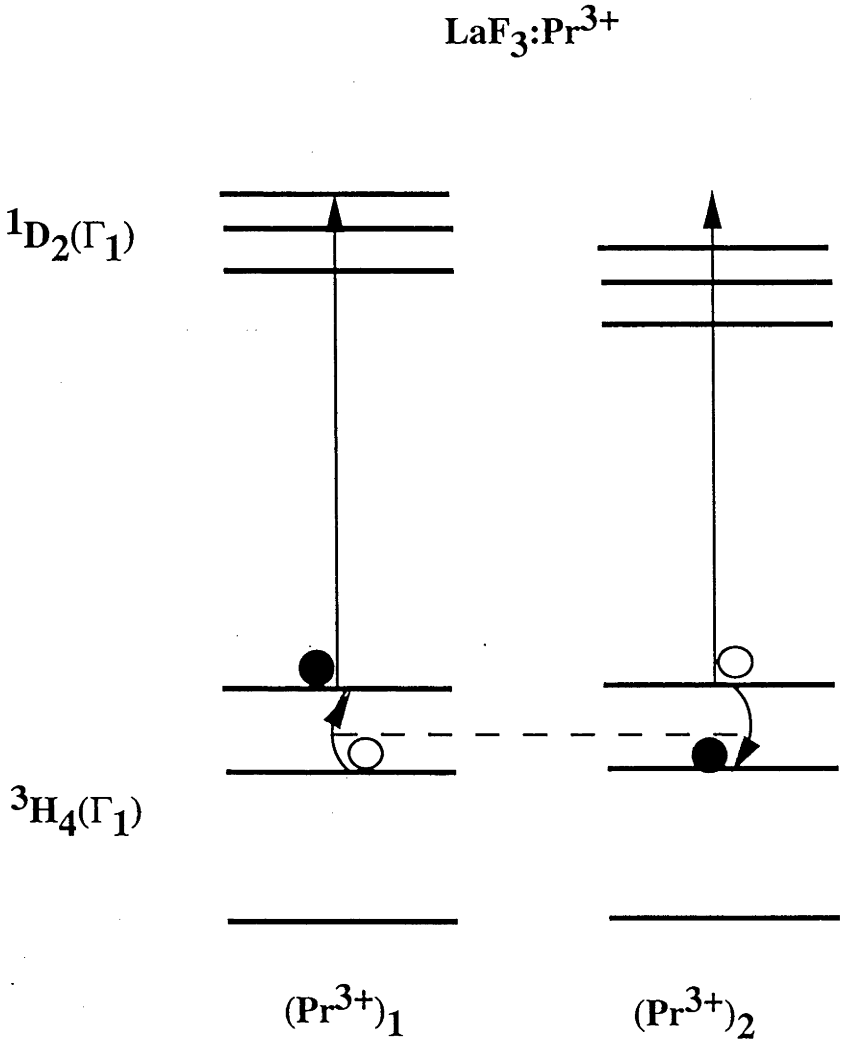

Figure 5.3 Cross-relaxation between two Pr^{3+} ions resulting in either hole recovery or hole broadening. The optical transition frequencies of the two ions differ due to strain broadening.

spectra. The splitting of these side holes from the central hole in a magnetic field should go as the gyromagnetic ratio of the ^{19}F (4 kHz/G) for applied fields greater than the local field due to the Pr moment. A simple energy level diagram of the coupled Pr-F system and the optical spin-flip transitions is shown in Fig 5.4. Similar neighbouring spin-flip transitions have been observed in the hole spectrum of $^4I_{15/2} \Rightarrow {}^4F_{9/2}$ optical transition in $LiYF_3:Er^{3+}$ [Wannemacher *et al.* 1991]. In this case the optical F spin-flip transitions were induced by the large first order electronic magnetic moment of Er^{3+}.

5.2 Theoretical background

In this section the contribution of the Pr-F superhyperfine interaction to the linewidths of both the hyperfine and optical transitions are calculated. The relative intensity of the F spin flip optical transitions will also be calculated. In both calculations the interaction of Pr ion with each ^{19}F nuclei will be treated separately. The effects of a large applied magnetic field on the Pr-F interaction is also considered.

At the end of this section the Pr-Pr cross relaxation rate between the ground state hyperfine levels will be estimated.

5.2.1 Hyperfine coupling in $LaF_3:Pr^{3+}$

Before considering the superhyperfine interactions it will be necessary to first review the hyperfine coupling theory for $LaF_3:Pr^{3+}$.

The general Hamiltonian describing the 4f electron states in a rare earth ion can be written as,

$$H = H_{IF} + H_{CF} + (H_{HF} + H_{Q} + H_{Z} + H_{z}) \qquad (5.1)$$

The first term is the free ion Hamiltonian which includes the spin-orbit interaction and the second is the crystal field Hamiltonian. The bracketed terms make a much smaller contribution; they are, in order of appearance, the hyperfine coupling between the 4f electrons and the rare earth nucleus H_{HF}, the nuclear quadrupole interaction H_Q, the electronic Zeeman interaction H_Z and the nuclear Zeeman interaction H_z.

The bracketed terms in (5.1) can be treated as a perturbation of the crystal field wavefunctions (ie. the eigenstates of the first two terms of the Hamiltonian). From

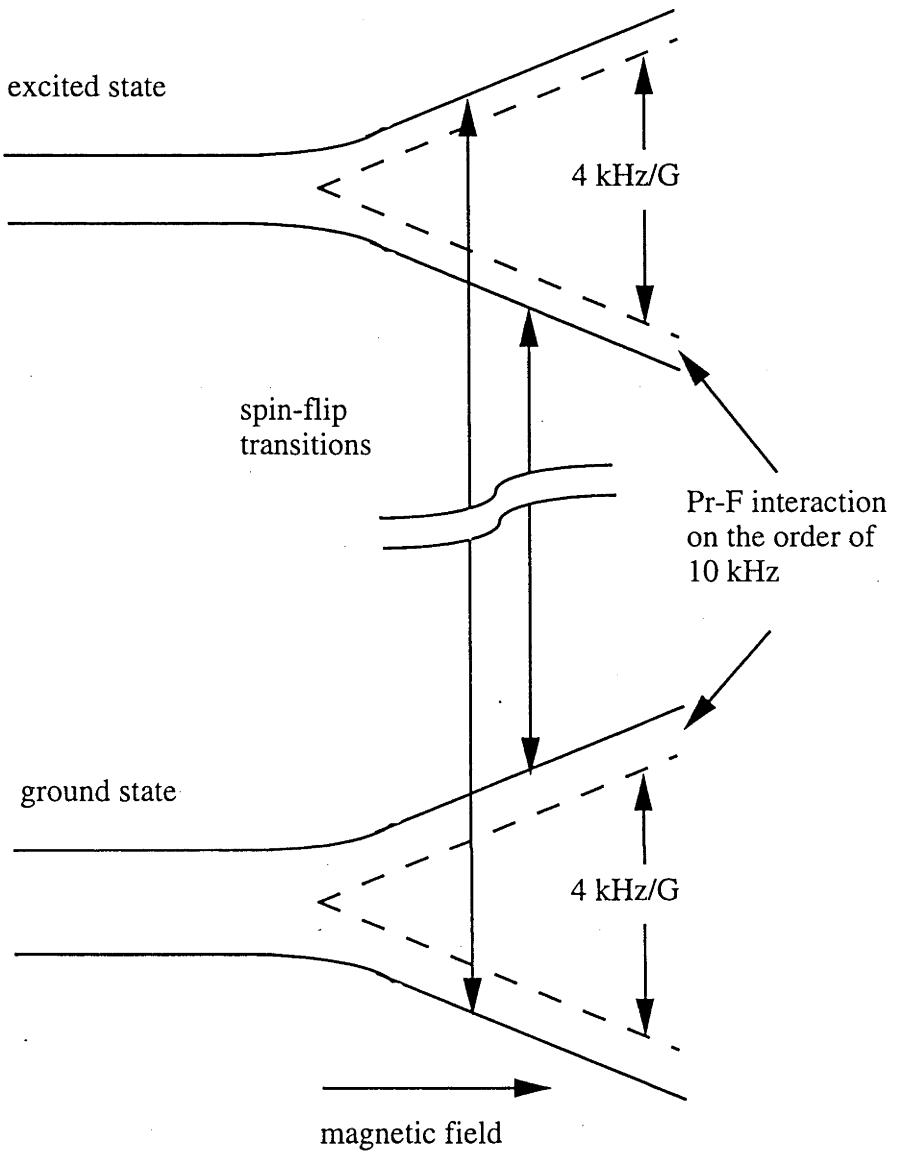

Figure 5.4. Energy level diagram of the coupling between a Pr^{3+} ion with a single ^{19}F nuclei, showing the two optical spin-flip transitions. For simplicity the hyperfine structure of the Pr^{3+} ion has been ignored.

perturbation theory it is possible to derive an effective Hamiltonian describing the effects the bracketed terms have on a single crystal-field level.

For Pr^{3+}, which is a non-Kramers' ion, sitting in a site of low symmetry (eg. the C_2 site in LaF_3) the electronic degeneracy of a given J-state is completely lifted, and the electronic angular momentum is quenched to first order. The hyperfine and electronic magnetic effects appear in the second order of the perturbation treatment. The effective Hamiltonian including nuclear Zeeman and nuclear quadrupole interactions, is given by [Teplov 1968]

$$\begin{aligned} H_{eff} &= -\left(2A_J g_J \mu_J \mathbf{H}\cdot\Lambda\cdot\mathbf{I} - H_z\right) - \left(A_J^2 \mathbf{I}\cdot\Lambda\cdot\mathbf{I} + H_Q\right) - g_J^2 \mu_B \mathbf{H}\cdot\Lambda\cdot\mathbf{H} \\ &= H_z' + H_Q' - g_J^2 \mu_B \mathbf{H}\cdot\Lambda\cdot\mathbf{H} \end{aligned} \tag{5.2}$$

where g_J is the Lande g-value

$$g_J = \left(\frac{3}{2}\right) - \frac{[L(L+1) - S(S+1)]}{[2J(J+1)]}, \tag{5.3}$$

H is the applied magnetic field, μ_B is the Bohr magneton, A_J is the hyperfine coupling constant for the LSJ states of interest, and the tensor Λ is given by

$$\Lambda_{\alpha\beta} = \sum_{n=1}^{2J+1} \frac{\langle 0|J_\alpha|n\rangle\langle 0|J_\beta|n\rangle}{\Delta E_{n,0}} \tag{5.4}$$

with $|0\rangle$ being the level to which H_{eff} applies, the $|n\rangle$'s being the other crystal field levels, and $\Delta E_{n,0}$ being the energy difference $E_n - E_0$. The first term in Equation 5.2 is the enhanced nuclear Zeeman Hamiltonian and can be written as,

$$H'_z = \gamma_x H_x I_x + \gamma_y H_y I_y + \gamma_z H_z I_z \tag{5.5}$$

γ_x,γ_y and γ_z are the effective enhanced nuclear gyromagnetic ratios along the principal axes of the Λ-tensor, and are given by

$$\gamma_\alpha = \gamma_N + \frac{2g_J \mu_B A_J \Lambda_{\alpha\alpha}}{h} \tag{5.6}$$

H'_Q consists of two parts. The first, H_Q, describes the interaction of the quadrupole moment of the nucleus with the electric field gradient (EFG), and has the form

$$H_Q = P\left[\left(I_{z'}^2 - \frac{I(I+1)}{3}\right) + \frac{\eta}{3}\left(I_{x'}^2 - I_{y'}^2\right)\right] , \qquad (5.7)$$

where P is the quadrupole coupling constant, η is the EFG asymmetry parameter and x', y' and z' are the principal axes of the EFG tensor. The EFG has contributions from the lattice, from the f-electrons and from the closed shells whose charge distribution is distorted by the electric field of the lattice. The latter is the Sternheimer anti-shielding effect and is often the dominant term. The second part of H'_Q is the second order magnetic hyperfine interaction, which is also known as the pseudo-quadrupole interaction [Baker and Bleaney 1958] as it can be written in the same form as H_Q, ie.

$$H_{pq} = D_{pq}\left[\left(I_z^2 - \frac{I(I+1)}{3}\right) + E_{pq}(I_x^2 - I_y^2)\right] \qquad (5.8)$$

where D_{pq} and E_{pq} can both be written in terms of the tensor Λ as

$$Dpq = A_J^2\left[\frac{1}{2}(\Lambda_{xx} + \Lambda_{yy}) - \Lambda_{zz}\right] , \qquad (5.9)$$

$$Epq = A_J^2\frac{1}{2}(\Lambda_{xx} - \Lambda_{yy}) . \qquad (5.10)$$

The principle axes of Λ (x,y,z) and hence H_{pq} do not necessarily coincide with the principal axes of the H_Q (x', y', z'). All the tensors will have one of their principal axes aligned along the C_2 axis. H'_Q is obtained by summing H_Q and H_{pq} in a common reference frame. When the result is diagonalised it can be written in the form:

$$H'_Q = D\left[\left(I_{z''}^2 - \frac{I(I+1)}{3}\right) + E\left(I_{x''}^2 - I_{y''}^2\right)\right] , \qquad (5.11)$$

where x", y", and z" form a third set of principal axes.

The last term in (5.2) is the quadratic electronic Zeeman shift.

5.2.2 Matrix calculations

In this section matrices for the quadrupole and nuclear Zeeman interactions are given for a system with I=5/2 and a site with at least one axis of symmetry (for $LaF_3:Pr^{3+}$ the C_2

axis). The different terms in the Hamiltonian must be expressed in a common basis set and as we are dealing with a situation where the principal axes of the different tensor quantities are not congruent, it is necessary to write these terms in a co-ordinate frame other than their principal axes.

The total quadrupole Hamiltonian H'_Q can be written in matrix form using the eigenstates of I and I_Z' as basis functions. The symmetry axis of the site is a convenient choice for the z axis in the calculations as all the tensor quantities share it as a principal axis. The choice of the x-axis is more arbitrary, in the case of $LaF_3:Pr^{3+}$ setting it to be parallel to the C_3 axis of the crystal facilitates comparison with experiments.

In a co-ordinate system congruent with its principle axis, H_Q' can be written as

$$H'_Q = \begin{bmatrix} I_x & I_y & I_z \end{bmatrix} \begin{bmatrix} V_{xx} & 0 & 0 \\ 0 & V_{yy} & 0 \\ 0 & 0 & V_{zz} \end{bmatrix} \begin{bmatrix} I_x \\ I_y \\ I_z \end{bmatrix} \tag{5.12}$$

where

$V_{zz} = \frac{2}{3}D,$

$V_{xx} = E - \frac{D}{3},$

$V_{yy} = E + \frac{D}{3}.$

To move to a co-ordinate frame with the x-axis parallel with C_3 and the z-axis parallel to the C_2 it is necessary to transform the matrix V such that

$$V' = R\,V\,R^T \tag{5.13}$$

where R is the matrix for the rotation about the z-axis,

$$R = \begin{bmatrix} \cos\theta & \sin\theta & 0 \\ -\sin\theta & \cos\theta & 0 \\ 0 & 0 & 1 \end{bmatrix} \tag{5.14}$$

θ is the angle between the x-axis of the principle axis system of H'_Q and C_3.

In this new basis set

$$H'_Q = \frac{3}{2}V_{zz}\left(I_z^2 - \frac{1}{3}I(I+1)\right) + \frac{(V_{xx} - V_{yy})}{4}\left[\cos 2\theta(I^+I^+ + I^-I^-) + i\sin 2\theta(I^+I^+ - I^-I^-)\right] \tag{5.15}$$

which can be written in matrix form

$H'_Q =$

I_z / I_z	$5/2$	$3/2$	$1/2$	$-1/2$	$-3/2$	$-5/2$
$5/2$	$\frac{10}{3}D$	0	$\sqrt{10}Ee^{i2\theta}$	0	0	0
$3/2$	0	$\frac{-2}{3}D$	0	$3\sqrt{2}Ee^{i2\theta}$	0	0
$1/2$	$\sqrt{10}Ee^{-i2\theta}$	0	$\frac{-8}{3}D$	0	$3\sqrt{2}Ee^{i2\theta}$	0
$-1/2$	0	$3\sqrt{2}Ee^{-i2\theta}$	0	$\frac{-8}{3}D$	0	$\sqrt{10}Ee^{i2\theta}$
$-3/2$	0	0	$3\sqrt{2}Ee^{-i2\theta}$	0	$\frac{-2}{3}D$	0
$-5/2$	0	0	0	$\sqrt{10}Ee^{-i2\theta}$	0	$\frac{10}{3}D$

(5.16)

We can follow a similar procedure for the total Zeeman Hamiltonian Hz'. In a co-ordinate frame congruent with the principle axis system of this Hamiltonian can be written as

$$H'_z = \begin{bmatrix} H_x & H_y & H_z \end{bmatrix} \begin{bmatrix} \gamma_x & 0 & 0 \\ 0 & \gamma_y & 0 \\ 0 & 0 & \gamma_z \end{bmatrix} \begin{bmatrix} I_x \\ I_y \\ I_z \end{bmatrix} \qquad (5.17)$$

This matrix equation can then be rotated about the z-axis by the angle ω so that its x-axis coincides with the C3 axis of the crystal. $H'z$ then has the form

$$H'_z = uI^+ + vI^- + g_z H_z I_z \qquad (5.18)$$

where

$$u = \frac{|H|\sin\tau}{4}\left[(\gamma_x + \gamma_y)e^{-i\alpha} + (\gamma_x - \gamma_y)e^{i(2\omega+\alpha)}\right],$$

$$v = u^*,$$

and the external magnetic field, which is at an angle of τ from the C_2 axis and whose projection into the plane perpendicular to C_2 makes an angle α from C_3, is given by

$$\tilde{H} = |H|\,(\sin\tau\cos\alpha,\ \sin\tau\sin\alpha,\ \cos\tau). \qquad (5.19)$$

H_z has the matrix form,
$H_z =$

I_z / I_z	$5/2$	$3/2$	$1/2$	$-1/2$	$-3/2$	$-5/2$
$5/2$	$\frac{-5}{2}\gamma_z H\cos\tau$	$\frac{-\sqrt{5}}{2}u$	0	0	0	0
$3/2$	$\frac{-\sqrt{5}}{2}u^*$	$\frac{-3}{2}\gamma_z H\cos\tau$	$-\sqrt{2}u$	0	0	0
$1/2$	0	$-\sqrt{2}u^*$	$\frac{-1}{2}\gamma_z H\cos\tau$	$\frac{-3}{2}u$	0	0
$-1/2$	0	0	$\frac{-3}{2}u^*$	$\frac{1}{2}\gamma_z H\cos\tau$	$-\sqrt{2}u$	0
$-3/2$	0	0	0	$-\sqrt{2}u^*$	$\frac{3}{2}\gamma_z H\cos\tau$	$\frac{-\sqrt{5}}{2}u$
$-5/2$	0	0	0	0	$\frac{-\sqrt{5}}{2}u^*$	$\frac{5}{2}\gamma_z H\cos\tau$

(5.20)

Finally when the quadratic Zeeman term, which is independent of I_Z, is written in a co-ordinate system congruent to the principle axis of Λ it has the form,

$$g_J^2\mu_B^2 \mathrm{H}\cdot\Lambda\cdot\mathrm{H} = \frac{g_J\mu_B}{2A_J}\left[H_x, H_y, H_z\right]\begin{bmatrix}(\gamma_x-\gamma_N) & 0 & 0\\ 0 & (\gamma_y-\gamma_N) & 0\\ 0 & 0 & (\gamma_z-\gamma_N)\end{bmatrix}\begin{bmatrix}H_x\\ H_y\\ H_z\end{bmatrix}$$

(5.21)

5.2.3 Hyperfine and Zeeman parameters for $LaF_3:Pr^{3+}$.

The Zeeman and quadrupole parameters for the $^3H_4$ ground state listed below are based on those used by Lukac *et al.* [1989], which are closely related to the values determined by Reddy *et al.* [1983]. For the $^1D_2$ state the parameter values determined by Mitsunaga *et al.* [1985] are used. The parameter values are listed in Table 5.1a and 5.1b. The values of D and E have been expressed in the co-ordinate frame where z // C_2 and x // C_3.

Table 5.1a Zeeman and quadrupole parameters for the $^3H_4$ state.

Parameter		Magnitude	Orientation of principle axes
$\gamma_1/2\pi$		3.45 kHz/G	// C_2
$\gamma_2/2\pi$		10.16 kHz/G	81.4° from C_3
$\gamma_3/2\pi$		4.98 kHz/G	-8.6° from C_3
Quadrupole tensor	D	1858 kHz	// C_2, 81.4° from C_3 and
	E	-2166.5 kHz	-8.6° from C_3

Table 5.1b Zeeman and quadrupole parameters for the $^1D_2$ state.

Parameter		Magnitude	Orientation of principle axes
$\gamma_1/2\pi$		2.2 kHz/G	// C_2
$\gamma_2/2\pi$		3.6 kHz/G	20° from C_3
$\gamma_3/2\pi$		1.9 kHz/G	-70° from C_3
Quadrupole tensor	D	1270 kHz	// C_2, 20° from C_3 and
	E	-308 kHz	-70° from C_3

Figs 5.5a and b show the orientation of the principle axes of H_Q and H_Z for the ground and excited states respectively.

To determine the magnetic coupling between the Pr^{3+} ion and the F nuclei in high magnetic fields it is necessary to know the values of both A_J and A_J`, the hyperfine constants for the ground and excited state for Pr^{3+}. Bleany determined A_J for Pr^{3+} in the ground state to be 1093 MHz using NMR techniques [Bleany 1964]. Macfarlane *et al.* measured the QZS of the $^3H_4 \Rightarrow {}^1D_2$ optical transition for the magnetic field aligned along a number different directions using spectral holeburning. From these measurements and a knowledge of A_J, γ and γ` and using Equation 5.21 they determined the hyperfine constant for the excited state $A_J$` to be 600 ± 50 MHz [MacFarlane *et al.* 1981b].

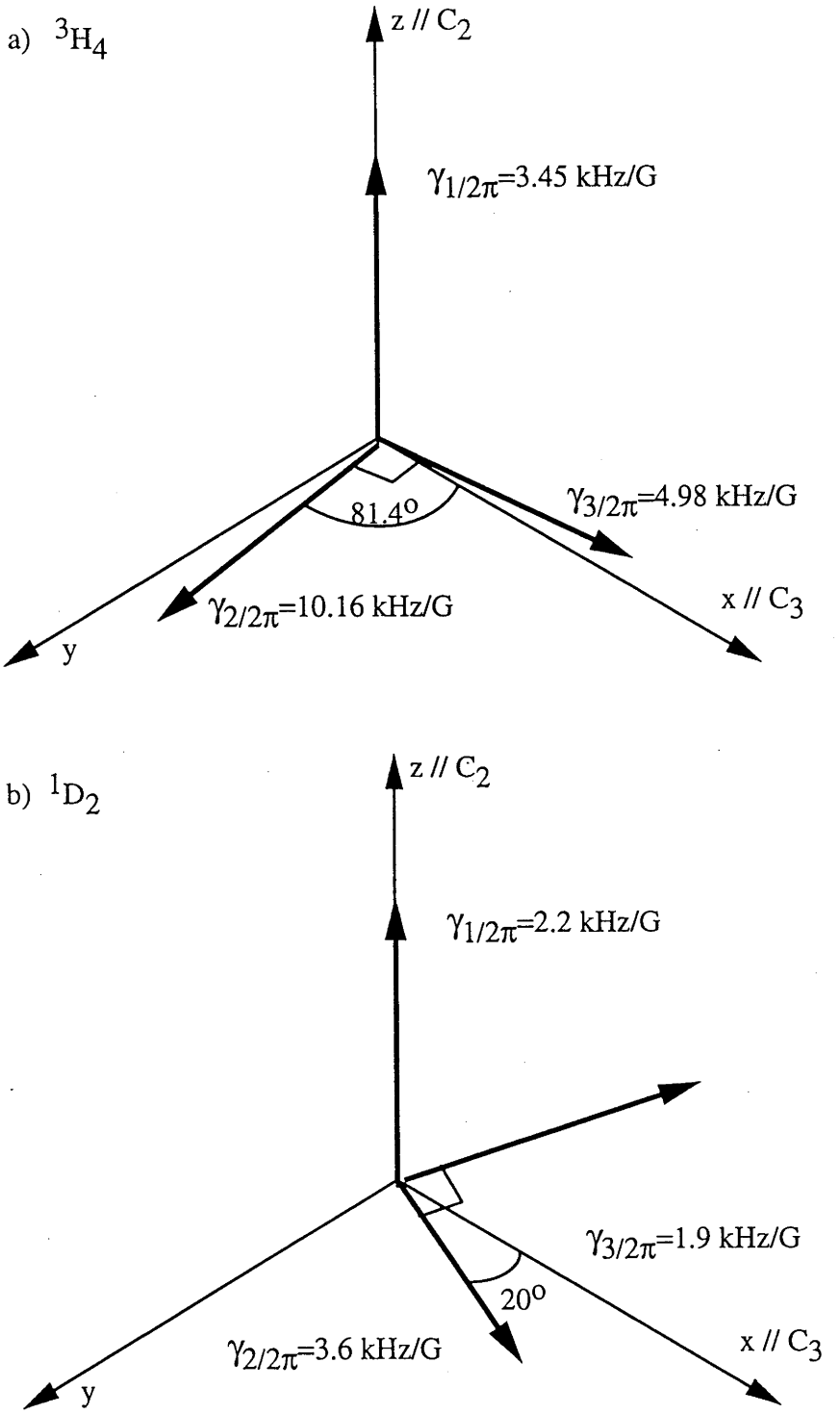

Figure 5.5 a & b. The principle axes of the Zeeman tensor and their relationship to the co-ordinate frame for the $^3H_4(\Gamma_1)$ and $^1D_2(\Gamma_1)$ states.

5.2.4 Theory of super-hyperfine coupling in Pr^{3+}:LaF_3

In this section we will consider the interaction of the enhanced nuclear moment of the Pr^{3+} ion μ_I with the nuclear moment of a single ^{19}F nucleus μ_S. The results from studying this interactions will be used to approximate the behaviour of a Pr^{3+} ion coupled to many ^{19}F nuclei. The calculation will be made for both the $^3H_4$ ground state and the $^1D_2$ excited state to enable the frequency shifts induced by the F spin on the optical transitions to be determined.

The Pr-F nuclear spin system in the presence of an applied magnetic field may be described by the effective Hamiltonian

$$H'_{eff} = H_{Pr} + H_{S-I} - \hbar\gamma_F \tilde{S}\cdot\tilde{\mathbf{H}} \qquad (5.22)$$

where H_{Pr} is the effective Hamiltonian describing the uncoupled Pr^{3+} ion, including the quadrupole and second order magnetic hyperfine interactions given in Equation 5.1, $\gamma_F/2\pi = 4$ kHz/G, and H_{S-I} describes the Pr-F coupling. In the point dipole approximation H_{S-I} is given by

$$H_{S-I} = \frac{\tilde{\mu}_I\cdot\tilde{\mu}_S}{r^3} - \frac{3(\tilde{\mu}_I\cdot\tilde{r})(\tilde{\mu}_S\cdot\tilde{r})}{r^5} \qquad (5.23)$$

where $\tilde{r}$ is the vector joining the Pr and ^{19}F nuclei. On substituting $\mu_I = \hbar\tilde{\gamma}_{Pr}\cdot I$ and $\mu_S = \hbar\gamma_F \cdot S$ into Equation 5.23 and selecting the usual reference frame with z parallel to the C_2 axis and x parallel to the C_3 axis we obtain

$$H_{I-S} = AS_+I_+ + BS_+I_- + CS_-I_+ + DS_-I_- + ES_-I_z + FS_+I_z + GS_zI_- + KS_zI_+ + LS_zI_z, \quad (5.24)$$

where $S_\pm = S_x \pm iS_y/2$, $I_\pm = I_x \pm iI_y/2$ and

$$A = \frac{h^2\gamma_F}{4|r|^3}\left(-\tfrac{1}{2}\exp(i2\omega)(\gamma_x-\gamma_y)(1-3(\cos^2(\theta))-\tfrac{3}{2}\sin^2(\theta)(\gamma_x-\gamma_y)\exp(-i2\eta)\right)$$

$$B = \frac{h^2\gamma_F}{4|r|^3}\left(-\tfrac{1}{2}(\gamma_x+\gamma_y)(1-3(\cos^2(\theta))-\tfrac{3}{2}\sin^2(\theta)(\gamma_x-\gamma_y)\exp(-i2(\eta+\omega))\right)$$

$$L = \frac{h^2\gamma_F}{4|r|^3}\left(2\gamma_x(1-3(\cos^2(\theta))\right)$$

$$K = \frac{h^2\gamma_F}{4|r|^3}\left(\tfrac{3}{2}\sin(\theta)\cos(\theta)(\gamma_x+\gamma_y)\exp(-i\eta)+(\gamma_x-\gamma_y)\exp(i(\eta+2\omega))\right),$$

$$C = B^*$$

$$D = A^*,$$

$$E = F^*$$

$$G = K^*$$

where $\tilde{r} = r(\sin\theta\cos\eta, \sin\theta\sin\eta, \cos\theta)$ and ω is the angle between the principle axis, perpendicular to the C_2 axis, of the tensor γ_{Pr} and the C_3 axis of the crystal.

Writing this in the product basis states $|I_z, S_z\rangle$ the Hamiltonian has the matrix form of

H_{Pr-F} =

	5/2↑	3/2↑	1/2↑	−1/2↑	−3/2↑	−5/2↑	5/2↓	3/2↓	1/2↓	−1/2↓	−3/2↓	−5/2↓
5/2↑	$\frac{5}{2}L$	$\sqrt{5}K$	0	0	0	0	$\frac{5}{2}F$	$\sqrt{5}A$	0	0	0	0
3/2↑	$\sqrt{5}K^*$	$\frac{3}{2}L$	$2\sqrt{2}K$	0	0	0	$\sqrt{5}B$	$\frac{3}{2}F$	$2\sqrt{2}A$	0	0	0
1/2↑	0	$2\sqrt{2}K^*$	$\frac{1}{2}L$	$3K$	0	0	0	$2\sqrt{2}B$	$\frac{1}{2}F$	$3A$	0	0
−1/2↑	0	0	$3K^*$	$-\frac{1}{2}L$	$2\sqrt{2}K$	0	0	0	$3B$	$-\frac{1}{2}F$	$2\sqrt{2}A$	0
−3/2↑	0	0	0	$2\sqrt{2}K^*$	$-\frac{3}{2}L$	$\sqrt{5}K$	0	0	0	$2\sqrt{2}B$	$-\frac{3}{2}F$	$\sqrt{5}A$
−5/2↑	0	0	0	0	$\sqrt{5}K^*$	$-\frac{5}{2}L$	0	0	0	0	$\sqrt{5}B$	$-\frac{5}{2}F$
5/2↓	$\frac{5}{2}F^*$	$\sqrt{5}B^*$	0	0	0	0	$-\frac{5}{2}L$	$-\sqrt{5}K$	0	0	0	0
3/2↓	$\sqrt{5}A^*$	$\frac{3}{2}F^*$	$2\sqrt{2}B^*$	0	0	0	$-\sqrt{5}K^*$	$-\frac{3}{2}L$	$-2\sqrt{2}K$	0	0	0
1/2↓	0	$2\sqrt{2}A^*$	$\frac{1}{2}F^*$	$3B^*$	0	0	0	$-2\sqrt{2}K^*$	$-\frac{1}{2}L$	$-3K$	0	0
−1/2↓	0	0	$3A^*$	$-\frac{1}{2}F^*$	$2\sqrt{2}B^*$	0	0	0	$-3K^*$	$\frac{1}{2}L$	$-2\sqrt{2}K$	0
−3/2↓	0	0	0	$2\sqrt{2}A^*$	$-\frac{3}{2}F^*$	$\sqrt{5}B^*$	0	0	0	$-2\sqrt{2}K^*$	$\frac{3}{2}L$	$-\sqrt{5}K$
−5/2↓	0	0	0	0	$\sqrt{5}A^*$	$-\frac{5}{2}F^*$	0	0	0	0	$-\sqrt{5}K^*$	$\frac{5}{2}L$

(5.25)

The arrows indicate the direction of the ^{19}F nuclear spin.

5.2.5 Fluorine positions

The vector $\tilde{r}$ joining the Pr and the F nuclear positions can be calculated from crystallographic positional parameters for LaF_3 determined by Mansmann [1965]. For convenience the position in the unit cell of each ion and the positional parameters are reproduced in Table 5.2 Fig 5.6 shows the ninefold coordination of the La^{3+} site in LaF_3.

5.2.6 Calculation of Frequency Shifts and Transition Probabilities.

The wavefunctions of the ground and excited states including the superhyperfine interaction can be written as a product state of the eigenfunctions of the first two terms in Equation 5.1, the free ion and crystal field Hamiltonian, with the eigenfunctions of $H_{eff}^{'}$. the Hamiltonian given in Equation 5.22. The relative transition probability of the optical transitions between different hyperfine and superhyperfine levels of the ground and excited states is given by the inner product of the eigenstates of the $H_{eff}^{'}$. The frequency of all these transitions are determined to within an additive constant by the eigenvalues of $H_{eff}^{'}$.

As an example the four transitions between I=-5/2 $^3H_4$ and I=-5/2 $^1D_2$ Pr^{3+} states interacting with a single F nuclei spin (for an external magnetic field of 50 G applied along the C_3 axis) are illustrated in Fig 5.7. The interaction strengths and frequency shifts were calculated for a ^{19}F nucleus at a distance of 0.247 nm from the Pr nucleus 69 degrees from the C_2 axis and 57 degrees from the C_3 axis. The position of this F ion is indicated in Fig 5.6. The two strong transitions indicated in Fig 5.7 are where the spin of the ^{19}F nucleus is left unchanged. The weaker transitions present are where the spin of the ^{19}F nucleus does flip, and are allowed because of the difference in the enhanced nuclear moment of the Pr^{3+} ion between the ground and excited states. This difference in the enhanced moments also results in a frequency difference between the two strongly allowed transitions. In the case illustrated in Fig 5.7 the frequency difference is 23 kHz.

The two transitions where the F spin is flipped were calculated to each have 3.5% of the total oscillator strength of the I=-5/2 $^3H_4$ to I=-5/2 $^1D_2$ transition. The oscillator strength of these F spin-flip transitions decreases inversely with an increasing applied magnetic field for fields greater than 10 G. This is because the perturbation in the local magnetic

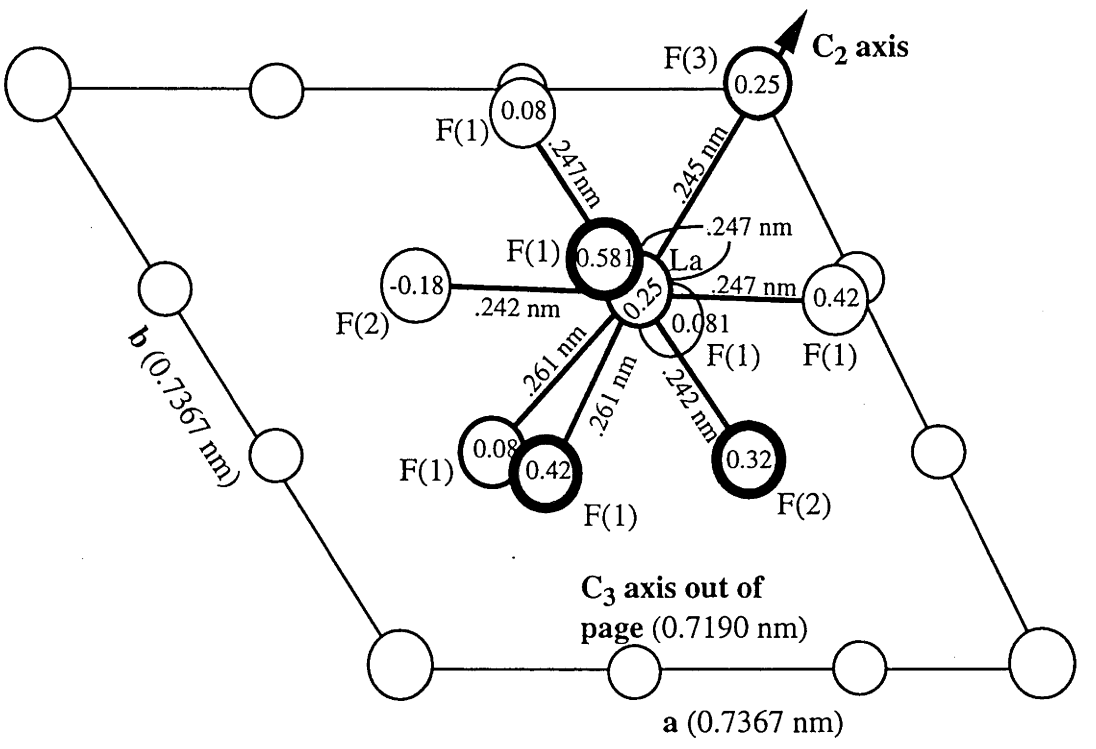

Figure 5.6. The ninefold co-ordination diagram of La in LaF_3 as viewed down the C_3 axis. The separations shown were determined using the positional parameters given in Table 5.2.

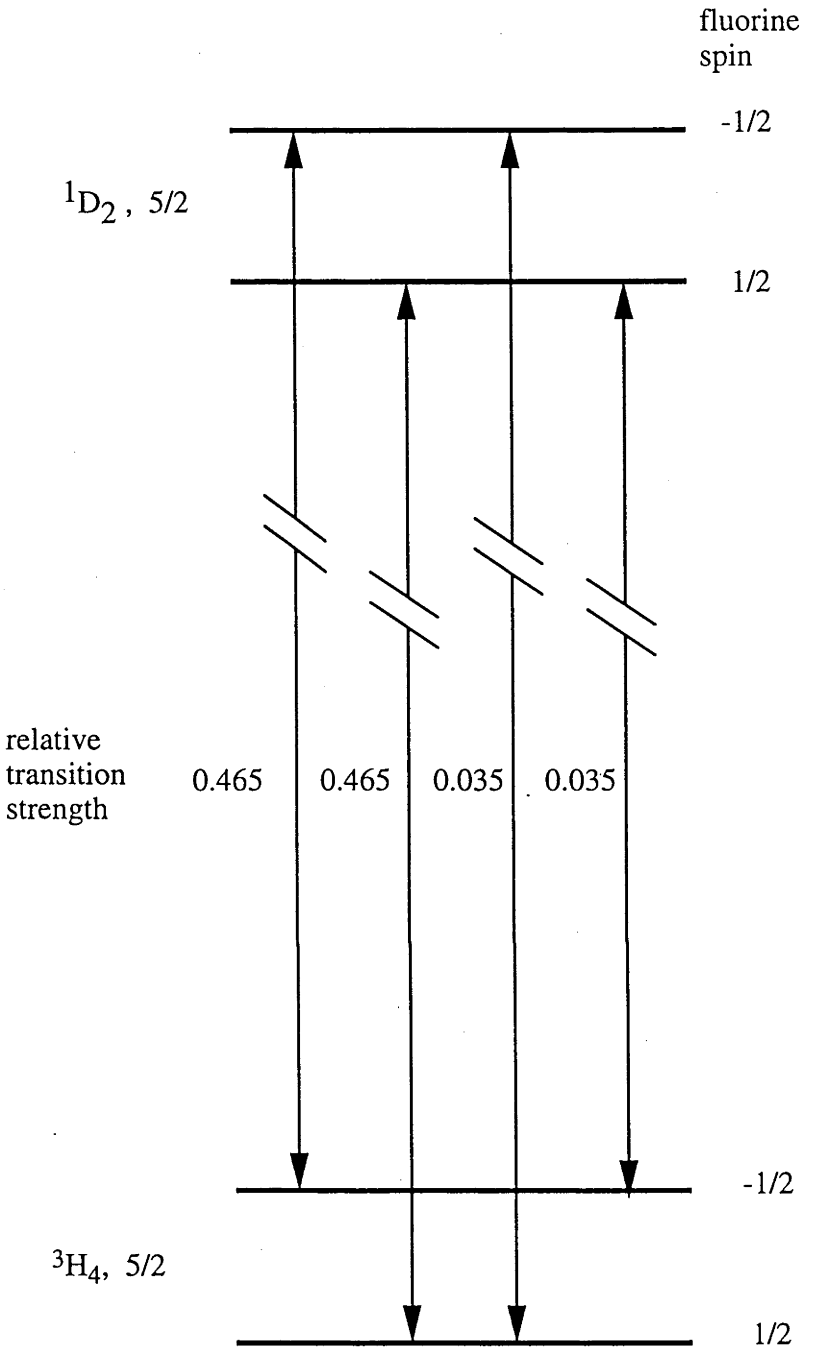

Figure 5.7. Transitions between the I=5/2 $^3H_4$ and I=5/2 $^1D_2$ states for the Pr-F coupled system in the presence of a 50 G field. The particular ^{19}F nucleus used in this example is separated by 0.247 nm from the Pr nucleus, 69° from the C_2 axis and 57° from the C_3 axis.

field seen by the ^{19}F nucleus due to the Pr^{3+} ion changing state becomes less significant compared to the total field as the applied field is increased.

To be able to relate this theoretical oscillator strength of the F spin flip transition to experiment it is necessary to calculate the probability of flipping a ^{19}F nucleus without being able to distinguish which F nuclei flipped. This was estimated by calculating the oscillator strength of flipping each of the 9 N-N ^{19}F nuclei separately, using the single ^{19}F nucleus model, and then summing the nine values. Table 5.3 gives the relative strength of the F spin-flip transitions for all 36 transitions between the hyperfine levels of the ground and excited states, in the presence of a 50 G field along the C_3 axis. The oscillator strengths of the transitions have been halved to take account of the 50:50 population distribution of the F spin states.

Ground state Hyperfine Levels	Excited State Hyperfine Levels					
	$5/2$	$3/2$	$1/2$	$-1/2$	$-3/2$	$-5/2$
$5/2$	(0.061,0.059)	(0.062,0.070)	(0.248,0.018)	(0.063,0.018)	(0.150,0.014)	(0.085,0.005)
$3/2$	(0.012,0.022)	(0.95,0.006)	(0.013,0.065)	(0.32,0.017)	(0.003,0.052)	(0.283,0.017)
$1/2$	(0.017,0.066)	(0.008,0.021)	(0.075,0.077)	(0.008,0.013)	(0.108,0.002)	(0.070,0.000)
$-1/2$	(0.017,0.001)	(0.033,0.001)	(0.004,0.083)	(0.033,0.069)	(0.007,0.020)	(0.014,0.061)
$-3/2$	(0.014,0.011)	(0.019,0.053)	(0.020,0.068)	(0.024,0.050)	(0.054,0.004)	(0.025,0.030)
$-5/2$	(0.066,0.006)	(0.058,0.018)	(0.060,0.017)	(0.24,0.000)	(0.073,0.070)	(0.063,0.055)

Table 5.3 Relative intensity of the optical F spin flip transition. The first figure in the brackets gives the ratio of the strength of the F spin flip component of the total oscillator strength between the two hyperfine levels. The second figure gives the ratio of the oscillator strength between the the two hyperfine levels and the total oscillator strength between the $^3H_4$ and $^1D_2$ states.

5.2.7 Calculation of the optical magnetic inhomogeneous broadening.

The inhomogeneous broadening of an optical transition due to different random orientations of the F spins can be estimated from the frequency shifts calculated for each ^{19}F nuclear position. When the applied magnetic field dominates the local field due to the ^{19}F spins it is valid to assume that the frequency shifts induced by each F spin on the optical transition calculated using the single ^{19}F nucleus model can be simply added to give the combined effect. The frequency of the optical transition for a given Pr^{3+} site is of the form

$$\nu = \nu_0 + \sum_i (-1)^r f_i , \qquad (5.26)$$

where the sum is over the ^{19}F positions, f_i is the frequency shift induced by the i^{th} ^{19}F nuclear magnetic moment, r is a random integer and υ_0 is the unperturbed optical frequency. The profile of the broadened line can then be built up by calculating ν for many different random distribution of the F spins. Fig 5.8 shows the distribution of F nuclei vs the frequency shift induced in the 5/2 $^3H_4$ to 5/2 $^1D_2$ optical transition by each F moment. The magnetic inhomogeneous profile of the I=5/2 $^3H_4$ to I=5/2 $^1D_2$ transition in a magnetic field of 100 G // C3, shown in Fig 5.9, was obtained using Equation 5.29 and 10000 random distributions of the nearest 250 ^{19}F nuclei. The profile was found not to change significantly when the number of ^{19}F nuclei was reduced to 50 or increased to 1000, indicating that 250 is a sufficient number of ^{19}F nuclei to consider when calculating the linewidths. Table 5.4 contains the FWHM linewidths of the 36 optical transitions calculated for the same parameters used to generate Fig 5.10. As an estimate of the holewidth a weighted mean of the 36 transition linewidths was performed using the relative oscillator strengths given in Table 5.4. The value for the holewidth calculated using this method was 77 kHz.

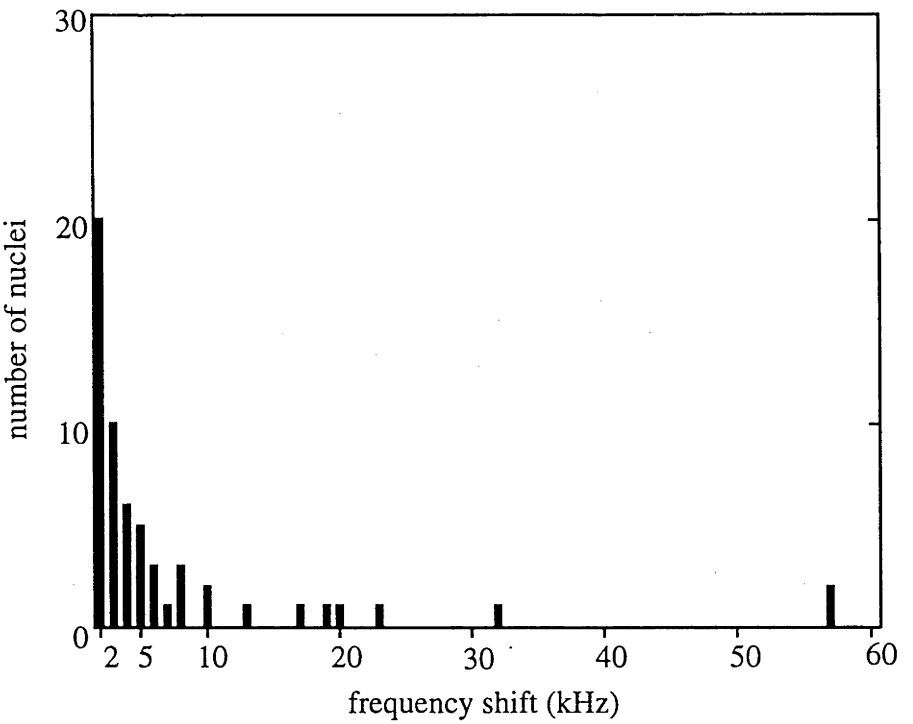

Figure 5.8. Distribution of the ^{19}F nuclei as a function of the frequency shift their moments induce on the I=5/2 $^3H_4$ to I=5/2 $^1D_2$ optical transition. The distribution is for the 250 ^{19}F nuclei closest to the Pr^{3+} ion.

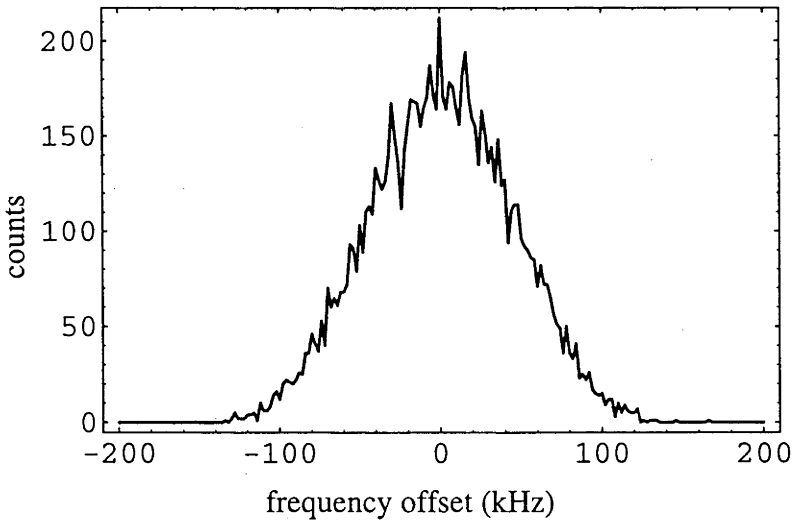

Figure 5.9 Magnetically inhomogeneously broadened profile of the I=5/2 $^4H_3(\Gamma_1) \Rightarrow$ I=5/2 $^1D_2(\Gamma_1)$ transition calculated using Equation 5.26 and 10000 random distributions of the moments of the nearest 250 ^{19}F nuclei. The vertical axis gives the number of distributions having a frequency in a given 2 kHz window.

Ground state Hyperfine Levels	Excited state Hyperfine Levels					
	$5/2$	$3/2$	$1/2$	$-1/2$	$-3/2$	$-5/2$
$5/2$	99*kHz*	97*kHz*	106*kHz*	105*kHz*	111*kHz*	128*kHz*
$3/2$	56*kHz*	53*kHz*	53*kHz*	51*kHz*	60*kHz*	87*kHz*
$1/2$	18*kHz*	37*kHz*	53*kHz*	53*kHz*	75*kHz*	99*kHz*
$-1/2$	85*kHz*	57*kHz*	47*kHz*	48*kHz*	24*kHz*	14*kHz*
$-3/2$	93*kHz*	74*kHz*	60*kHz*	55*kHz*	47*kHz*	52*kHz*
$-5/2$	115*kHz*	106*kHz*	105*kHz*	102*kHz*	95*kHz*	90*kHz*

Table 5.4a. Predicted FWHM linewidths of the optical transitions between the $^3H_4$ levels hyperfine and the $^1D_2$ hyperfine levels, in the presence of an applied field of 100 G parallel to the C_3 axis.

Ground state Hyperfine Levels	Excited state Hyperfine Levels					
	$5/2$	$3/2$	$1/2$	$-1/2$	$-3/2$	$-5/2$
$5/2$	0.061	0.069	0.000	0.018	0.012	0.058
$3/2$	0.019	0.003	0.052	0.016	0.058	0.017
$1/2$	0.067	0.021	0.012	0.063	0.003	0.000
$-1/2$	0.001	0.000	0.073	0.014	0.019	0.059
$-3/2$	0.0093	0.053	0.019	0.048	0.005	0.033
$-5/2$	0.073	0.020	0.016	0.000	0.068	0.053

Table 5.4b. The ratio of the oscillator strength between particular hyperfine levels to the total oscillator strength between the $^3H_4$ and $^1D_2$ states, in the presence of an applied field of 100 G parallel to the C_3 axis

5.2.8 Calculation of broadening in the hyperfine transitions.

So as to be able to test the validity of the calculation of the magnetic inhomogeneous broadening of the optical transitions, the widths of the NMR transitions in both the ground and the excited states have also been calculated. The procedure used to calculate the line profiles is identical to that used for the optical transitions. An external field of 100 G//C_3 was assumed. The linewidths are presented in Table 5.5, along with the experimental values of Wong *et al.*, obtained with the use of a Raman heterodyne detection technique on a 0.1 at% $LaF_3:Pr^{3+}$ sample [Wong *et al.* 1983].

	Transition	*Theory (kHz)*[a]	*Experimental (kHz)*
$^3H_4$	$\frac{1}{2} \rightarrow \frac{3}{2}$	80	159 ± 5^b
	$\frac{3}{2} \rightarrow \frac{5}{2}$	52	160.5 ± 1^b
$^1D_2$	$\frac{1}{2} \rightarrow \frac{3}{2}$	24	32 ± 3^b 15 ± 2^c
	$\frac{3}{2} \rightarrow \frac{5}{2}$	35	33 ± 3^b 21 ± 2^c

Table 5.5. Inhomogeneous and homogeneous linewidths (FWHM) for the hyperfine transitions of the $^3H_4$ ground and $^1D_2$ excited states.

[a] *Theoretical values calculated for an applied field of 100 G parallel to the C_3 axis.*

[b] *Wong 1983, CW measurement made in the presence of the earth's magnetic field. In an applied DC magnetic field of 30 -150 G, the $^3H_4$ ground state inhomogeneous widths were observed to narrow from zero-field values of 160 kHz to approximately 100 kHz. It is not clear if a similar narrowing was observed for the $^1D_2$ widths.*

[c] *Wong et al. 1983, Spin echo measurements of the homogeneous linewidths in an applied field of 30 G perpendicular to the C_3.*

The theoretical values for the $^3H_4$ linewidths of 52 and 80 kHz are significantly smaller (up to a factor of 2) than the experimental values of approximately 100 kHz (see (b)). The difference could be due to strain broadening of the hyperfine transitions. Another

possibility is that the interaction between the Pr^{3+} enhanced nuclear moment and the moment of the N-N ^{19}F nuclei has a contribution from an exchange interaction. They are neighbouring nuclei and hence an exchange effect via their respective electron clouds is possible.

A direct comparison between theoretical and the experiment values for the $^1D_2$ hyperfine transitions is not possible without further experiments measuring the inhomogeneous linewidths of these transitions in the presence of a magnetic field are performed. On the available data, though, there seems to be a reasonable agreement.

5.2.9 Chemical shift

In this section the chemical shift of the F nuclear magnetic moment due the interaction with the electronic part of the Pr^{3+} ion's wavefunction will be calculated for both the $^3H_4$ and $^1D_2$ levels.

When an external field is applied to the Pr^{3+} ion a magnetic dipole moment is induced in the electronic part of the wavefunction. This moment is associated with both the quadratic Zeeman and the enhanced nuclear Zeeman effects. This moment is given by

$$\tilde{\mu}_H = 2g_J^2\mu_B^2 H\, \Lambda_{Pr} \qquad (5.27)$$

This magnetic moment will also interact with the nuclear magnetic moments of the F nuclei. The general form of the interaction Hamiltonian,

$$H_{chem} = \gamma_F(2g_J^2\mu_B^2 H\, \Lambda_{Pr})\cdot \Delta\mathbf{S} \qquad (5.28)$$

is the same as the nuclear Zeeman effect. The other way to think of this interaction is that the fluorine nuclear magnetic moment induces a moment on the Pr electronic states, which causes a chemical shift in the fluorine's magnetic moment equal to

$$\gamma_F(2g_J^2\mu_B^2\Lambda_{Pr})\cdot \Delta\mathbf{S} \qquad (5.29)$$

This interaction is independent of the Pr hyperfine state so it will not affect the inhomogeneous broadening of the hyperfine transitions. This interaction though will affect the detuning of the N-N F spins from the bulk F and hence will alter the dynamics of the N-N F. Furthermore because this interaction depends on the electronic state of the Pr^{3+} ion it will contribute to the broadening in the optical transition.

It will be assumed here that the interaction between the F moment and the induced moment is purely dipolar. This assumption is justified on the grounds of the reasonable success of the same assumption in determining the inhomogeneous linewidths of the rf transitions (see Section 5.). The interaction can now be written as

$$H_{chem} = \frac{\tilde{\mu}_H \tilde{\mu}_S}{r^3} - \frac{3(\tilde{\mu}_H \cdot \tilde{r})(\tilde{\mu}_S \cdot \tilde{r})}{r^5} \qquad (5.30)$$

For simplicity we will only calculate this chemical shift for an external field along the C_3 axis of the crystal. All the experiments where the chemical shift is of concern were performed with the field along this axis. From Equations 5.27 and 5.30 the induced magnetic moment written in a co-ordinate frame aligned along the C_2 and C_3 axis is given by

$$\mu_I = \frac{g_J \mu_B \tilde{H}}{A_J} \times \begin{bmatrix} (\gamma_x - \gamma_n)\cos^2\theta + (\gamma_y - \gamma_n)\sin^2\theta & (\gamma_x - \gamma_n)\sin\theta\cos\theta & 0 \\ (\gamma_y - \gamma_n)\sin\theta\cos\theta & (\gamma_x - \gamma_n)\cos^2\theta + (\gamma_y - \gamma_n)\sin^2\theta & 0 \\ 0 & 0 & \gamma_z \end{bmatrix} \qquad (5.31)$$

For a field applied along the C_3 axis the magnitude of the induced magnetic moment in the groundstate calculated using Equation 5.31 is

$$\mu_I = 4.22 \times |H| \ \ Hz/G^2 \qquad (5.32)$$

For the excited state the induced moment is

$$\mu_I = 5.44 \times |H| \ \ Hz/G^2 \qquad (5.33)$$

The magnitude of the difference in the induced moments of the ground and excited states is

$$\mu_I = 1.20 \times |H| \ \ Hz/G^2 \qquad (5.34)$$

For the field applied along the C_3 axis the Equation 5.30, describing the interaction of the induced moment with the F moment, can be written in matrix form as

$$H_c = \frac{h\gamma_F g_J \mu_B H_x}{2A_J r^3} \times$$

$$\left(\left[\begin{bmatrix} 0 & \begin{pmatrix} (\gamma_x - \gamma_n)\cos^2\theta + (\gamma_y - \gamma_n)\sin^2\theta \\ -i(\gamma_y - \gamma_x)\sin\theta\cos\theta \end{pmatrix} \\ \begin{pmatrix} (\gamma_x - \gamma_n)\cos^2\theta + (\gamma_y - \gamma_n)\sin^2\theta \\ -i(\gamma_y - \gamma_x)\sin\theta\cos\theta \end{pmatrix} & 0 \end{bmatrix} - \right.$$

$$\left. -3(\sin\theta_r \cos\phi((\gamma_x - \gamma_n)\cos^2\theta + (\gamma_y - \gamma_n)\sin^2\theta)) + \sin\theta_r \sin\phi(\gamma_y - \gamma_x)\sin\theta\cos\theta) \times \begin{bmatrix} \cos\theta_r & \sin(\theta_r)e^{-i\phi} \\ \sin(\theta_r)e^{-i\phi} & \cos\theta_r \end{bmatrix} \right) \tag{5.35}$$

The Hamiltonian has been written using the eigenstates of the ^{19}F spin $|S_z\rangle$ as the basis states.

For a large external magnetic field applied along the C3 axis, to a good approximation, the energy shifts in the optical transitions due to the F spins can be determined by simply solving 5.34 for both the electronic ground and excited state, for each F position. In a procedure identical to that used in Section 5.2.7, these values can be used to estimate the linewidth of the transition. Using the energy shifts of the nearest 250 F spins the FWHM linewidth was found to be 12 Hz/G times the applied field for fields greater than about 10 kG. For fields below this the chemical shift no longer dominates the Pr-F interaction and the full effective Hamiltonain must be solved.

5.2.10 Pr - Pr cross relaxation

As discussed in Section 5.1 the cross-relaxation between groundstate hyperfine levels induced by the Pr - Pr dipolar interaction provide a mechanism for both filling and broadening the spectral hole. In this section the Pr-Pr cross-relaxation rate will be estimated as a function of the detuning of their hyperfine transitions. The effect the dynamics of the ^{19}F nuclear spin has on the cross-relaxation rate will be considered.

Bloembergen *et al.* considered the cross relaxation of two nuclear spins in 1959 [Bloembergen *et al.* 1959]. They showed that if the homogeneous line profiles of the rf transitions between the spin states are assumed Gaussian then the probability per unit time that ion 1 increases its energy by $h\upsilon_1$ and ion 2 decreases its energy by $h\upsilon_2$ with the

balance of the energy taken up by the whole array of dipoles (in the case of $LaF_3 : Pr^{3+}$ the F magnetic moments outside of the frozen core) can be estimated by

$$w_{ij} = \frac{|\langle\varphi_i|H_{int}|\varphi_f\rangle|^2}{\sqrt{2\pi}\hbar^2}\left[\frac{\exp\left\{\frac{-(\nu_1-\nu_2)^2}{2[(\Delta\nu_1)^2+(\Delta\nu_2)^2]}\right\}}{\sqrt{[(\Delta\nu_1)^2+(\Delta\nu_2)^2]}}\right] \qquad (5.36)$$

where H_{int} is the interaction Hamiltonian ,υ_1 and υ_2 are the transition frequencies and $\Delta\upsilon_1$ and $\Delta\upsilon_2$ are the FWHM homogeneous linewidths of the rf transition under consideration for each ion.

The term in the truncated dipolar interaction Hamiltonian (Equation 5.24) which describes the cross-relaxation process in the presence of an external field significantly greater than the dipolar interaction, is given by

$$H_{int} = \frac{\gamma^2\hbar^2}{4r^3}(1 - 3\cos^2\theta)(\mathbf{I}_1^+\mathbf{I}_2^- + \mathbf{I}_1^-\mathbf{I}_2^+) \qquad (5.37)$$

where r is the separation between the ions, θ is the angle between the two moments and γ is the enhanced nuclear moment of the Pr^{3+} ion. To obtain an estimate of the cross-relaxation rate it will be assumed that γ_{Pr} is isotropic and has a value of 6 kHz (the average of the 3 principal axes values). For our dipolar interaction

$$|\langle\varphi_f|H_{int}|\varphi_f\rangle|^2 = [I_1(I_1+1) - m_1(m_1+1)][I_2(I_2+1) - m_2(m_2+1)] \qquad (5.38)$$
$$\times \frac{\gamma^4\hbar^4}{16r^6}(1 - 3\cos^2\theta)^2$$

For a sample of $LaF_3:Pr^{3+}$ with 0.1 at% Pr, assuming the ions are evenly distributed throughout the crystal, the most common separation of a Pr^{3+} ion from its nearest Pr^{3+} neighbour is 1.1 nm.

The dynamics of the Pr - Pr cross-relaxations is complicated by the presence of the F frozen core that surrounds the Pr^{3+} ions. The complication arises because the broadening of the Pr^{3+} hyperfine transitions due to the N-N ^{19}F nuclei cannot be necessarily treated as either pure homogeneous or pure inhomogeneous broadening. It is shown below that the F spin flips within the frozen core may be a bottleneck for the Pr-Pr cross-relaxation process. Figure 5.10 shows the estimated cross-relaxation rate for the $^3H_4$ ($3/2 \Rightarrow 5/2$) as a function of the detuning between the two ions calculated using

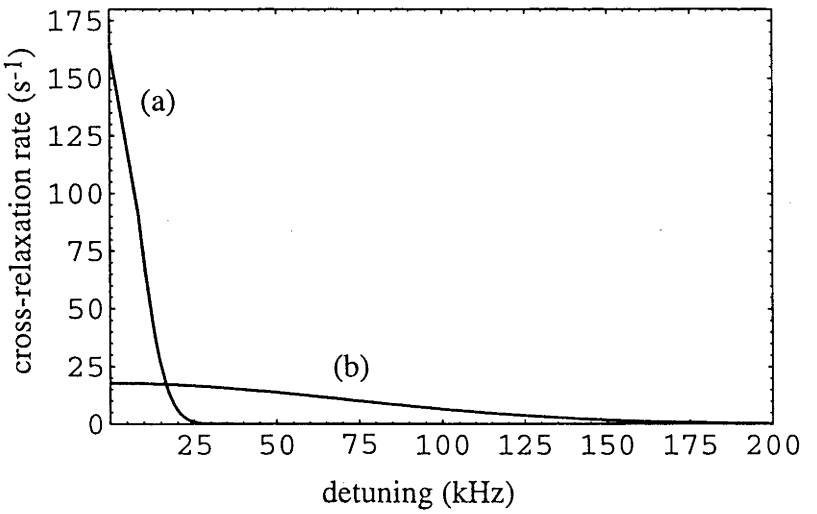

Figure 5.10. The cross-relaxation rate between two Pr^{3+} ions in LaF_3:Pr^{3+}, one in the I=3/2 groundstate hyperfine level and the other in the I=5/2 level, calculated using Equation 5.36. The rate is shown as a function of the detuning of the I=3/2 $\Rightarrow$ 5/2 hyperfine transition between the two ions. For trace (a) $2\,\Delta\upsilon$ = 11 kHz and for trace (b) $2\,\Delta\upsilon$ = 100 kHz.

Equation 5.36, for an ion separation of 1.1 nm. The angle between the two dipole moments was set to 90 degrees. Two traces are plotted in Fig 5.11 in the first $\Delta\upsilon$ was set to 11 kHz, the value of the homogeneous linewidth of the 3/2 $\Rightarrow$ 5/2 transition determined by Wong *et al.*. [Wong *et al.* 1983]. In the second trace $\Delta\upsilon$ was set to 100 kHz, the total linewidth of the 3/2 $\Rightarrow$ 5/2 transition [Wong *et al.* 1983]. To illustrate the effect the N-N ^{19}F nuclear spin flips can have on the Pr-Pr cross-relaxation, consider two Pr^{3+} ions whose hyperfine transitions are detuned by 50 kHz from each other. If the N-N ^{19}F nuclear spins are assumed to be static the cross-relaxation rate as calculated using Equation 5.35 is of the order 10^{-7} Hz. If the N-N ^{19}F nuclear spin flip rate is assumed to be rapid, the broadening due to the N-N 19F's can be treated as homogeneous and the cross-relaxation rate for the ions detuned by 50 Hz is 14 Hz. If the spin flip rate of the N-N ^{19}F nuclei is comparable or slower than 14 Hz the Pr-Pr cross-relaxation rate will be limited by the F spin flip rate. This is because the Pr^{3+} ions will wait for the N-N ^{19}F spin flips to bring them into resonance with each other before they are likely to undergo a cross-relaxation.

It was shown in Section 5.2.9 that increasing the magnetic field will decrease the rate at which the N-N ^{19}F nuclei undergo mutual spin flips. As these spin flips can act as a bottle neck for the Pr-Pr cross-relaxation it is to be expected that the cross-relaxation rate of the Pr3+ ions will also decrease with an increase in the external magnetic field. This slowing down of the cross relaxation should be evident as a decrease in the decay rate of the spectral holes as the external field is increased.

5.3 Experimental Procedure

The measurements were performed on the $^3H_4(\Gamma_1) \Rightarrow {}^2D_1(\Gamma_1)$ transition of the Pr^{3+} ion in a crystal of LaF_3:Pr^{3+} (nominal 0.1 at%) at 2K. The wavelength of this transition is 592.52 nm. The sample was irradiated with light from the modified Coherent 699 ring dye laser described in Chapter 2. The laser beam was aligned along the C_3 axis of the crystal and focused down to a spot size of 200 μm. The photon echo technique described in Chapter 4 was used to determine the homogeneous linewidth of the transition for the current sample. The holeburning measurements were performed with the frequency modulation technique described in Chapter 3. The power in the burn beam was varied from 0.1 mW to 100 mW. The power in the probe beam was typically 1 mW with about 1% of this power in the FM sidebands. Unless otherwise stated the sidebands of the probe beam were swept at a rate of 1 MHz/ms. The scans were recorded as single shot events with a delay of at least 60 seconds between shots.

Two different cryostats were used. Where only low magnetic fields were needed a glass cryostat was used. The sample was immersed in liquid helium, which was pumped to reduce its temperature to below 2 K. The magnetic field was supplied by a set of three orthogonal pairs of superconducting coils. Each pair of coils is capable of supplying a 200 G field. When fields above 200 G were needed an Oxford Instruments cryostat equipped with a superconducting magnet was used. The sample was again immersed in liquid helium and pumped. The crystal was aligned such that the magnetic field was along the C_3 axis of the crystal. The superconducting magnet is capable of generating fields of up to 6 T.

5.4 Results

5.4.1 Side hole structure

The amplitude of the photon echo signal as a function of the pulse separation, in the presence of a 100 G magnetic parallel to the C_3 axis, is shown in Fig. 5.11. The laser power used for these measurements was 100 mW. The echo signal was found to have a maximum amplitude for a $\pi/2$ pulse duration of 2 μs. This suggest that the nutation frequency due to the optical driving field is 125 kHz. The signal was observed to decay exponentially as function of the delay time, with a decay time of 7.55±0.1 μs. From Equation 4.23, T_2 is twice the observed decay time 15.1± 0.2 μs, and the homogeneous linewidth given by $1(\pi T_2)$ is 21± 0.3 kHz. As discussed in Chapter 3 the narrowest possible width of a spectral hole is twice the homogeneous linewidth, which in the present case means a linewidth of 42 ± 0.6 kHz. This value for T2 is shorter than that of Macfarlane et al. [Macfarlane et al. 1979] who get 23 μs at 80 G. This indicates a sample dependence.

Fig 5.12 shows two spectra of optical holes created with 5 mW pulses 200 μs long, one burnt and probed in the absence of an external magnetic field, the other in the presence of a 53 G field along the C_3 axis. The delay between burning the hole, and the sideband scanning through it was approximately 500 μs. The width of the hole burnt with zero applied magnetic field was 220 ± 10 kHz FWHM. On the application of the 53 G field the hole split into three with the holewidth reducing to 80±10 kHz. When the applied magnetic field was increased the frequency of the two side holes was observed to shift at a rate of 4.0±0.2 kHz/G, as shown in Fig 5.13.

As shown in Figs 5.14 and 5.15 the frequency of the side holes were found to be independent of the direction of the applied field, although the frequency of other Zeeman

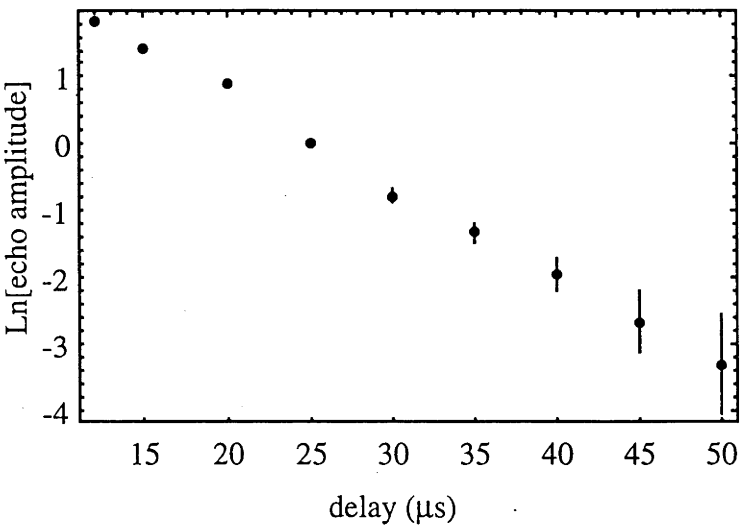

Figure 5.11. Photon echo amplitude as a function of the delay time, for the $^3H_4 \Rightarrow {}^1D_2$ transition in $LaF_3:Pr^{3+}$ in the presence of a 100 G magnetic field parallel to the C_3 axis. The laser intensity was 100 mW and the duration of the $\pi/2$ pulse was 2 μs. The observed decay rate was 7.55 ± 0.05 μs.

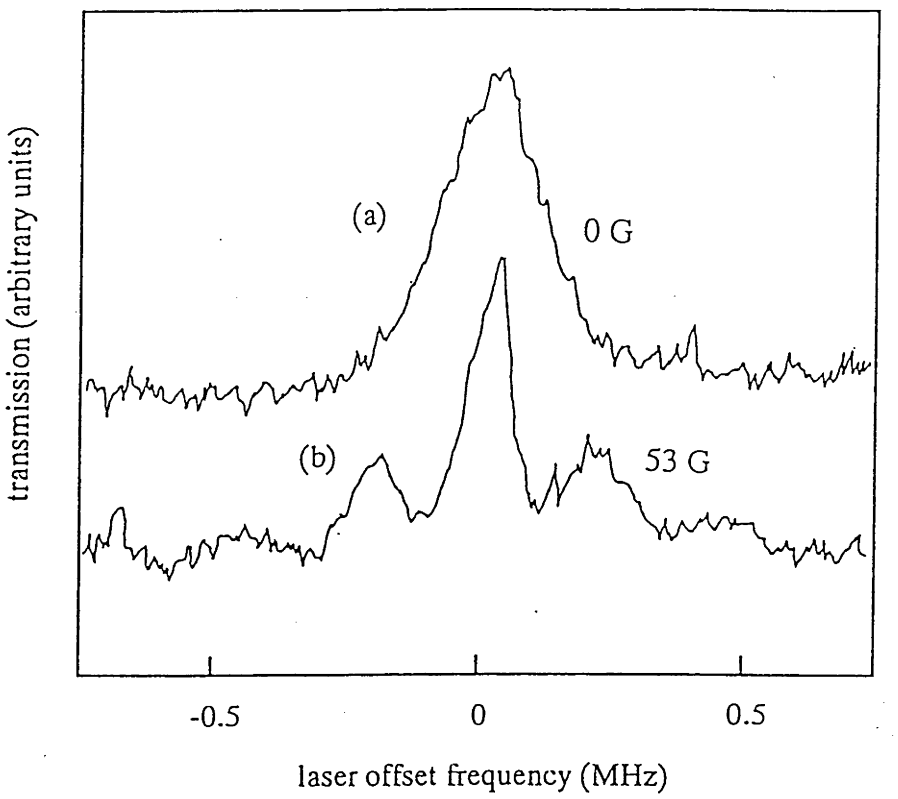

Figure 5.12 Optical holeburning spectra. Trace (a) was taken in the presence of the earth's magnetic field only. Trace (b) was taken in the presence of a 53 G magnetic field parallel to the C_3 axis of the crystal.

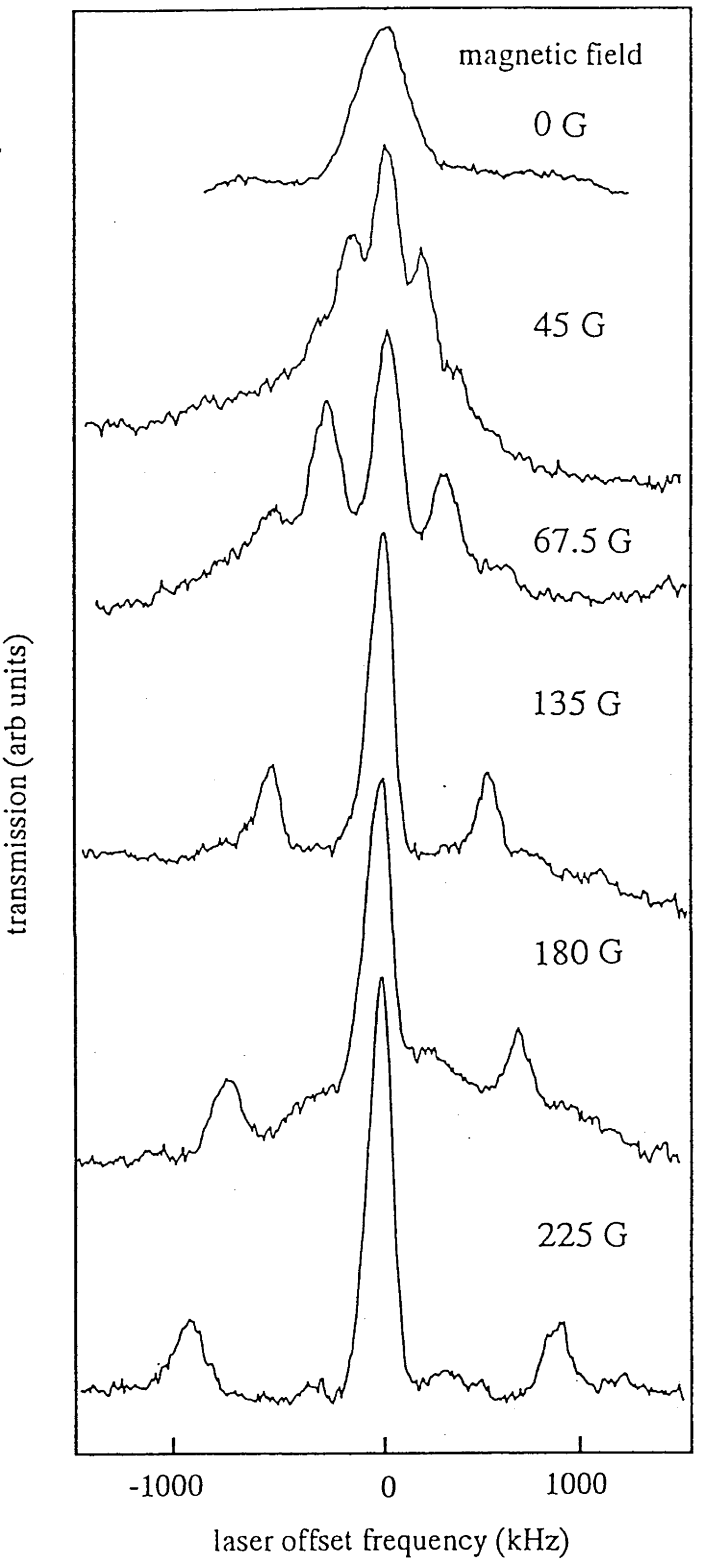

Figure 5.13 Optical holeburing spectra taken in the presence of a magnetc field parallel to the C_3 axis. The magnitude of the field was varied from 0 to 225 G.

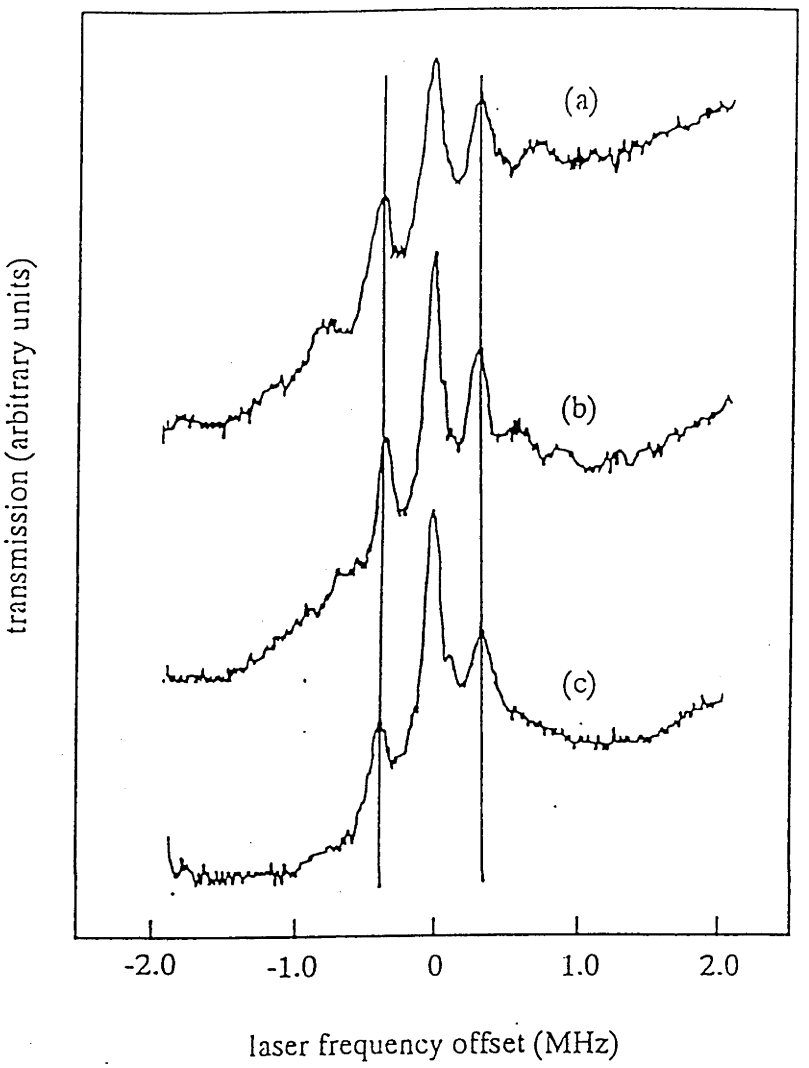

Figure 5.14 Optical hole burning spectra taken in the presence of a 86 G magnetic field in a plane including the C_3 and C_2 axes. For trace (a) the field is parallel to the C_3 axis, trace (b) 45^o to the C_3 axis and for trace (c) the field is parallel to the C_2 axis. For all of the angles sideholes are observed at ± 344 kHz.

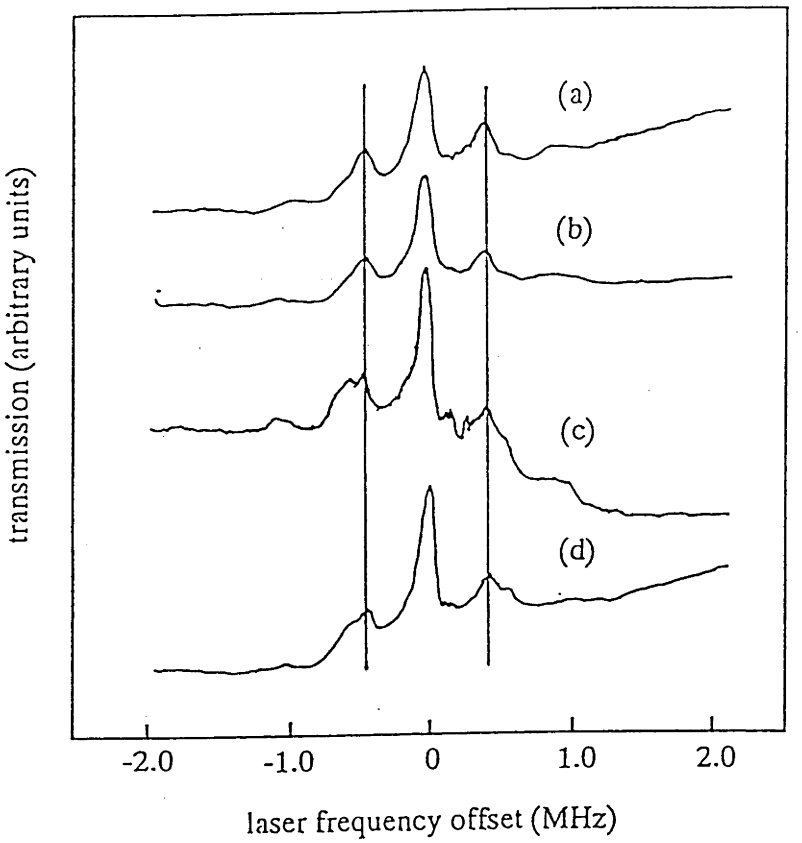

Figure 5.15. Optical hole burning spectra taken in the presence of a 210 G magnetic field perpendicular to the C_3 axis. For trace (a) the field is 15° from one of the C_2 axis trace (b) 30°, trace (c) 45° and for trace (d) 53°. For all angles sideholes are observed at ± 840 kHz.

structure was observed to vary. The magnetic field dependence of these side holes, in both the magnitude and direction of the field, is consistent with these side holes being the result of optical transitions where the spin of a N-N ^{19}F nucleus, with its isotropic magnetic moment of 4.0 kHz/G, is flipped along with the excitation of the Pr^{3+} ion to the $^1D_2$ state.

To confirm that the origin of these side holes are due to the neighbouring ^{19}F nuclei and not to Zeeman structure in the Pr^{3+} ion, the total hole structure within 5 MHz of the centre hole as function of the field applied along the C_3 axis was investigated. Fig 5.16 shows a typical spectrum. The burn pulse duration was increased to 5 ms to accentuate the side hole structure. In Fig 5.17 the frequency of the side holes is plotted as a function of the applied field strength. Fitted to this data is the theoretical position of the side holes due to the hyperfine structure in the $^1D_2(\Gamma_1)$ state (thin lines). The thick line shows the expected position of the side holes due to ^{19}F spin flips with a gradient of 4.0 kHz/G. The gradient of the line fitted to the points lying close to this line was 3.95 ± 0.1 kHz/G.

To obtain an estimate of the relative strength of these F spin flip transitions the saturation of the optical transition of the burn pulse was reduced by reducing the duration of the pulse to 200 μs, reducing the laser power to 100 μW and the diameter of the laser spot on the crystal was doubled to 400 μm. From the nutation frequency estimated from the photon echo measurements the nutation frequency under the conditions just outlined should be 2 kHz. With a nutation frequency of 2 kHz less than 25% of the ions in resonance with the laser will be excited during a 200 μs pulse. Under these low saturation conditions the depths of the holes should reflect the relative strengths of the associated transitions. The relative depth of each side hole to the centre hole for a hole burnt in the presence of a magnetic field of 34 G was 20% as shown in Fig 5.18. The theoretical value of the relative strength of the spin-flip transitions is 7%, calculated using the methods described in Section 5.2.6. The measurement was repeated for two other magnetic fields also shown in Fig 5.18. The depth of the side holes were observed to decrease with increasing applied magnetic field, consistent with the behaviour predicted in Section 5.2.6.

5.4.2 Time evolution of spectral holes

A selection of typical scans from a series of time resolved spectra following the evolution of a hole burnt in the presence of a 250 G field are shown in Fig 5.19. The holes were burnt with 10 mW pulses 1 ms long. Fig 5.20 shows the area of the hole as a function

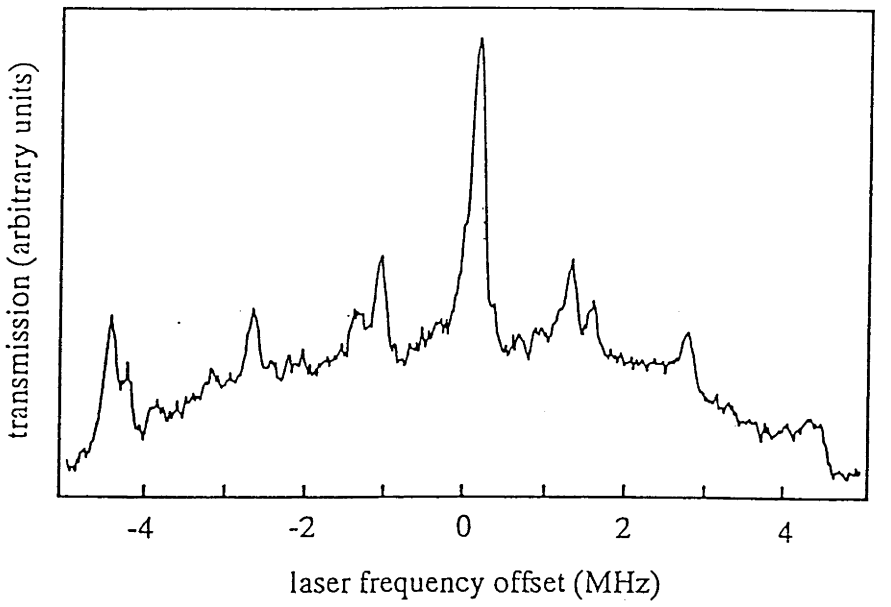

Figure 5.16 Optical holeburning spectrum taken in the presence of a 305 G magnetic field parallel to the C_3 axis. A laser power of 40 mW was used to burn the hole. The sideholes associated with the ^{19}F nuclear spin flip transitions are approximately 1.2 MHz either side of the central hole. The other sideholes present are due to the Zeeman structure associated with the Pr^{3+} ion.

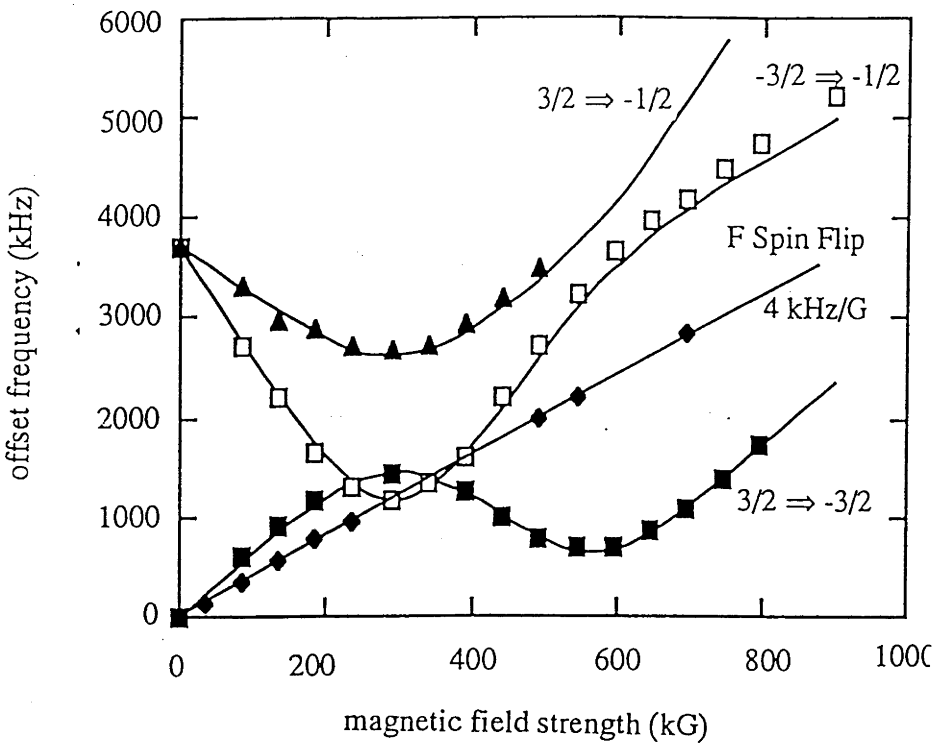

Figure 5.17 Side hole frequencies plotted as a function of the applied magnetic field. The field is applied along the C_3 axis of the crystal. The thin lines give the theoretical position of the side holes due to the Zeeman structure in the $^1D_2$ ($\Gamma 1$) state. The thick line shows the expected position of the side holes to ^{19}F.

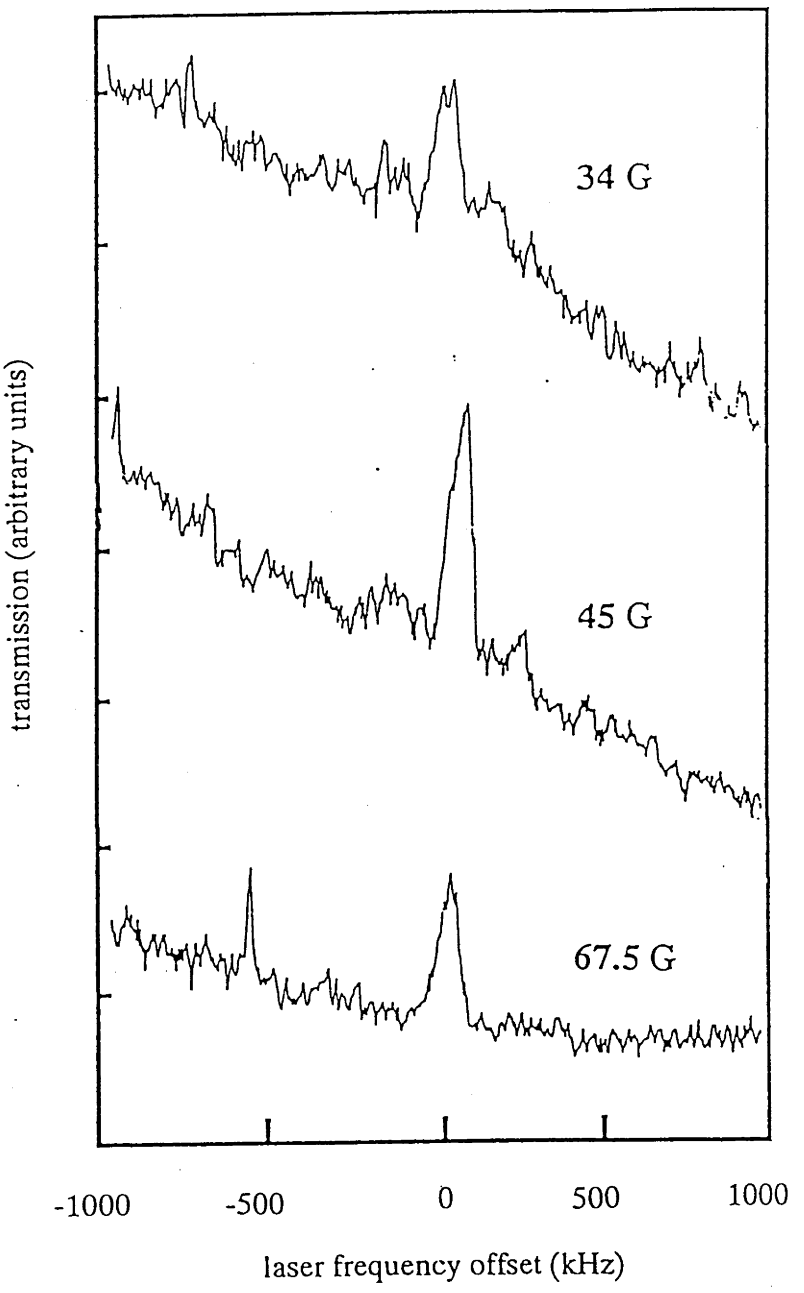

Figure 5.18 Holeburning spectra taken in the presence of a small magnetic field parallel to the C_3 axis. The holes were burnt with 0.1 mW pulses, 200 μs long.

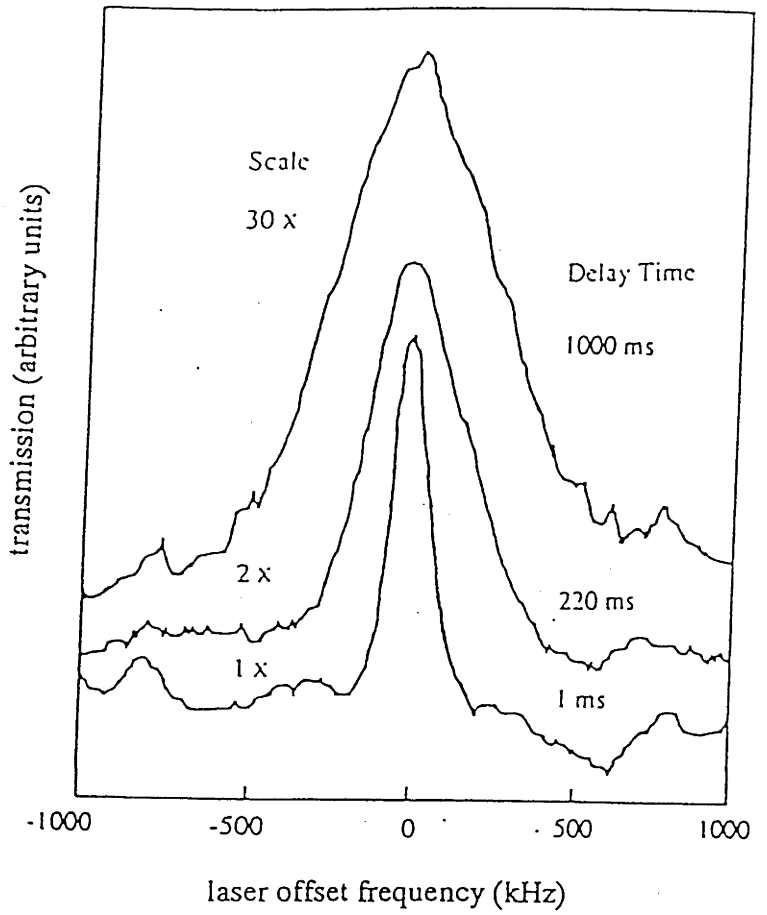

Figure 5.19 Time resolved spectral hole, burnt in the presences of a 250 G magnetic field parallel to the C_3 axis of the crystal field.

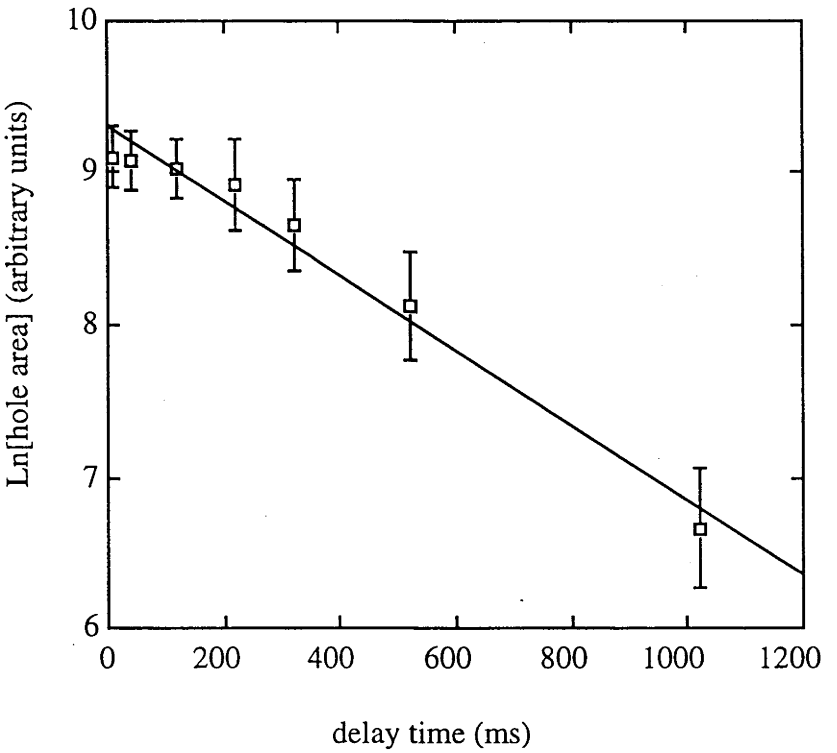

Figure 5.20. Time dependence of the area of the optical hole, for a magnetic field of 250 G parallel to the C_3 axis. The holes were burnt using 10 mW pulses 1 ms long.

of the delay between the burning and reading of the hole respectively. The lifetime of the hole area was 400 ± 50 ms. The lineshape of the hole was found to fall between a Gaussian and a Lorentzian profile. This profile was preserved as the hole broadened from 130 kHz at 2 ms out to 580 kHz at 1.5 s. The observed broadening during this interval of 450 kHz is significantly larger than the 100 kHz inhomogeneous broadening in the ground state hyperfine transitions observed by Wong *et al.* and the theoretical N-N ^{19}F nuclear contribution to the inhomogeneous broadening of the all the $^3H_4(\Gamma_1)$ - $^1D_2(\Gamma_1)$ optical transitions (see Table 5.5). I concluded from this that a hole broadening mechanism other than the magnetic interactions of the N-N ^{19}F nuclei must also be operating.

To determine the nature of the hole broadening mechanism operating in the presence of moderate magnetic fields, the time evolution of the hole width as a function of the strength of the applied field was investigated. The results of the study are shown in Fig 5.21.

The evolution of the spectral holes was also studied in the presence of larger fields, where the chemical shift in the Larmor frequencies of the N-N ^{19}F nuclei is likely to be significant. Two holeburning spectra taken in the presence of a 30 kG field are shown in Fig 5.22 one taken with a 10 ms delay the other with a 10 s delay. The area of the hole was observed not to change significantly over the 10 seconds. The time dependence of the width of a hole burnt in the presence of the 30 kG field is shown in Fig 5.21. Finally the width of the hole as a function of the applied magnetic field is shown in Fig 5.23. The width of the hole was recorded at delays of 10 ms and 200 ms, the laser power of the burn pulse was set to 20 mW and the pulse duration used was 1 ms. The general trend observed was for the hole width to increase as the field was increased from a field of 1 kG at a rate between 10 and 20 Hz/G, with an anomalous decrease between 20 and 30 kG.

5.5 Discussion

5.5.1 Side hole structure

The results presented in Fig 5.17 clearly shows that the frequency of the sideholes shift linearly with the applied magnetic field, at a rate of 3.95 ±0.1 kHz/G , and are not related to the Pr^{3+} hyperfine structure. This along with the isotropic nature of the Zeeman splitting confirms that these sideholes are due to optically induced F spin flips. As mentioned in Section 5.1 similar neighbouring spin-flip transitions have been observed in

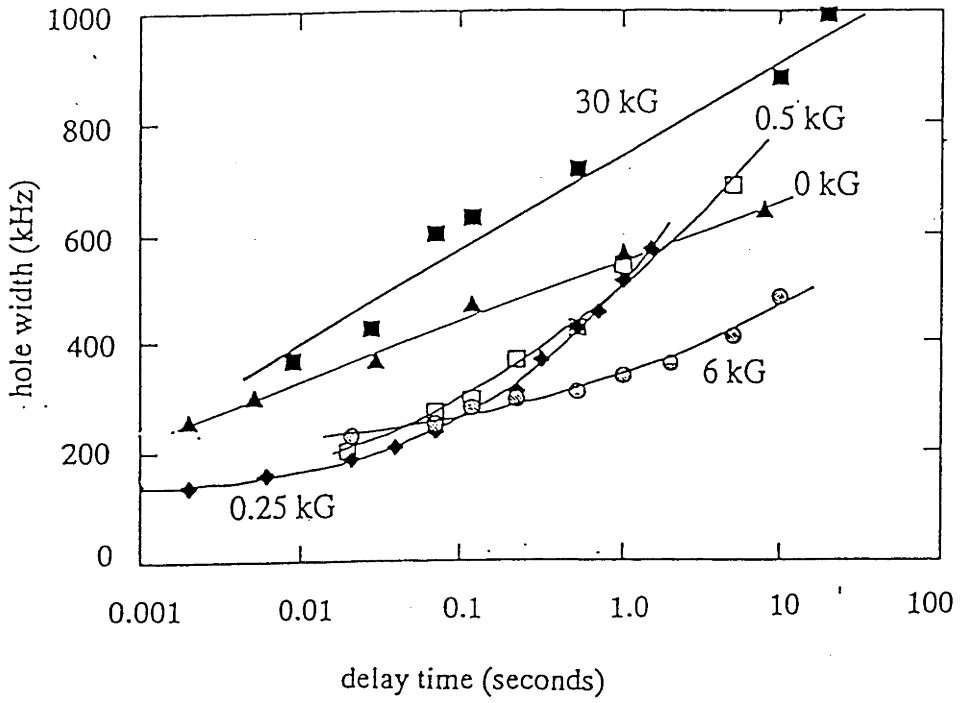

Figure 5.21 Time dependence of the hole width observed as a function of the applied magnetic field, for a field applied along the C_3 axis of the crystal.

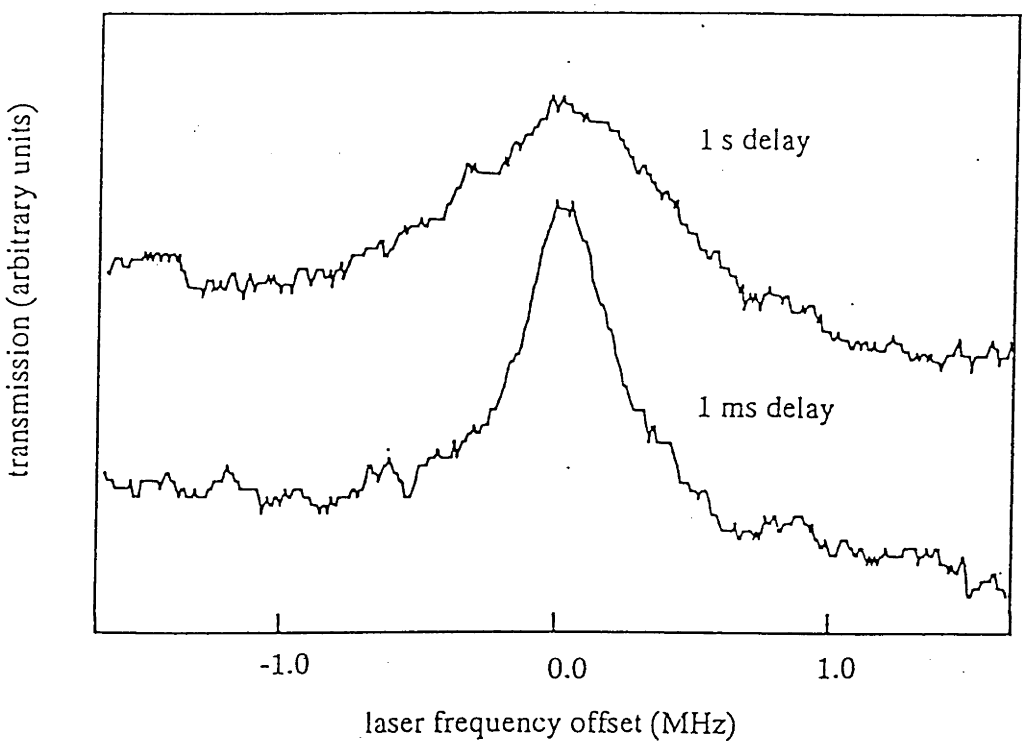

Figure 5.22 Time resolved optical hole spectra of holes burnt in the presence of a 30 kG magnetic field parallel to the C_3 axis.

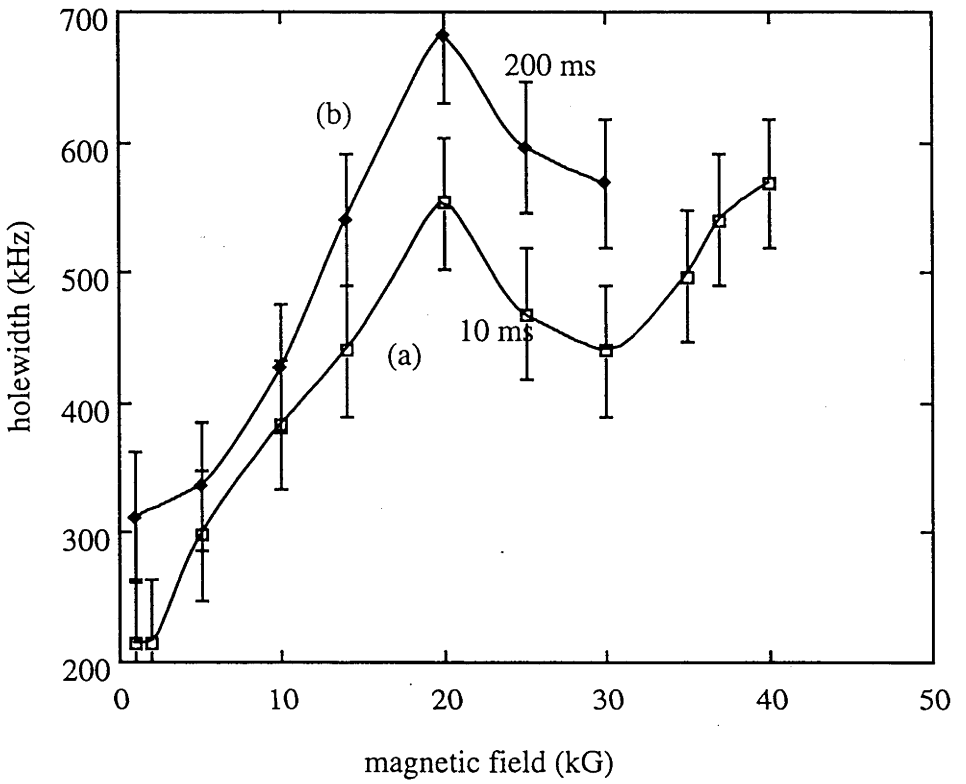

Figure 5.23 Linewidth of spectral holes (FWHM) as a function of the applied magnetic field. The magnetic field was applied along the C_3 axis. The holes were burnt using 10 mW pulses 1 ms long. For trace (a) the delay between burning and probing the hole was 10 ms, whilst for trace (b) it was 200 ms.

holeburning spectra of the $^4I_{15/2} \Rightarrow {}^4F_{7/2}$ transition in $LiYF_3:Er^{3+}$ [Wannemacher *et al.* 1991] although in this case even in a zero applied field there is a significant field at the neighbouring F site due to the large electronic moment of the Er^{3+} ion. In zero field these F spin-flip transitions were clearly resolvable from the central transition. In the present case there is only the weak enhanced nuclear moment of the Pr^{3+} ion and so even for the N-N ^{19}F nuclei the zero field shifts are very small and unresolved. A field of a few gauss is sufficient to dominate the praseodymium field and give the observed linear splitting. It is likely that the narrowing of the homogeneous linewidth observed on the application of an external magnetic field [DeVoe *et al.* 1979] was partially due to the removal of this unresolved structure as well as (proposed by DeVoe *et al.*) a retardation of the cross-relaxation rate of the ^{19}F nuclei.

The discrepancy, of a factor of 2, between the relative depth of the side holes and the calculated relative transition strengths of the optical spin-flip transitions is not surprising considering the assumptions made in the calculations. If an exchange interaction is present as well as the point dipole interaction assumed in the calculations, the spin-flip transitions will be stronger than predicted. An exchange interaction will also increase the magnetic contribution to the inhomogeneous broadening of the hyperfine transitions. The observed groundstate hyperfine transition linewidths of 100 kHz [Wong *et al.* 1983] are less than a factor of 2 larger than the theoretical prediction made assuming a point dipole interaction (see Table 5.5). This implies the exchange interaction is comparable or smaller than the point dipole interaction. Such an increase in the interaction strength could explain the higher than predicted transition strengths. The effect of assuming that the interaction of the Pr^{3+} ion and each of the ^{19}F nuclei can be considered separately and ignoring the interactions between the ^{19}F nuclei is unclear. It is not unreasonable to speculate that it may have lead to an underestimation of the transition strengths of the optical spin-flip transition.

5.5.2 Time evolution of spectral holes

The minimum observed hole width of 80 kHz (Fig 5.18) is 38 kHz broader than the width predicted from the photon echo measurements. The estimated contribution to the width from power broadening and from the Fourier width of the 200 μs burn pulse is 12 kHz. The remainder of this discrepancy is likely to be due to rapid spectral diffusion during the 1 ms delay between burning the hole and reading it. Such a fast diffusion is consistent with the observation of Muramoto et al. [1992].

In regard to identifying the hole broadening mechanism the following observations can be made from the magnetic field dependence of the time dependent hole broadening data presented in Fig 5.21:

On increasing the magnetic field from 0 to 250 G, the rate of hole broadening decreased for times less than 50 ms and increased for times after this point.

Doubling of the field to 0.5 kG produced only small changes to the hole evolution. This indicates that the chemical shift of the Larmor frequency of the ^{19}F nuclei , which is proportional to the applied field, plays only a minor role in the hole broadening mechanisms.

The broadening of the hole over the period 20 ms - 1.5 s was reduced from 400 kHz in a field of 0.25 kG down to 100 kHz when the field was increased to 6 kG.

The reduction of the hole broadening by 75% suggests that at least 300 kHz of the hole width in an applied field of 0.25 kG at 1.5 s delay is of a magnetic origin. This 300 kHz contribution to the hole width is significantly larger than can be accounted for by magnetic dipole interactions between the Pr^{3+} ion and the surrounding F nuclei. The predicted linewidth calculated in Section 5.2.7 was only 77 kHz. Further, the 300 kHz contribution is significantly larger than the inhomogeneous linewidths of the ground and excited state hyperfine transitions (see Table 5.5). This implies that a large component of the observed hole broadening is not due to fluctuating local magnetic fields, though its rate does depend on the applied magnetic field.

I attributed this component of the hole broadening to the spatial migration of the Pr^{3+} hyperfine excitations via Pr-Pr cross relaxations process described in Section 5.2.10. The observed magnetic field dependence of the hole broadening rate is due to changes in the Pr-Pr mutual spin-flip rate. The broadening is associated with the strain broadening of the optical transition and hence will not appear as inhomogenous broadening of the hyperfine transitions. The process is not spectral diffusion as the resonant frequencies of the ions are not changing; rather, different ions are sampled as the redistribution of the hyperfine population created by the laser spatially diffuses through the crystal. That this mechanism is operating as a broadening mechanism indicates there is a strong correlation in the distance between the Pr^{3+} ions and their optical frequency in this sample.

The changes in the Pr-Pr cross relaxation rate with magnetic field is likely to be due to changes in the N-N ^{19}F nuclear cross-relaxation rate. In Section 5.2.9 it was shown that

on increasing an external magnetic field the chemical shift of the N-N ^{19}F nuclei will increase the detuning of these nuclei from the bulk ^{19}F nuclei, slowing down the rate a which N-N F's undergo cross-relaxations. At a field of 6 kG along the C_3 axis the magnetic moment induced on the electronic groundstate, calculated using Equation 5.32, is 25 kHz/G. This moment is larger than the groundstate enhanced nuclear moment so the chemical shift will significantly increase the detuning of the N-N ^{19}F nuclei. As shown in Section 5.2.9 slowing down the N-N ^{19}F spin-flips will also slow down the Pr-Pr cross relaxation rate. It should be noted that this chemical shift will not affect the hyperfine transition frequencies and hence the resonance condition between the Pr ions directly as the chemical shift is independent of the Pr nuclear state.

The preservation of the hole profile as it broadens, observed for the holes burnt in a 250 G field, suggests that the broadening is the result of many frequency jumps which are small compared to the linewidth of the hole. If the broadening was due to frequency jumps comparable in size to the hole width we would expect to observe the hole to form a pedestal. With an initial hole width of 120 kHz at 2 ms these frequency jumps would have to be 60 kHz or smaller so as not to observe a distortion in the hole profile. For the hole to broaden from 120 kHz to 580 kHz at least 5 such jumps would be necessary over the 1.5 s interval. Therefore the lower limit for the Pr-Pr cross relation rate is 3.5 sec^{-1}. This value is in reasonable agreement with the theoretical estimate of the cross-relaxation rate, calculated in Section 5.2.10, where the N-N ^{19}F nuclear spins were assumed to be dynamic on a time scale short compared to the resonant Pr-Pr cross relaxation rate.

If these measurements were repeated for a Pr^{3+} doped sample with a crystal host with no or only small magnetic moments, where initial hole widths of the order 10 kHz can be expected, it might be possible to determine the size of the frequency jumps and hence the cross-relaxation rate. The cross-relaxation rate observed in this situation is likely to be significantly different to that in Pr^{3+}:LaF_3, because the broadening of the hyperfine transitions is likely to be dominated by the static strain broadening, rather than by dynamic magnetic interactions.

That the hole burnt in the presence of a 250 G field was observed with a decay time of 400 ± 50 ms indicates that the population distribution in the groundstate hyperfine levels of the ions in the region of the hole is relaxing on a similar time scale. Shelby *et al.* [1980] proposed two mechanisms for the relaxation they observed in zero magnetic field. The first involved a cross relaxation process involving simultaneous spin flips of the Pr nucleus and three surrounding La nuclei. This mechanism only acts upon the 8.47 MHz

transition and was found to occur at a rate of 0.18 sec^{-1}. This cross-relaxation was also expected to be strongly retarded on the application of a magnetic field which would detune the Pr and La splittings. It is therefore unlikely that this mechanism can account for the filling of the hole observed in the present measurements.

This leaves the second mechanism proposed by Shelby *et al.*, Pr-Pr cross relaxation, which has been discussed in detail in Section 5.2.10 and above in relation to hole broadening. For this process to reduce the area of the hole there must be cross relaxations between Pr nuclei which differ in their optical frequencies by more than 1 MHz. The rate of these cross relaxations will be given by the lifetime of the hole's area. This rate of 2.5 sec^{-1} is similar to the estimated lower limit of the cross-relaxation between Pr^{3+} ions of similar optical frequencies. From this result it appears that for typical Pr hyperfine excitation, at least one of the cross-relaxations will occur between Pr ions of similar optical frequencies before a cross-relaxation between Pr^{3+} ions of dissimilar frequencies.

The evolution of spectral holes where the spatial diffusion of the hyperfine excitation is occurring depends on the spatial distribution of the Pr^{3+} ions and on the crystal strain field. A simple model to explain the hole evolution is that the strain field consists of domains where the ions' optical frequencies vary only slightly, but where the optical frequencies can differ greatly between domains. The boundaries of the domains should present no barrier to the spin diffusion as the majority of the broadening of the hyperfine transitions is due to Pr-F interactions, which are constantly varying, and not strain. The diffusion within a domain will produce broadening whilst the diffusion across domain boundaries fills in the hole. The rate at which a hole broadens compared to the rate at which it decays will depend on the size of these domains, the variation of the optical frequencies within the domains and the density of the Pr^{3+} ions.

The increase of the lifetime of the hole area from 400 ms to well in excess of 10 s when the applied magnetic field was increased from 250 G to 30 kG is further indication that the Pr-Pr cross relaxation rate decreases in large applied magnetic fields. In the present case the cross-relaxation rate appears to have decreased by more than a factor of 20. This decrease in the cross-relaxation rate should also reduce the hole broadening rate due to the spatial diffusion of the hyperfine excitation. That the holes burnt in the 30 kG field are broader than holes burnt at 6 kG, or at lower fields, at all observed delays is attributed to the increase of the frequency shifts of the optical transition from the Pr-F interactions in the larger magnetic field. The total broadening of the optical transition due

to the chemical shift interaction, calculated in Section 5.2.9, is 360 kHz for the 30 kG field.

Further evidence that the increase in the hole width is due to the chemical shift is that the general trend of the hole width to increase at a rate of about 13 Hz/G as the magnetic field is increased (see Fig 5.23), is similar to the rate of increase of the total optical linewidth of 12 Hz/G due to the chemical shift calculated in Section 5.2.9. The reason for the anomalous decrease in the width of the hole between 20 and 30 kG for delays times of 10 and 200 ms seen in Fig 5.23 is unclear. Further measurements need to be made with longer delay times to see how this anomaly evolves in time.

In future work it should be possible to confirm the role of the Pr-Pr cross-relaxation by studying the evolution of the hole in the presence of a magnetic field perpendicular to the C_3 axis. In such a field the hyperfine structure of the Pr^{3+} ions in the three different C_2 sites will be different and cross-relaxations between ions of different sites will be hindered. This should result in a slower rate of hole broadening. It is also hoped that by studying holeburning in samples with hosts with no magnetic moments and varying Pr^{3+} concentration it will be possible to improve our understanding of the Pr^{3+} distribution within the crystal and the crystal strain field.

One of the initial aims of this work was to investigate the dynamics of the N-N ^{19}F nuclear spins by observing spectral diffusion generated by these nuclear spins, using spectral holeburning. It was not possible to clearly distinguish between the hole broadening due to the spectral diffusion and the that due to the Pr-Pr cross-relaxation. By studying samples with significantly lower concentrations of Pr^{3+} ions than that used in this work it should be possible to decrease the rate of the Pr-Pr cross-relaxation rate to a level such that its contribution to the hole broadening will not mask any spectral diffusion present.

5.6 Conclusion:

Optical transitions where the nuclear spin of N-N F ions are flipped have been identified. These transitions are the result of the coupling of the enhanced nuclear moment of the Pr^{3+} ion with the nuclear moment of the N-N F ions. In a magnetic field of 34 G along the C_3 axis approximately 20% of the total optical transition strength is associated with these ^{19}F spin flip transitions. This relative transition strength was found to be approximately 3 times larger than the theoretical value.

The broadening of spectral holes has been observed in $LaF_3:Pr^{3+}$ on a time scale of seconds. It was demonstrated that a hole broadening mechanism other than that due to F spin-flips is also operating. It has also been demonstrated that this new mechanism is due to the spatial diffusion of the Pr^{3+} hyperfine excitation via a cross-relaxation between Pr^{3+} ions. The dependence of this broadening mechanism on the applied magnetic field is attributed to the magnetic field dependence of the N-N ^{19}F nuclear cross-relaxation rate and the effect this has on the Pr-Pr cross-relaxation rate.

Chapter 6 Conclusion

In this work an ultra-high-resolution dye laser system, modified from a commercial laser, has been used to investigate a number of interesting aspects of the spectroscopy of rare earth doped crystals inaccessible to commercially available dye lasers. The linewidth of the ultra-narrow linewidth ring dye laser (Coherent 699/29) was demonstrated to be less than 2 kHz over time intervals of tens of milliseconds. The demonstration was performed by burning and then probing a spectral hole with a 3.7 kHz linewidth (FWHM) in the optical $^1F_0 \Rightarrow {}^1D_0$ transition in $Y_2O_3:Eu^{3+}$. This to the author's knowledge is the narrowest spectral hole observed in a solid. Over longer time intervals the frequency of the laser was observed to drift at rates of the order of 100 kHz/sec. The long term stability is believed to be limited by the "Newport Supercavity" used as the frequency reference for stabilising the laser frequency. It is hoped that the long term stability of the system will be improved by replacing the "Newport Supercavity" with a custom built cavity based on a zerodur rod. These anticipated improvements will allow the study of time dependent holeburning over indefinitely long time intervals.

Using the frequency stabilised laser, the coherent response of the $^1F_0 \Rightarrow {}^1D_0$ transition in $KEu(WO_4)_2$ was investigated. The dephasing rate of the transition was studied as a function of both the magnitude and the phase of the optical driving field. Four coherent transient techniques were used; photon echoes, free induction decay, rotary echoes and a new technique, coherence phase locking. The coherence phase locking technique, although it does parallel the NMR technique of spin locking, has not been previously demonstrated in the visible regime.

Non-optical Bloch equation behaviour similar to that observed in $LaF_3:Pr^{3+}$ [DeVoe and Brewer 1983] and ruby [Szabo and Muramoto 1989] was observed using free induction decay and coherence phase locking. It was concluded from a comparison between the four transient techniques that the relative phase between the driving field and the transitions dipole moment is an important parameter in interpreting the observed non-optical Bloch equation behaviour. Analyses of the coherence relaxation in these measurements was complicated by the presence of instantaneous spectral diffusion in the $KEu(WO_4)_2$ sample. For this reason no attempt was made to model the system beyond comparing the observed coherent transient responses with the predictions of the unmodified optical Bloch equations.

Experiments using modified coherence phase locking techniques have been proposed to study the dependence of the coherence dephasing on the relative phase of the driving

field. In future investigations it is hoped that the non-optical Bloch equation behaviour can be fully characterised, using these new techniques, for samples where the mechanism of the coherence relaxation is well understood.

Time resolved holeburning in the $^3H_4 \Rightarrow {}^1D_2$ transition in $LaF_3:Pr^{3+}$ was used to investigate magnetic interactions involving the Pr^{3+} ions. Hole broadening observed over time intervals of up to 1 second was attributed at least partially to a mechanism involving the cross relaxation of Pr^{3+} ground state hyperfine levels between adjacent ions. In this mechanism the hyperfine excitations associated with the spectral hole spatially diffuse through the crystal, via cross-relaxations. As these excitations migrate through the crystal they sample ions whose optical transition frequencies are different from the ions excited by the laser. The fact that the spatial diffusion results in a broadening of the hole indicates a correlation between the ion's position and its optical frequency. By studying Pr-Pr cross-relaxation processes using time resolved holeburning in a wide range of crystal hosts and Pr^{3+} ion concentrations, it is anticipated that it should be possible to improve our knowledge of the spatial distribution of both the Pr^{3+} ions and the crystal strain field.

The observed dependence of the Pr-Pr cross-relaxation rate on the applied magnetic field was attributed to the magnetic field dependence of the nearest-neighbour ^{19}F nuclear cross-relaxation rate and the effect the ^{19}F nuclear cross-relaxations have on the Pr-Pr cross-relaxations.

A new type of optical transition in $LaF_3:Pr^{3+}$ was identified. These transitions in which the spin of a neighbouring ^{19}F nuclei is flipped with the optical excitation of the Pr^{3+} ion from the ground state to the $^1D_2$ state was identified from holeburning spectra. They are a consequence of the interaction between the nuclear magnetic moment of the nearest-neighbour ^{19}F nuclei with the enhanced nuclear moment of the Pr^{3+}. Similar transitions have been observed before but only for Er^{3+} an ion with a large first order electronic magnetic moment [Wanaaemacher et al. 1991]. Because the side holes due to these transitions were only clearly visible for frequency separations less than a few megahertz it is unlikely this transition could have been identified without the use of an ultra-high resolution laser.

Appendix A: DC Response of Error Signal

The calculation of the DC error signal follows closely the calculations of Houssin *et al.* [1988] and is present here for the convenience of the reader and to provide a basis for the calculation of the AC signal in Appendix B.

After passing through the external electro-optic phase modulator (see Fig 2.1) the laser field is of the form

$$E = E_0 \exp[i\omega_c t + \delta \sin \omega_m t],, \tag{A.1}$$

where $\upsilon_c=\omega_c/2\pi$ is the frequency of the laser, $\upsilon_m=\omega_m/2\pi$ is the modulation frequency and δ is the modulation index. If $\delta<1$ we can neglect all harmonics of the modulation frequency and express the laser field as a carrier and two sidebands

$$\begin{aligned} E = E_0\big[&J_0(\delta)\exp[i\omega_c t] + J_1(\delta)\exp[i(\omega_c+\omega_m)t] \\ &-J_1(\delta)\exp[i(\omega_c-\omega_m)t]\big], \end{aligned} \tag{A.2}$$

where $J_o(\delta)$ and $J_1(\delta)$ are Bessel functions of the first kind.

The reflection of a plane wave from a plane Fabry-Perot interferometer with identical mirrors is given by

$$\frac{E_r}{E_i} = \rho - \rho t^2 \frac{\exp[-i\theta]}{1-\rho^2\exp[-i\theta]}, \tag{A.3}$$

where ρ^2 is the coefficient of reflection of the mirrors, $t^2 = (1-\rho^2)$ and $\theta = \dfrac{2\omega d}{c}$ is the phase accumulated on one round trip of the cavity. The result of reflecting the phase modulated light off the cavity is then given by

$$E_r = E_0\left[J_o(\delta)\left[\rho+\rho t^2\frac{\rho^2-\exp[-i\theta_c]}{D_c}\right]\exp[i\omega_c t]\right.$$
$$+J_1(\delta)\left[\rho+\rho t^2\frac{\rho^2-\exp[-i(\theta_c+\theta_m)]}{D_c}\right]\exp[i(\omega_c+\omega_m)t] \quad , \quad \text{(A.4)}$$
$$\left.-J_1(\delta)\left[\rho+\rho t^2\frac{\rho^2-\exp[-i(\theta_c-\theta_m)]}{D_c}\right]\exp[i(\omega_c-\omega_m)t]\right]$$

where

$$D_c = 1+\rho^4-2\rho^2\cos\theta_c,$$
$$D_+ = 1+\rho^4-2\rho^2\cos(\theta_c+\theta_m),$$
$$D_- = 1+\rho^4-2\rho^2\cos(\theta_c-\theta_m),$$

The photocurrent on the photodiode is given by

$$I=\frac{\eta q}{h\nu}E_r\bullet E_r^*, \quad \text{(A.5)}$$

where η is the quantum efficiency of the detection and q is the charge on an electron [Yariv 85]. The component of this current at the modulation frequency is

$$I(\omega_m)=\frac{2\eta qE_o^2}{h\nu}J_0(\delta)J_1(\delta)\left\{\cos\omega_m t\left\{\left[\rho+\rho t^2\frac{\rho^2-\cos\theta_c}{D_c}\right]\left[\left[\rho+\rho t^2\frac{\rho^2-\cos(\theta_c+\theta_m)]}{D_+}\right]\right.\right.$$
$$\left.-\left[\rho+\rho t^2\frac{\rho^2+\cos(\theta_c-\theta_m)]}{D_-}\right]\right]+\frac{\rho t^2\sin\theta_c}{D}\left[\frac{\rho t^2\sin(\theta_c+\theta_m)}{D_+}-\frac{\rho t^2\sin(\theta_c-\theta_m)}{D_-}\right]\Bigg\}$$
$$+Sin\omega t\left\{\frac{-\rho t^2\sin\theta_c}{D_c}\left[\left[\rho+\rho t^2\frac{\rho^2-\cos(\theta_c+\theta_m)]}{D_+}\right]+\left[\rho+\rho t^2\frac{\rho^2+\cos(\theta_c-\theta_m)]}{D_-}\right]\right.$$
$$\left.\left.\left[\rho+\rho t^2\frac{\rho^2+\cos\theta_c]}{D}\right]\left[\rho t^2\frac{\sin(\theta_c+\theta_m)]}{D_+}+\rho t^2\frac{\sin(\theta_c-\theta_m)]}{D_-}\right]\right\}\right\}$$

(A.6)

The signal from the photodiode is mixed with $\sin(\omega_m t)$ to give the error signal

$$V = g\frac{2\eta qE_o^2}{h\nu}J_0(\delta)J_1(\delta)\left\{\frac{\rho t^2\sin\theta_c}{D_c}\left[\left[\rho+\rho t^2\frac{\rho^2-\cos(\theta_c+\theta_m)]}{D_+}\right]\right.\right.$$
$$\left.+\left[\rho+\rho t^2\frac{\rho^2+\cos(\theta_c-\theta_m)]}{D_-}\right]\right] \qquad (A.7)$$
$$-\left[\rho+\rho t^2\frac{\rho^2+\cos\theta_c]}{D}\right]\left[\rho t^2\frac{\sin(\theta_c+\theta_m)]}{D_+}+\rho t^2\frac{\sin(\theta_c-\theta_m)]}{D_-}\right]\Bigg\}$$

where g takes into account the current-to-voltage conversion of the photodiode signal, the gain of the pre- and post-amplifiers, the amplitude of the local oscillator and the efficiency of the mixer.

When the resonance linewidth of the cavity is than smaller than ω_m and ω_m is smaller than the free spectral range, there are three main contributions to the error signal:

$$V = g\frac{2\eta qE_o^2}{h\nu}J_0(\delta)J_1(\delta)\rho^2t^2\left[\frac{\sin\theta_c}{D_c}-\frac{\sin(\theta_c+\theta_m)}{D_+}-\frac{\sin(\theta_c-\theta_m)}{D_-}\right] \qquad (A.8)$$

For frequencies close to the resonance peak the error signal is approximately described by

$$V = g\frac{2\eta qE_o^2}{h\nu}J_0(\delta)J_1(\delta)\rho^2t^2\left[\frac{\sin\theta_c}{D_c}\right] \qquad (A.9)$$

The slope of the frequency discriminator at the resonance peak is

$$\frac{\partial V}{\partial \nu} = g\frac{2\eta qE_o^2}{h\nu}J_0(\delta)J_1(\delta)\rho^2t^2\frac{2d}{cD_c(\theta_c=\theta_0)}$$

$$= g\frac{2\eta qE_o^2}{h\nu}J_0(\delta)J_1(\delta)\frac{\rho}{\Delta\nu_{1/2}} \qquad (A.10)$$

where θ_0 is the on resonance phase shift, which will be a multiple of 2π. This gradient can be related to the peak-to-peak voltage of the error signal $V_{p\text{-}p}$ and $\Delta\upsilon_{1/2}$ is the FWHM width of the cavity resonance given by:

$$\Delta\nu_{1/2} = \frac{c(1-\rho^2)}{2d\rho} \qquad (A.11)$$

Equation A.9 reaches its maximum when

$$\begin{aligned}\theta_{\max} &= \frac{4\pi\nu_{\max}d}{c} \\ &= \frac{2\sqrt{2}\pi\left(1-\rho^2\right)}{\sqrt{\rho^2+1}}\end{aligned} \tag{A.12}$$

Comparing Equations A.11 and A.12 it can be seen that for a high finesse cavity with $\rho\approx1$, $\Delta\upsilon_{1/2}\approx2\upsilon_{\max}$. From Equation A.10 we have

$$\begin{aligned}\frac{V_{p-p}}{\Delta\nu} &\approx g\frac{2\eta qE_o^2}{h\nu}J_0(\delta)J_1(\delta)t^2\frac{2d}{cD_c\left(\theta_c=\theta_{\max}\right)} \\ &\approx g\frac{2\eta qE_o^2}{h\nu}J_0(\delta)J_1(\delta)t^2\frac{d}{cD_c\left(\theta_c=\theta_o\right)}\end{aligned} \tag{A.13}$$

as D is proportional to the cavity transmission and $\rho\approx1$. Substituting Equation A.10 into A.13 we obtain:

$$\delta V = 2\left(\frac{V_{p-p}}{\Delta\nu_c}\right)\delta\nu \tag{A.14}$$

This simply states that the gradient of the frequency discriminator about the resonance peak is given by twice the peak to peak voltage of the error signal divided by the FWHM line width of the resonance.

Appendix B AC Response of Error Signal

The AC frequency perturbation is introduce as an FM modulation of the laser light at the frequency ω_n, which is assumed to be less than ω_m. The laser field after the electro-optic modulator is given by

$$E = E_0 \exp[i\omega_c t + \delta_m \sin \omega_m t + \delta_n \sin \omega_n t], \tag{B.1}$$

where δ_n is the modulation index of the noise and δ_m is the modulation index of the modulation introduced by the phase modulator. If δ_n, $\delta_m<1$ we can neglect all harmonics, sum and difference frequencies of the modulation frequencies and express the laser field as a carrier and four sidebands

$$\begin{aligned} E = E_0\big[& J_0(\delta_m)J_0(\delta_n)\exp[i\omega_c t] + J_1(\delta_m)\exp[i(\omega_c+\omega_m)t] \\ & -J_1(\delta_m)\exp[i(\omega_c-\omega_m)t] + J_1(\delta_n)\exp[i(\omega_c-\omega_n)t] \\ & -J_1(\delta_n)\exp[i(\omega_c-\omega_n)t]\big], \end{aligned} \tag{B.2}$$

The result of reflecting this phase modulated field off the cavity is

$$\begin{aligned} E_r = E_0\Bigg[& J_o(\delta_m)J_o(\delta_n)\left[\rho+\rho t^2\frac{\rho^2-\exp[-i\theta_c]}{D_c}\right]\exp[i\omega_c t] \\ & +J_1(\delta_m)\left[\rho+\rho t^2\frac{\rho^2-\exp[-i(\theta_c+\theta_m)]}{D_c}\right]\exp[i(\omega_c+\omega_m)t] \\ & -J_1(\delta_m)\left[\rho+\rho t^2\frac{\rho^2-\exp[-i(\theta_c-\theta_m)]}{D_c}\right]\exp[i(\omega_c-\omega_m)t] \\ & +J_1(\delta_n)\left[\rho+\rho t^2\frac{\rho^2-\exp[-i(\theta_c+\theta_n)]}{D_c}\right]\exp[i(\omega_c+\omega_n)t] \\ & -J_1(\delta_n)\left[\rho+\rho t^2\frac{\rho^2-\exp[-i(\theta_c-\theta_n)]}{D_c}\right]\exp[i(\omega_c-\omega_n)t]\Bigg] \end{aligned} \tag{B.3}$$

If we now assume that the carrier is in resonance with the reference cavity then $\theta_c=2\pi n$ and the first term in Equation B.3 disappears. The current in the photodiode is now given by

$$I = 2\frac{\eta q E_0^2}{h\nu_c} J_1(\delta_m) J_1(\delta_n) \left[\left[\rho + \rho t^2 \frac{\rho^2 - \cos\theta_m}{D_m} \right] \times \right.$$
$$\left[\rho + \rho t^2 \frac{\rho^2 - \cos\theta_n}{D_n} \right] \sin(\omega_n t)\sin(\omega_m t) +$$
$$\frac{\sin\theta_m}{D_m} \rho t^2 \left[\frac{\sin\theta_n}{D_n} \rho t^2 \right] \cos(\omega_n t)\cos(\omega_m t) +$$
$$\frac{\sin\theta_m}{D_m} \rho t^2 \left[\rho + \rho t^2 \frac{\rho^2 - \cos\theta_n}{D_n} \right] \sin(\omega_n t)\cos(\omega_m t) + \qquad \text{(B.4)}$$
$$\left. \left[\rho + \rho t^2 \frac{\rho^2 - \cos\theta_m}{D_m} \right] \left[\frac{\sin\theta_n}{D_n} \rho t^2 \right] \cos(\omega_n t)\sin(\omega_m t) \right]$$

When the signal from the photodiode is mixed with $\sin(\omega_m t)$ to give the error signal we obtain

$$V(\omega_n) = 2g\frac{\eta q E_0^2}{h\nu_c} J_1(\delta_m) J_1(\delta_n) \left[\rho + \rho t^2 \frac{\rho^2 - \cos\theta_m}{D_m} \right] \times$$
$$\left[\left[\rho + \rho t^2 \frac{\rho^2 - \cos\theta_m}{D_m} \right] \sin\omega_n t + \left[\frac{\sin\theta_n}{D_n} \rho t^2 \right] \cos\omega_n t \right] \qquad \text{(B.5)}$$

As $J_1(\delta_n) = \dfrac{\omega_p}{\omega_n}$ for $\delta_n << 1$ where ω_p is the amplitude of the frequency perturbation, $V(\omega_n)$ is approximately given by

$$V(\omega_n) = 2g\frac{\eta q E_0^2}{h\nu_c} J_1(\delta_m) \left[\rho + \rho t^2 \frac{\rho^2 - \cos\theta_m}{D_m} \right] \times$$
$$\frac{\omega_p}{\omega_n} \left[\left[\rho + \rho t^2 \frac{\rho^2 - \cos\theta_m}{D_m} \right] \sin\omega_n t + \left[\frac{\sin\theta_n}{D_n} \rho t^2 \right] \cos\omega_n t \right] \qquad \text{(B.6)}$$

Appendix C: Torrey's solution

It was shown by Torrey [Torrey 1949] that if W stands for any one of u, v, w the general solution of Equations 5.1, for the case of a constant driving field, may be written in the form

$$W = Ae^{-a\chi t} + Be^{-b\chi t}\cos(s\chi t) + \frac{C}{s}e^{-b\chi t}\sin(s\chi t) + D \qquad \text{(C.1)}$$

The constants a, b, s, A, B, C and D in equation C.1 are functions of T_1, T_2, Δ and χ. a, b and s are independent of the component of the Bloch vector represented by W, and they are also independent of the initial conditions. A, B, C and D depend on the component represented by W. A, B and C depend on the initial values of u, v and w. Torrey also showed that under the condition $1/T_1 < 1/T_2 << \chi$ the constants a, b, s can be approximated by

$$a = \left(1/\chi T_2 + 1/\chi T_1\left(\Delta/\chi\right)^2\right)\Big/\left(1+\left(\Delta/\chi\right)^2\right) + O\left[\left(1/\chi T_2 - 1/\chi T_1\right)^3\right],$$

$$b = 1/\chi T_2 - \frac{1}{2}\left(1/\chi T_2 - 1/\chi T_1\right)\Big/\left(1+\left(\Delta/\chi\right)^2\right) + O\left[\left(1/\chi T_2 - 1/\chi T_1\right)^3\right], \qquad \text{(C.2)}$$

$$s^2 = 1+\left(\Delta/\chi\right)^2 + O\left[\left(1/\chi T_2 - 1/\chi T_1\right)^3\right].$$

The constants D and A are given by

$$D = g(0)_i \Big/ a[b^2+s^2],$$
$$A = -g(-a)_i \Big/ a[(b-a)^2+s^2]. \qquad \text{(C.3)}$$

where

$$g_u(p) = u_0 p\left[1+\left(p+1/\chi T_1\right)\left(p+1/\chi T_2\right)\right] + \Delta/\chi\left(1/\chi T_1\right) + pw_0 + v_0,$$
$$g_v(p) = u_0 p\Delta/\chi\left(p+1/\chi T_1\right) + v_0 p\left(p+1/\chi T_2\right)\left(p+1/\chi T_1\right) - \left(1/\chi T_1 + w_0 p\right)\left(p+1/\chi T_2\right),$$
$$g_w(p) = u_0 p\Delta/\chi + v_0 p\left(p+1/\chi T_2\right) + \left(1/\chi T_1 + w_0 p\right)\left[\left(p+1/\chi T_2\right)^2 + \left(\Delta/\chi\right)^2\right]. \qquad \text{(C.4)}$$

The remaining constants B and C expressed in terms of a, b, s, A, D and the initial conditions are given by

(a) for W=u

$$B = -A + D + u_0, \quad C = aA + bB - {}^{1}\!/_{T_2\chi} u_0 - {}^{\Delta}\!/_{\chi} v_0,$$

(b) for W=v

$$B = -(A + B) + v_0, \quad C = aA + bB - w_0 - {}^{1}\!/_{T_2\chi} v_0 + {}^{\Delta}\!/_{\chi} u_0, \quad \text{(C.5)}$$

(c) for W=w

$$B = -(A + B) + w_0, \quad C = aA + bB + {}^{1}\!/_{T_1\chi}(1 - w_0) + v_0.$$

I found two mistakes in Torrey's original paper. The corrections are

$$g_u(p) = u_0 p\left[1 + \left(p + {}^{1}\!/_{\chi T_1}\right)\left(p + {}^{1}\!/_{\chi T_2}\right)\right] + {}^{\Delta}\!/_{\chi}\left[{}^{1}\!/_{\chi T_1} + p w_0 - v_0 p\left(p + {}^{1}\!/_{\chi T_1}\right)\right],$$

and

$$B = -(A + D) + u_0$$

References

Allen, L., and J. H. Eberly, 1975, 'Optical Resonance and Two Level Atoms' (Wiley, New York), pp. 28 ff and 52 ff.

Babbit, W. R., A. Lezama and T.W. Mossberg, 1989, Phys. Rev. B **39**, 1987.

Baker, J. M., and B. Bleaney, 1958, Proc. R. Soc. London Ser. A **245**, 156.

Berman, P. R., 1986, J. Opt. Am. **B 3**, 572.

Bjorklund, G. C., 1980, Opt. Lett. **5**, 15.

Bleaney, B., 1964, in 'Proceedings of the Third International Conference on Quantum Electronics', Vol. 1, P. Givet and N. Bloembergen, eds. (Columbia U. Press, 1964), p. 595.

Bloembergen, N., S. Shapiro, P. S. Pershan and J. O. Artman, 1959, Phys. Rev. **114**, 445.

DeVoe, R. G., A. Szabo, S. C. Rand and R. G. Brewer, 1979, Phys. Rev. Lett. **42**, 1560.

DeVoe, R. G. and R. G. Brewer, 1983, Phys. Rev. Lett. **50**, 1269.

DeVoe, R. G. and R. G. Brewer, 1984, Phys. Rev. A **30**, 2827.

Drever, R. W. P., J. L. Hall, F. V. Kowalski, J. Hough, G. M. Ford, A. J. Munley and H. Ward, 1983, Appl. Phys. B **31**, 97.

Equall, R. W., Y. Sun, R. L. Cone and R. M. Macfarlane, 1994, Phys. Rev. Lett. **72**, 2179.

Erickson, L. E., 1977a, Phys. Rev. B**16**, 4731.

Erickson, L. E., 1977b, Opt. Comm. **21**, 147.

Flinn, G. P., K. W. Ganem, M. L. Jones, R. S. Meltzer and R. M. Macfarlane, 1994, Phys. Rev. B **49**, 5821.

Gough, D., 1993, private communication.

Hall, J. L. and T. W. Hansch, 1984, Opt. Lett. **9**, 502.

Helmcke, J., S. A. Lee and J. L. Hall, 1982, Appl. Opt. **21**, 1686.

Helmcke, J., J. J. Snyder, A. Morinaga, F. Mensing and M. Glaser, 1987, Appl. Phys. B **43**, 85.

Helmcke, J., A. Morinaga, J. Ishikawa and F. Riehle, 1989, IEEE Trans Instrum. Meas. **38**, 524.

Houssin, M., M. Jardino, B. Gely and M. Desaintfuscien, 1988, Opt. Lett. **13**, 823.

Huang, J., J.M. Zhang, Z. Lezama and T.W.Mossberg, 1989, Phys. Rev. Lett. **63**, 78.

Kallenbach, R., C. Zimmerman, D. H. McIntyre and T. W. Hansch, 1989, Opt. Comm. **70**, 56.

Kallenbach, R., F. Schmidt-Kaler, M. Weitz, C. Zimmermann and T. W. Hansch, 1991, Opt. Comm. **81**, 63.

Kilin, S. Ya., and A. P. Nizovtev, 1990, Phys. Rev. A **42**, 4403.

Kurnit, N. A., I. D. Abella and S. R. Hartman, 1964, Phys. Rev. Lett. **13**, 567.

Levenson, M. D. and S. S. Kano, 1988a, 'Introduction to Nonlinear Laser Spectroscopy' (Academic Press, Boston), p. 47.

Levenson, M. D. and S. S. Kano, 1988b, 'Introduction to Nonlinear Laser Spectroscopy' (Academic Press, Boston), p. 216.

Lukac, M., F. W. Otto and E. L. Hahn, 1989, Phys. Rev. A **39**, 1123.

Macfarlane, R. M., R. M. Shelby and R. L. Shoemaker, 1979, Phys. Rev. Lett. **43**, 1726.

Macfarlane, R. M., C. S. Yannoni and R. M. Shelby, 1980, Opt. Comm. **32**, 101.

Macfarlane, R. M. and R. M. Shelby, 1981a, Opt. Comm. **39**, 169.

Macfarlane, R. M. and R. M Shelby, 1981b, Opt. Lett. **6**, 96.

Macfarlane, R. M. and R. M. Shelby, 1987, 'Coherent Transient and Holeburning Spectroscopy of Rare Earth Ions in Solids', in 'Spectroscopy of Solids Containing Rare Earth Ions', A. A. Kaplananskii and R. M. Macfarlane, eds. (Elsevier Science Publishers B. V., Amsterdam).

Mansmann, M., 1965, Deitschrift fur Kristallographie **122**, 375.

Manson, N. B. and P. T. H. Fisk, 1990, J. Lumin. **45**, 429.

Mitsunaga, M., E. S. Kintzer and R. G. Brewer, 1985, Phys. Rev. B **31**, 6947.

Mitsunaga, M., N. Uesugi and K. Sugiyama, 1993, Opt. Lett. **18**, 1256.

Moerner, W. E., 1988, ed., 'Persistent Spectral Hole Burning: Science and Applications' (Springer-Verlag, Berlin, 1988).

Mossberg, T. W., 1982, Opt. Lett. **7**, 77.

Muramoto, T. and A. Szabo, 1988, Phys. Rev. A **38**, 5928.

Muramoto, T., Y. Takahashi and T. Hashi, 1992, J. Lumin. **53**, 84.

Rand, S. C., A. Wolkaum, R. G. DeVoe and R. G. Brewer, 1979, Phys. Rev. Lett. **43**, 1868.

Reddy, B. R. and L. E. Erickson, 1983, Phys. Rev. B **27**, 5217.

Redfield, A., 1955, Phys. Rev. **98**, 1787.

Rutman, J., (1978), Proc. IEEE **66**, 1048.

Salomon Ch., D. Hils and J. L. Hall, 1988, J. Opt. Am. B **5**, 1576.
Shakhmuratov, R. , A. Szabo, 1993, Phys. Rev. B **48**, no 10, 6903-7.

Sharma, K. K. and L. E. Erickson, 1980, Phys. Rev. Lett. **45**, 294.

Shelby, R. M., C. S. Yannoni and R. M. Macfarlane, 1978, Phys. Rev. Lett. **41**, 1739.

Shelby, R. M., R. M. Macfarlane and C. S. Yannoni, 1980, Phys. Rev. B **21**, 5004.

Solomon, I., 1959, Acad. Sci. **248**, 92.

Steiner, I., V. Enders, F. Elsner, W. Neuhauser, P. E. Toschek, R. Blatt and J. Helmcke, 1989, Appl. Phys. B **49**, 251.

Sugiyama, K. and A. Morinaga, 1991, J. Appl. Phys. **30**, L1811.

Szabo, A. 1975, USA patent.

Szabo, A. and T. Muramoto, 1989, Phys. Rev. A **98**, 3992.

Teplov, M. A., 1968, Sov. Phys. JETP **26**, 872.

Torrey, H. C., 1949, Phys. Rev. **76**, 1059.

Wald, L. L., E. L. Hahn and M. Lukac, 1992, Opt. Soc. Am. B **9**, 789.

Wannemacher, R., R. M. Macfarlane, Y. P. Wang, D. Sox, D. Boye and R. S. Meltzer, 1991, J. Lumin., **48-49**, 309.

Wong, N. C., E. S. Kintzer, J. Mlynek, R. G. DeVoe and R. G. Brewer, 1983, Phys. Rev. B **28**, 4993.

Yano, R., M. Mitsunaga and N. Uesugi, 1992, J. Opt. Soc. Am. B **9**, 992.

Yariv, A., 1985, 'Optical Electronics', (Holt, Rinehart and Winston, New York).

Zalken, A., D. H. Templeton and T. E. Hopkins, 1966, Inorganic Chemistry **5**, 1466.

Zhu, M. and J. L. Hall, 1993, J. Opt.Soc. Am. B **10**, 802.

Shakhmuratov, R. , A. Szabo, 1993, Phys. Rev. B **48**, no 10, 6903-7.